Analysis of multi-b-value diffusion MRI data for characterisation of healthy and pathological brain tissue

Von der Medizinischen Fakultät der Rheinisch-Westfälischen Technischen Hochschule Aachen zur Erlangung des akademischen Grades eines Doktors der Theoretischen Medizin genehmigte Dissertation

vorgelegt von

Ricardo Loução

aus

Lissabon (Portugal)

Berichter: Univ.-Prof. Dr. Dr. h.c. Nadim Jon Shah
Priv.-Doz. Dr. med. Tanja Veselinović

Tag der mündlichen Prüfung: 16.07.2025

To Leonardo,
let him be inspired by the small feats of his father,
so that one day he can reach much further.

Parts of this work have already been published as:

- Loução R, Oros-Peusquens AM, Langen KJ, Ferreira HA, Shah NJ. A Fast Protocol for Multiparametric Characterisation of Diffusion in the Brain and Brain Tumours. Front Oncol. 2021 Sep 21;11:554205. doi: 10.3389/fonc.2021.554205

Abstract

Typically quantified by the apparent diffusion coefficient (ADC), diffusion MRI measures water diffusion in biological tissues which in turn is seen as a probe of microstructural changes derived from pathology. However, the ADC is confounded by a number of processes and phenomena rendering it sub-optimal for the characterisation of brain tissues. Additionally, the even more complex micro-environments of pathologies like brain tumours do not lend themselves to be properly summarised by a single value.

In this work, two methods for the acquisition and analysis of multi-b-value dMRI data were developed, expanding the ADC formalism and keeping in mind clinical feasibility.

The first is a unified model for the measurement of perfusion, and Gaussian and non-Gaussian diffusion. This is achieved by sampling the tissue at 16 unique b-values, from 0 to 3,000 s/mm^2, while including the clinically established b = 1,000 s/mm^2. With an acquisition time of 4 minutes and 19 seconds, four quantities can be derived from this protocol: pseudo-diffusivity and perfusion fraction, characterising the perfusion regime; apparent diffusivity, describing Gaussian diffusion; and apparent kurtosis, as a measure of non-Gaussian diffusion. This method was validated *in vivo* in a brain tumour patient cohort by pinning the derived quantities against their counterparts from established protocols. The metrics characterising perfusion did not correlate with their canonical counterparts, which suggests in part that these reflect different phenomena. Conversely, the Gaussian and non-Gaussian quantities proposed were highly correlated with those from the canonic protocols, indicating that the clinical usefulness of the canonic quantities is preserved when using the proposed metrics.

The second method is based on a parameter-free fitting of dMRI data with b-values ranging up to 10,000 s/mm^2, using non-negative least squares. This method provides with a diffusivity spectrum, as opposed to a fixed set of diffusivity pools and their relative fractions, allowing for a richer characterisation of the different diffusivity regimes in the tissue. Data was also fitted using established methods such as mono-, bi-, and tri-exponential decays in order to establish the added value of the proposed method. This method was demonstrated in a broad brain tumour cohort, where tissue specific spectra were derived: grey matter, white matter, cerebrospinal fluid, oedema, tumour, and restricted diffusion lesions. The latter develops as a consequence of the disease but it is yet poorly understood. The proposed method is applied to try to characterise this lesion. The suggested method was shown to better fit the data than the fixed-term models and the derived spectra show distinct differences in both healthy and pathologic tissue.

In conclusion, this work developed methods for the multi-parametric characterisation of diffusion in biological tissues, evaluated in brain tumour patients.

Zusammenfassung

Die diffusionsgewichtete MRT wird in der Regel durch den scheinbaren Diffusionskoeffizienten (ADC) quantifiziert und misst die Wasserdiffusion in biologischem Gewebe, was wiederum als Indikator für mikrostrukturelle Veränderungen in der Pathologie angesehen wird. Die ADC wird jedoch durch eine Reihe von Prozessen und Phänomenen beeinträchtigt, so dass der für die Charakterisierung von Hirngeweben nicht optimal ist. Darüber hinaus lassen sich die noch komplexeren Mikroumgebungen von Pathologien wie Hirntumoren nicht durch einen einzigen Wert angemessen zusammenfassen.

In dieser Arbeit wurden zwei Methoden für die Erfassung und Analyse von dMRT-Daten mit mehreren B-Werten entwickelt, die den ADC-Formalismus erweitern und die klinische Durchführbarkeit im Auge behalten.

Das erste ist ein einheitliches Modell für die Messung der Perfusion sowie der gaußschen und nicht-gaußschen Diffusion. Dies wird erreicht, indem das Gewebe bei 16 verschiedenen b-Werten von 0 bis 3.000 s/mm^2 abgetastet wird, wobei der klinisch etablierte $b = 1.000$ s/mm^2 berücksichtigt wird. Bei einer Aufnahmezeit von 4 Minuten und 19 Sekunden lassen sich aus diesem Protokoll vier Parameter ableiten: Pseudodiffusivität und Perfusionsanteil, die das Perfusionsregime charakterisieren; die scheinbare Diffusivität, die die Gaußsche Diffusion beschreibt; und die scheinbare Kurtosis als Maß für die nichtgaußsche Diffusion. Diese Methode wurde *in vivo* in einer Hirntumor-Patientenkohorte validiert, indem die abgeleiteten Größen mit ihren Gegenstücken aus etablierten Protokollen verglichen wurden. Die Parameter, die die Perfusion charakterisieren, korrelierten nicht mit ihren kanonischen Gegenstücken, was zum Teil darauf hindeutet, dass diese unterschiedliche Phänomene widerspiegeln. Umgekehrt korrelierten die vorgeschlagenen Gaußschen und nicht-Gaußschen Parameter in hohem Maße mit denen der kanonischen Protokolle, was darauf hindeutet, dass die klinische Nützlichkeit der kanonischen Parameter bei Verwendung der vorgeschlagenen Parameter erhalten bleibt.

Die zweite Methode basiert auf einer parameterfreien Fitting von dMRT-Daten mit b-Werten von bis zu 10.000 s/mm^2 unter Verwendung von der nicht negative kleinste Quadrate Methode. Diese liefert ein Diffusionsspektrum im Gegensatz zu einem festen Satz von Diffusionspools und deren relativen Anteilen, was eine umfassendere Charakterisierung der verschiedenen Diffusionsregime im Gewebe ermöglicht. Die Daten wurden auch mit etablierten Methoden wie mono-, bi- und tri-exponentiellem Zerfall angepasst, um den Mehrwert der vorgeschlagenen Methode zu ermitteln. Diese Methode wurde an einer breiten Hirntumorkohorte demonstriert, wobei gewebespezifische Spektren abgeleitet wurden. Es hat sich gezeigt, dass die vorgeschlagene Methode besser zu den Daten passt als die Modelle mit festen Diffusionspools, und die abgeleiteten Spektren zeigen deutliche Unterschiede zwischen gesundem und pathologischem Gewebe.

Zusammenfassend lässt sich sagen, dass in dieser Arbeit entwickelte Methoden für die multiparametrische Charakterisierung der Diffusion in biologischem Gewebe, die bei Hirntumorpatienten evaluiert wurden.

Contents

List of Figures

List of Tables

Glossary

ADC	apparent diffusion coefficient
AICc	corrected Akaike's information criterion
B_0	external magnetic field
BBB	blood-brain barrier
CBF	cerebral blood flow
CBV	cerebral blood volume
CT	computerised tomography
CV	coefficient of variation
D_{app}	apparent diffusivity
DKI	diffusion kurtosis imaging
DMRI	diffusion-weighted MRI
DSC	dynamic susceptibility contrast
DTI	diffusion tensor imaging
ECS	extracellular space
FA	fractional anisotropy
FDG	^{18}F-fluoro-2-deoxy-D-glucose
FDOPA	3,4-dihydroxy-6-[^{18}f]-fluoro-L-phenylalanine
FET	O-(2-^{18}F-fluoroethyl)-L-tyrosine
FLAIR	fluid-attenuated inversion recovery
FOV	field-of-view
FWHM	full-width half maximum
GM	grey matter
HGG	high grade glioma
IVIM	intravoxel incoherent motion
K_{app}	apparent kurtosis

LGG	low grade glioma
M_0	net magnetisation
MD	mean diffusivity
MeGRE	multi-echo gradient echo
MET	L-[methyl-^{11}C]methionine
MK	mean kurtosis
MRI	magnetic resonance imaging
PET	positron emission tomography
QMRI	quantitative MRI
RF	radio frequency
RMSE	root mean squared error
ROI	region of interest
SE-EPI	spin-echo echo planar imaging
SNR	signal-to-noise ratio
T_1	T_1-weighted
T_1C	T_1-weighted post-contrast
T_2	T_2-weighted
T_2^*	T_2^*-weighted
WM	white matter

1. Introduction

A staple of *in vivo* imaging in clinical practice is magnetic resonance imaging (MRI). This technique relies on tissue intrinsic properties to non-invasively depict tissues at, some times, sub-millimetre scales with exquisite soft tissue contrast. Such images can then be leveraged in a clinical setting to identify patterns of pathology, which help physicians make decisions pertaining to their clinical routine.

A particular variant of MRI, called diffusion-weighted MRI (dMRI), does not rely on the intrinsic properties of the tissues, but rather on the movement, in particular diffusion, of water molecules in the tissues. While initially conceptualised by Bloch in 1946 (Bloch, 1946), it was only in the mid-1980s that the first dMRI images of the brain were acquired (Le Bihan and Brenton, 1985; Le Bihan et al., 1986). The clinical usefulness of dMRI was shortly thereafter demonstrated by Moseley and colleagues, by showing that the dMRI signal measured in acute brain ischemia in cats dropped significantly (Moseley et al., 1990). This type of contrast was superior to the standard imaging done at the time and since then, dMRI has developed into a centre-piece of MRI in the clinical realm.

The uniqueness of the dMRI signal comes from the fact that the molecular movement of water is highly dependent on the types of barriers present in the imaged tissue. What this means is that changes in the tissue microstructure, well below the voxel level, are reflected in the measured dMRI signal. Therefore, dMRI has been used to study pathologies marked by their ability to change the microstructural environment, like, e.g., stroke or brain tumours.

Quantification of molecular diffusion in the clinic is performed using the apparent diffusion coefficient (ADC), neatly summarising into one value the amount of water diffusion in a given region (Le Bihan et al., 1986). To calculate the ADC, one requires only a pair of

images: one without diffusion weighting and one with a diffusion weighting. This diffusion weighting is typically summarised by the b-value Le Bihan et al. (1986).

Despite its simplicity of acquisition and calculation, the ADC suffers from some drawbacks. Like the name suggests, it is an "apparent" value, confounded by other types of molecular movement, such as capillary perfusion (Le Bihan et al., 1988). Additionally, a single value per voxel assumes that a single population of diffusing molecules exists within that voxel. This is not correct, as it has been demonstrated that intra-cellular and extra-cellular water molecules diffuse at different rates (Mulkern et al., 1999). Moreover, the ADC formalism assumes that water diffusion is isotropic and therefore follows a Gaussian distribution. However, microstructural barriers which hinder diffusion lead to the violation of the gaussianity assumption (Jensen et al., 2005). Overall, this means that diffusion in the tissue is not properly characterised solely by the ADC.

Over the years, multiple formalisms have been introduced to deal with the shortcomings of the ADC. These include expanding the number of diffusing pools (Mulkern et al., 1999; Zeng et al., 2018), including other types of molecular movement (Le Bihan et al., 1988; Federau et al., 2014b), or even adding non-Gaussianity terms to the formalism (Jensen et al., 2005; Jensen and Helpern, 2010).

While each of these adds to the characterisation of pathological micro-environment, holding some level of clinical applicability (Maier et al., 2010; Federau et al., 2014a; Jiang et al., 2015), the concurrent evaluation of multiple of these parameters is lacking. Additionally, the range of b-values used in the clinic is very limited, while it has been shown that including higher b-values holds higher utility in, e.g., the grading of tumours (Seo et al., 2008; Kang et al., 2011; Zeng et al., 2017).

In this thesis, methods for the acquisition and analysis of multi-b-value dMRI data are presented and applied to brain tumour cohorts. These methods expand on the aforementioned ones in that: 1) a unified framework for the acquisition and processing of data leading to perfusion, Gaussian, and non-Gaussianity related quantities is developed; 2) expansion of modelling of fixed amounts of diffusing pools into a data-driven, agnostic model, characterising as many diffusion pools as the data suggests. Such methods could provide

researchers and clinicians alike with tools to multi-parametrically characterise pathological tissue, in an era where quantitative assessment of MRI data is gaining traction.

This thesis starts with an introduction of the MRI and dMRI concepts, given in chapter 2, and a brief overview of brain tumour imaging in chapter 3.

In chapter 4, an extended framework for diffusion estimation across three distinct diffusion ranges is provided: intravoxel incoherent motion, Gaussian diffusion, and non-Gaussian diffusion. These diffusion ranges are linked to perfusion phenomena, free-water diffusion, and restricted diffusion, respectively. The diffusivity metrics in each of these three ranges can hold information regarding processes like, e.g., angiogenesis, which could be potential biomarkers for tumour malignancy. This chapter is based on Loução et al. (2021).

The framework is further extended in chapter 5, where the analysis of very restricted diffusion is performed in a cohort of brain tumour patients. Through the acquisition of very high b-values ($> 5{,}000$ s/mm^2), dMRI is sensitive to molecules that move particularly slow, due to the presence of a highly restrictive micro-environment, which can be indicative of disease progression. Particular focus is given to restricted diffusion lesions in brain tumour patients whose origin is still elusive but have been associated with poor prognosis. The analysis methods investigated include both fixed-term and term-free models with the goal of identifying unique characteristics within these lesions which can hold prognostic value.

Finally, chapter 6 gives concluding remarks and provides an outlook of the work developed.

2. Magnetic Resonance Imaging

Magnetic resonance imaging (MRI) is a non-invasive imaging technique based on the principle of nuclear magnetic resonance, arising from the interaction between spins and magnetic fields. In order to understand the origin of the diffusion-weighted signal provided by MRI, it is important to have a foundation of the underlying physics. This chapter will introduce them to the reader. While the physics of MRI are better explained under the guise of quantum mechanics, here I will adopt the classical formulation, since it is sufficient to understand the underlying phenomena and concepts used in this thesis.

2.1. Spins, excitation, and relaxation

Rotating objects described by classical physics possess a property called angular momentum. This is a form of inertia which depends on the physical characteristics of the object, such as shape, mass, and rotational velocity. Atomic nuclei posses a similar property, commonly referred to as spin (Griffiths and Schroeter, 2018). Just like the angular momentum interacts with gravitational fields, so too do the spins, except with electromagnetic fields. This is because nuclei with non-zero spin possess a magnetic dipole moment, which can be thought of as a small magnet.

In the absence of an external magnetic field, the spins in a given material are randomly oriented. When summed up, the random orientations of the spins lead to a null net magnetisation, as the small magnets end up cancelling each other out. Once the spins are placed in an external static magnetic field, they tend to align along it, creating a non-zero net magnetisation on the sample. This forms the basis of the MRI signal and is depicted in Fig. 2.1.

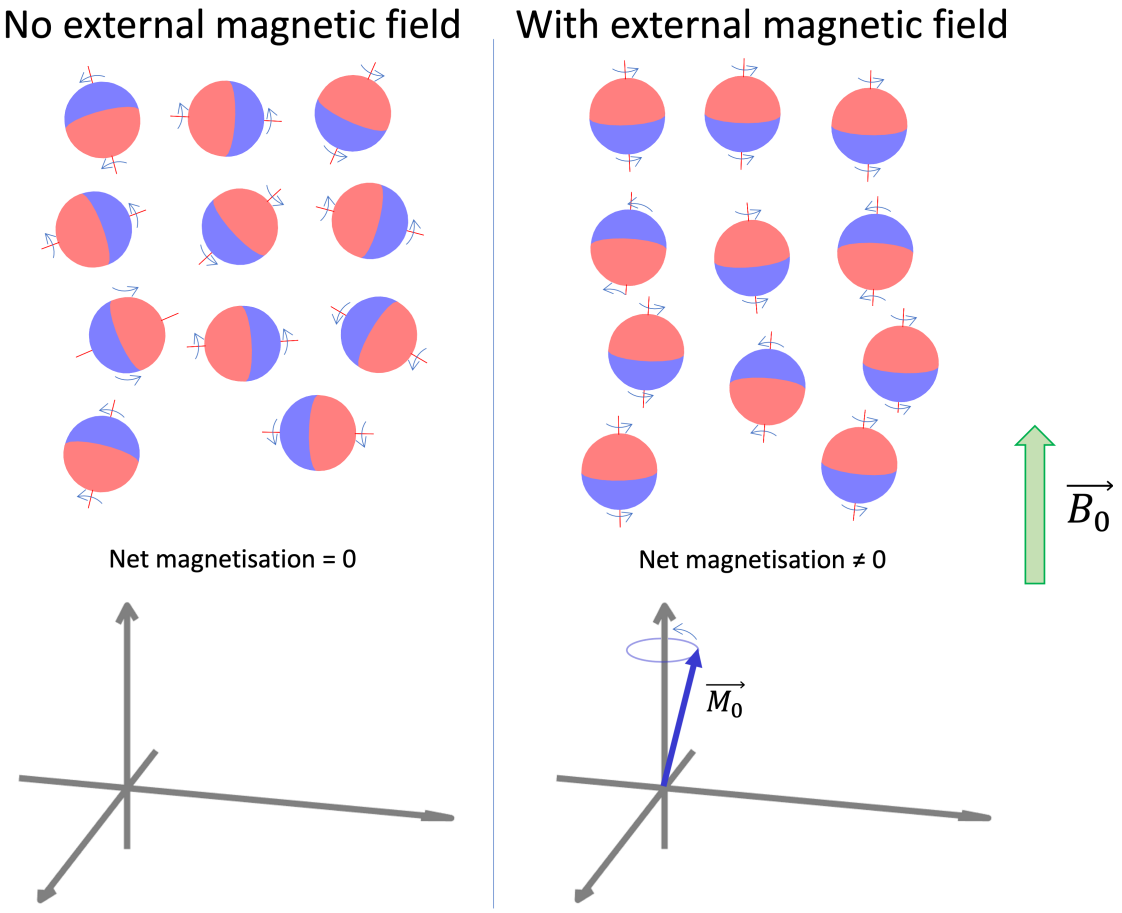

Figure 2.1.: *Effect of an external magnetic field on spins. Without the presence of an external magnetic field (left panel), the spins are randomly oriented, resulting in a zero net magnetisation. If subject to an external magnetic field, the spins will align along it, creating a non-zero magnetisation which will precess around the direction of the external magnetic field.*

The net magnetisation, typically denoted as M_0, can be interpreted as a spinning top, precessing along the direction of the external magnetic field, typically denoted as z. The precession frequency, called Larmor frequency, is given by

$$\omega_0 = \gamma B_0 \tag{2.1}$$

where γ is the gyromagnetic ratio of the imaged atom, and B_0 is the intensity of the magnetic field (Levitt, 2013). The imaged atom in most of the MRI field and in this work is $^1_1$H,

which has a gyromagnetic ratio of 42.576 MHz/T, so that the Larmor frequency at 3 Tesla is about 128 MHz.

Due to this precession of M_0, the description of spins and their evolution in time throughout an MRI experiment is typically performed in a rotating frame of reference. This is defined as the reference frame precessing with M_0. This is achieved by aligning the z-axis to M_0 so that it becomes stationary when in equilibrium.

In order to obtain a signal, the net magnetisation needs to be excited using radio frequency (RF) pulses. These RF pulses are applied at the Larmor frequency so that resonance can be induced (Purcell et al., 1946). Typical pulses include tipping M_0 to either 90° or 180°, although any angle is technically possible.

If a pulse of 90° is applied, then M_0 will be transferred to xy plane, i.e. the plane perpendicular to the magnetic field direction, called the transverse plane. This transverse component of the magnetisation, μ_{xy}, will then relax back to equilibrium, $\mu_{xy} = 0$, following:

$$\mu_{xy}(t) = M_0 e^{-t/T_2} \tag{2.2}$$

with T_2 being the transverse relaxation time (Bloch, 1946). This process is called T_2, transverse, or spin-spin relaxation. This process arises from the interactions of the spins with each other, leading to a loss of phase coherence and therefore to a loss of μ_{xy} with time.

Alongside T_2 relaxation, the magnetisation along the z axis, μ_z, will also relax. In the above 90° example, $+\mu_z \equiv M_0$, is nullified after the RF pulse is applied. As the system is allowed to relax back to equilibrium, μ_z has the following evolution:

$$\mu_z(t) = M_0(1 - e^{-t/T_1}) \tag{2.3}$$

This process is called T_1, longitudinal, or spin-lattice relaxation, with T_1 being the longitudinal relaxation time (Bloch, 1946). Longitudinal relaxation is a consequence of the spins being in a strong main magnetic field: after the RF pulse, the spins will go back to

their equilibrium position and this process is governed by T_1 relaxation. The evolution of μ_{xy} and μ_z in time are demonstrated in Fig. 2.2 after a 90° RF pulse.

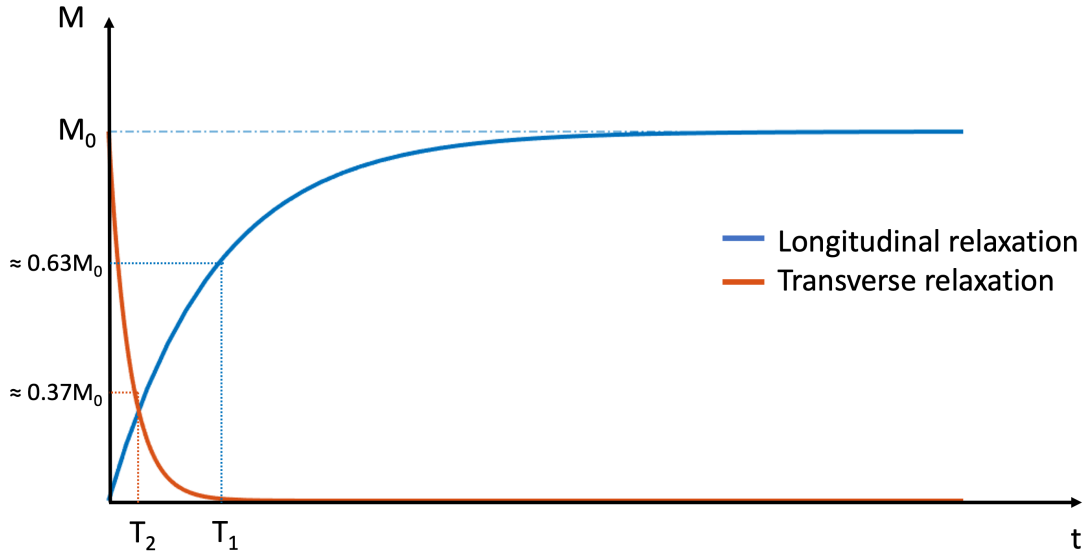

Figure 2.2.: *Longitudinal and transverse relaxations after a 90° RF pulse. The plot illustrates the evolution of both T_1 and T_2 in time after a 90° pulse. In biological tissues, T_1 is typically much larger than T_2.*

Whenever the magnetisation has a component in the xy plane, i.e. $\mu_{xy} \neq 0$, it becomes possible to measure it. By positioning a coil around the sample, perpendicular to, e.g., the y axis and tuned to the sample's Larmor frequency, an electric current will be induced in the coil due to Faraday's induction law - as shown in Fig. 2.3.

After a simple 90° pulse, the measured signal is called free induction decay (FID) (Hahn, 1950a). Shown in the third panel of Fig. 2.3, the FID decays exponentially with T_2, in theory. In practice, however, due to inhomogeneities in B_0, each spin will experience a slightly different magnetic field, which leads to a faster loss of spin coherence, which in turn results in a much quicker signal decay. This decay constant is called T_2^* and it can be expressed as:

$$\frac{1}{T_2^*} = \frac{1}{T_2} + \frac{1}{T_{2inhom}} \tag{2.4}$$

where T_{2inhom} is the decay rate resulting from the field inhomogeneities.

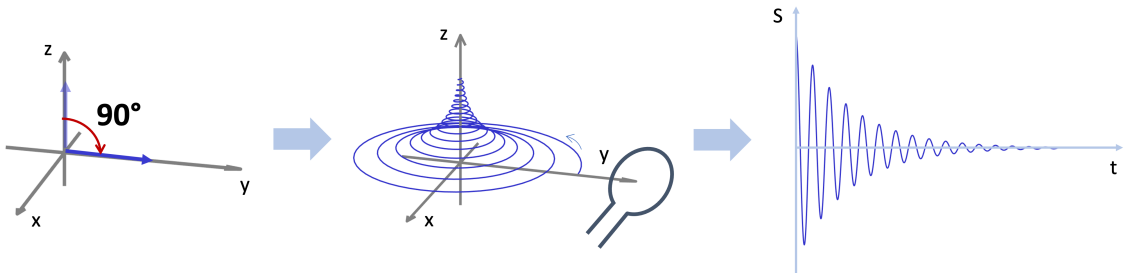

Figure 2.3.: *Schematic demonstration of the measurement of FID. After a 90° RF pulse (left panel), the magnetisation vector will return to equilibrium according to the trajectory shown in the middle panel by virtue of of both T_1 and T_2 relaxations. Placing a coil next to the sample will induce a current in that coil due to Faraday's induction law. The signal picked up by the coil is demonstrated in the third panel and is called free induction decay (FID). The envelope of the FID decays with T_2.*

2.2. Spatial encoding, kspace, and imaging

As mentioned above, the preferred atom for MRI is $^1_1$H due to its high relative abundance. The human body, comprised primarily of water - with its two protons -, is an excellent sample for MRI. However, in order to image the human body, it is important to determine the spatial location of the spins' signal. This is achieved via the application of magnetic field gradients to the sample in such a way that each region in space is subject to a slightly different magnetic field and, therefore, the respective spins rotate at slightly different Larmor frequencies (Liang et al., 2000). For reference, current static magnetic fields in MRI vary from 1.5 to 7 T, while the gradients are typically between 0.01 and 0.1 T/m.

2.2.1. Slice encoding

The first step in identifying the source of the signal, and therefore of creating an image is called slice encoding. While slice encoding is typically performed along the z-axis, it can also be performed along any other axis. Taking the z as an example, a gradient field, G_z, is applied along this direction, demonstrated in Fig. 2.4. This, in turn, results in the spins along this gradient precessing at different Larmor frequencies, as given by:

$$\omega_z = \gamma(B_0 + G_z) \tag{2.5}$$

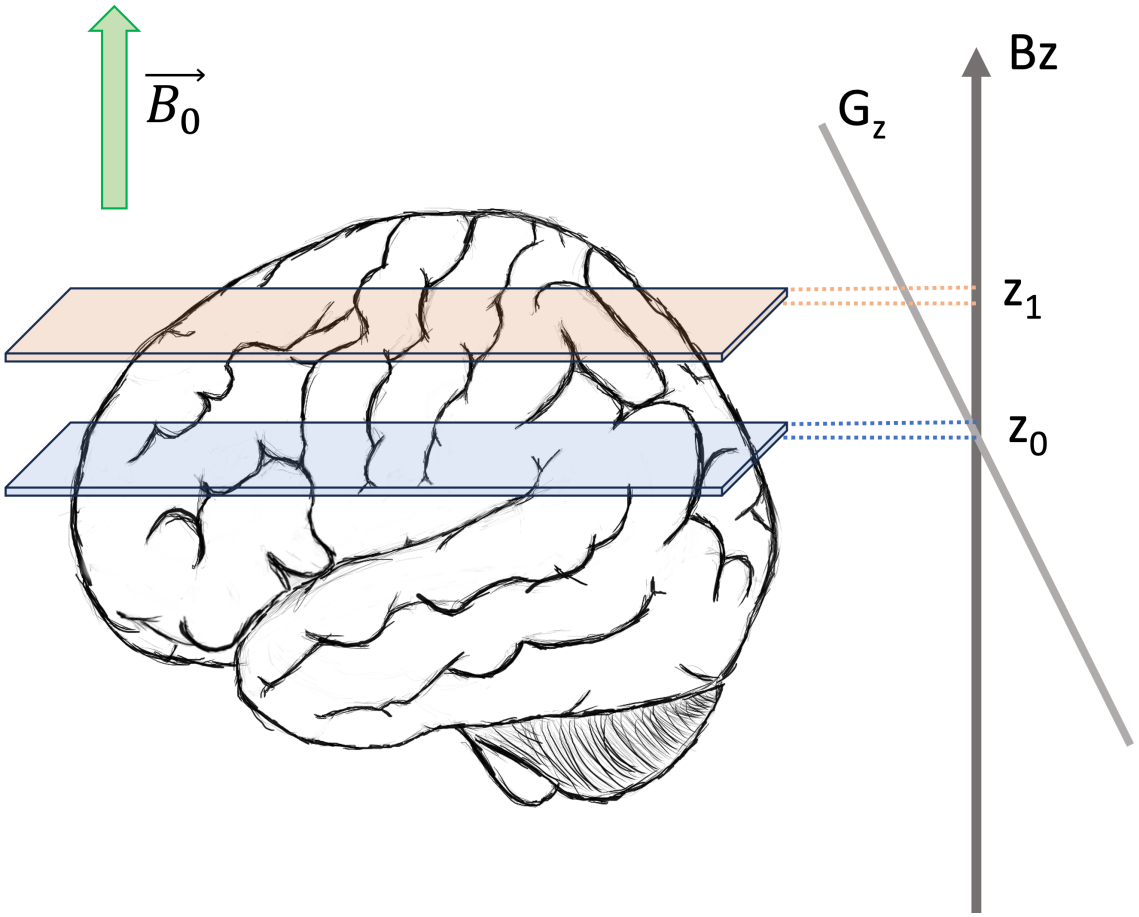

Figure 2.4.: *Slice encoding gradient. The gradient is applied along the z-axis, so that different points along this dimension experience different precessing frequencies. At z_0, the spins precess at Larmor frequency; at z_1 the spins precess at a slightly faster frequency, given by Eq. 2.5*

It follows, therefore, that in order to excite spins at position z_0, i.e. the centre of the gradient field, a pulse with Larmor frequency should be applied (ω_0), while to excite spins at position z_1 an RF pulse with frequency ω_1 needs to be applied: faster if the spins are in the positive part of G_z, slower if in the negative part of G_z. The thickness of the excited slice depends on the frequency bandwidth of the applied pulse.

At this stage, all of the spins in the slice will emit a signal. However, discriminating their position in x and y is still not possible. To do that, two extra sets of gradients need to be applied, one for the encoding along x, and another for the encoding along y.

2.2.2. Phase encoding

By applying a gradient pulse, with duration T_p, perpendicular to that of slice selection, e.g., along the y direction (G_y), the spins along this direction will precess either faster or slower compared to ω_0, depending on whether they find themselves in the positive or negative part of G_y. When G_y is turned off, all of the spins will return to the precessing frequency of ω_0, however, with phase offsets - Fig. 2.5, left panels. These phase offsets are used to identify the spins along y.

2.2.3. Frequency encoding

Finally, when an additional gradient is applied in a direction perpendicular to that of the slice encoding and frequency encoding - now G_x, according to the previous examples -, the spins along this gradient will experience slightly different magnetic fields, leading to different precessing frequencies - Fig. 2.5, right panels. This gradient G_x stays on during the readout phase, i.e. when the signal from the sample is actually measured, which will then identify their position along the x direction. Since the gradient stays on for the whole readout part, frequency encoding is a very efficient step, as it allows us to sample multiple points with a single excitation pulse.

2.2.4. k-space

Now that we can identify the position in space where the signal comes from, it becomes possible to build an image from the acquired signal. The very first step is to demodulate the signal, which means to electronically remove the Larmor frequency. The retrieved demodulated signal after phase encoding is denoted by:

$$S(t) = \iint_{slice} I(x,y) e^{-i\gamma G_y y T_p} dxdy, t > T_p \tag{2.6}$$

where

$$I(x,y) = \int_{-\Delta z/2}^{+\Delta z/2} \rho(x,y,z) dz \tag{2.7}$$

with $\rho(x, y, z)$ being the proton density of the sample at position (x,y,z). The quantity $\gamma G_y y T_p$ from Eq. 2.6 gives the accumulated phase by the protons at position y after a gradient pulse of duration T_p. Note that I have chosen to ignore the effects of relaxation for simplicity - they will be introduced later on.

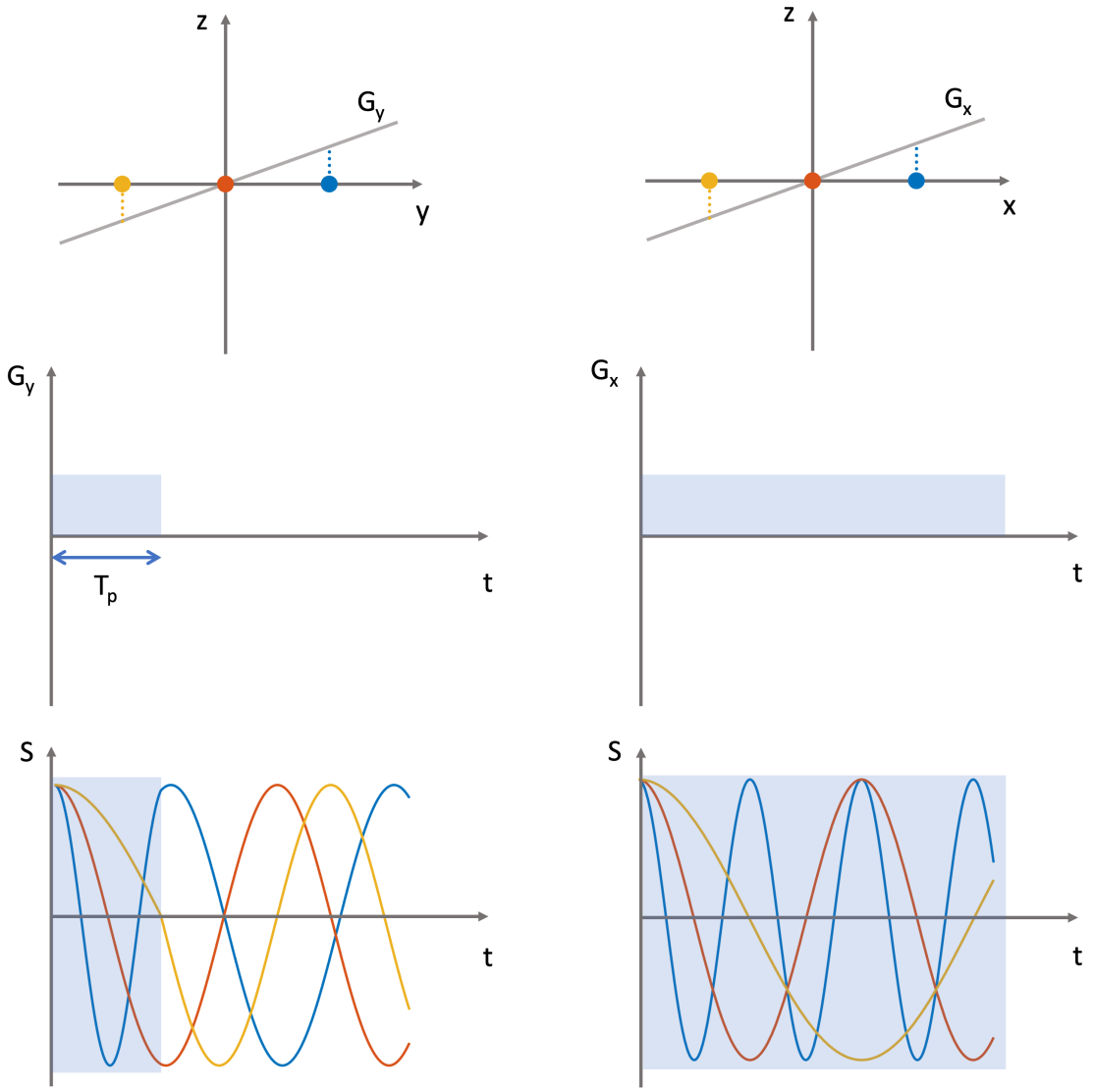

Figure 2.5.: *Phase and frequency encoding. On the left panels are shown the phase encoding steps, and on the right the frequency encoding. While the principles are the same, note that phase encoding gradients are only on for a short amount of time, T_p, after which the spins will return to precessing at Larmor frequency but each position will show a phase offset. The frequency encoding gradients, on the other hand, are on for the full duration of the readout.*

After frequency encoding, the signal can be expressed by:

$$S(t) = \iint_{slice} I(x,y) e^{-i\gamma G_x x t} dxdy \tag{2.8}$$

where $e^{-i\gamma G_x x t}$ denotes the frequency encoding along x.

Joining Eqs. 2.6 and 2.8, one can express the signal after frequency and phase encoding by:

$$S(t) = \iint_{slice} I(x,y) e^{-i\gamma G_y y T_p + \gamma G_x (t-TE) x} dxdy \tag{2.9}$$

where TE is the echo time - see 2.2.5.

Defining auxiliary variables as

$$\begin{aligned} \eth &= \gamma/2\pi, \\ k_x &= \eth G_x (t - TE), \\ k_y &= \eth G_y T_p \end{aligned} \tag{2.10}$$

it is possible to rewrite Eq. 2.9 as

$$S(k_x, k_y) = \iint_{slice} I(x,y) e^{-i2\pi[k_x x + k_y y]} dxdy \tag{2.11}$$

The keen reader will identify the similarities between relation 2.11 and a 2D Fourier Transform (FT). Indeed, the underlying proton distribution, i.e. our image function $I(x,y)$, can be obtained by applying an inverse FT to the sampled data $S(k_x, k_y)$. The domain in which the measured signal resides is called k-space and it has units of cm^{-1} (Spraggins, 1996). If one talks about the object residing in "space domain", then k-space resides in "spatial frequency domain", encoding the spatial frequencies and phases of the imaged object.

Flavours of k-space sampling strategies are plentiful, but the simplest and the one used in this thesis is called cartesian sampling. In it, the k-space is seen as a grid with NxN

points, typically sampled line-by-line. The number of measurements in a line, i.e. along k_x, is given by:

$$N = \frac{T_A}{\Delta t} \tag{2.12}$$

where T_A is the acquisition time and Δt the time interval between sampling. Lines are then switched by varying G_y by some increment ΔG_y, leading to a new k_y. Increments of k_y and k_x are then given by:

$$\begin{aligned} \Delta k_x &= \gamma |G_x| \Delta t \\ \Delta k_y &= \gamma \Delta G_y T_p \end{aligned} \tag{2.13}$$

The final image, i.e. the inverse Fourier transformed k-space, will have resolution - Δx and Δy - and size - otherwise known as the field-of-view (FOV) - dependent on k_x and k_y according to the following relations:

$$\begin{aligned} FOV_x &= \frac{1}{\Delta k_x} = \frac{1}{\gamma |G_x| \Delta t} \\ FOV_y &= \frac{1}{\Delta k_y} = \frac{1}{\gamma \Delta G_y T_p} \\ \Delta x &= \frac{FOV_x}{N} = \frac{1}{\gamma |G_x| T_A} \\ \Delta y &= \frac{FOV_y}{N} = \frac{1}{\gamma G_{ymax} T_p} \end{aligned} \tag{2.14}$$

Image resolution and FOV are therefore determined by adjusting the acquisition parameters of the MRI sequence shown in Eq. 2.14.

2.2.5. Imaging sequences

We know now how to identify the spatial source of the signal and to sample the k-space, so it is important to know how to prepare the spins for the signal acquisition. As seen in the previous sections, the spins can be manipulated using RF pulses and magnetic gradients.

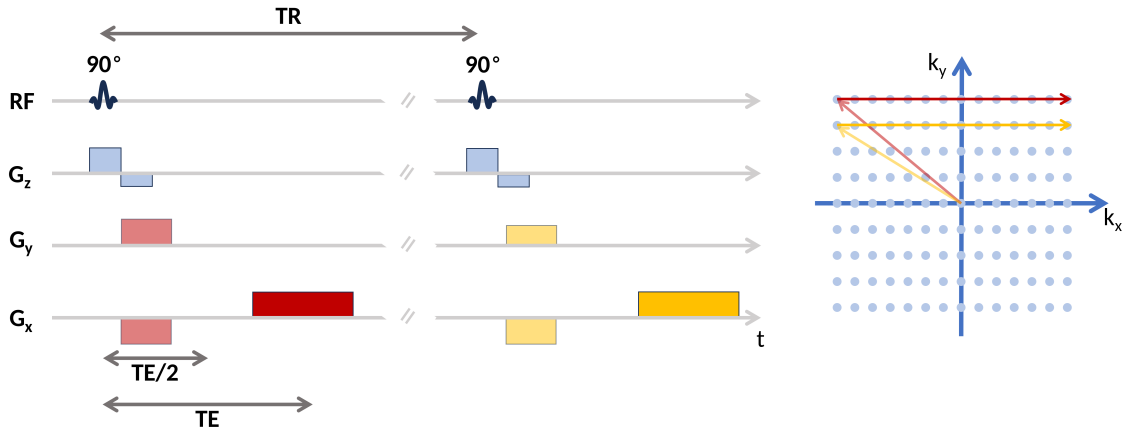

Figure 2.6.: *Gradient echo sequence. After the 90° pulse and the slice encoding, phase encoding ensues. After that, the frequency encoding is applied during readout, producing an echo at time TE. Note that G_y is varied at the second repetition so as to sample a different k_y line of k-space (red vs yellow gradients/trajectories in k-space).*

The reader will recall that after a 90° pulse, the spins will produce an FID. With the application of imaging gradients, the spins dephase much quicker, leading to a very quick loss of signal. In order to obtain signal again, the spins need to be refocussed, which is achieved by applying either gradients or RF pulses. In the end, at the time the spins get refocussed, an echo of the FID is produced, which is the signal measured by the scanner. To the combination of the different RF pulses and gradients responsible for producing an echo, from excitation to measurement, we call an imaging sequence.

One of the simplest imaging sequences is the gradient echo (GRE) sequence (Markl and Leupold, 2012), whose sequence diagram and k-space trajectory are shown in Fig. 2.6. It starts with a 90° RF pulse combined with a slice encoding gradient, guaranteeing slice selection. Following that, the phase and the frequency encoding gradients are applied concurrently. The frequency encoding gradient forces a controlled dephasing of the spins, leading to a loss of the FID - as stated previously. The time between the centre of the RF pulse and the end of the frequency encoding gradient is half of the echo time (TE). The signal is then recovered by applying a readout gradient, which has opposite polarity and twice the length of the frequency encoding gradient, recovering the spins' coherence, producing an echo at time point TE.

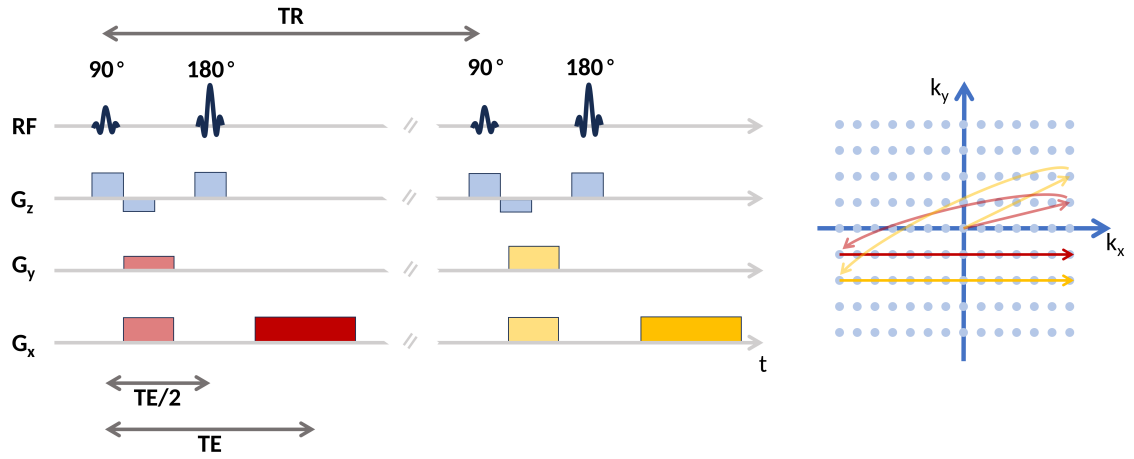

Figure 2.7.: *Spin echo sequence. After the 90° pulse and the slice encoding, phase encoding ensues just like in the GRE sequence. Spin refocusing is achieved by applying a 180° pulse, followed by the frequency encoding/readout. When looking at the k-space trajectories, the 180° RF pulse rotates the k-space "cursor" around the k-space centre by 180°.*

Another very common preparation is the spin-echo (SE) sequence, shown in Fig. 2.7 (Hahn, 1950b). It differs from the GRE sequence in that instead of rephasing the spins using gradients, rephasing is done by virtue of an RF pulse. Thus, an SE experiment starts just like a GRE one, with a 90° pulse with concurrent slice encoding, tipping the spins to the xy plane. A concurrent phase and frequency encoding follows, during which, the spins dephase analogously to the GRE experiment. After that, a second RF pulse is applied at TE/2, together with another slice selection gradient. This second RF pulse has 180°, leading to the refocussing of the spins, producing, once again, an echo at time TE.

Two important notes are worth mentioning. Firstly, after the 90° RF pulse in both GRE and SE, an additional gradient is used in G_z to destroy the accumulated phase during slice encoding. When uncompensated, this accumulated phase would negatively influence the rest of the measurement. Secondly, since the frequency encoding step is very efficient, as mentioned before, it is advantageous to acquire redundant information during the echo formation. This is achieved via applying two opposite frequency encoding gradients. One can think of the first frequency encoding gradient as moving the k-space "cursor" to position $-k_{xmax}$, and the second one as moving towards $+k_{xmax}$. Effectively this makes it so that the acquired signal during the first half of the readout is the "ramp-up" to the echo and the second half is the "ramp-down", with the peak of the echo at the centre of k-space. Without

the first frequency encoding, the acquired signal would start at the centre of k-space ($k_x = 0$), and by applying only the readout encoding gradient one would only acquire the positive k_x-half of k-space.

The preparations described are used to fill a single k-space line - red lines in Figs. 2.6 and 2.7. Before preparing to fill the second line - yellow lines in Figs. 2.6 and 2.7 - , one needs to allow the spins to recover their longitudinal magnetisation. In order to allow the spins to relax back to equilibrium, a certain amount of time needs to be waited until the next excitation is performed and the whole process is repeated to fill the next k-space line. The time between the first RF pulse of consecutive preparations is called repetition time (TR). Usually, TR $\geq$ 5T1, to ensure that the majority of the longitudinal magnetisation has recovered. The next line in k-space is then sampled by varying the phase encoding gradient by some interval ΔG_y, and this process is repeated N times until all k-space lines are filled.

2.2.6. Echo planar imaging

While normal TE values vary between 20 to 150 ms, typical TR values can go up to several seconds. Therefore, the total acquisition time of an image is highly dependent on the TR. In fact, considering e.g. a TR of 5 seconds, a k-space matrix with 128 lines will take around 640 seconds, or circa 10 minutes, to acquire. For some applications, such long sampling times are not acceptable and, so, clever ways of rapidly sampling k-space have been developed. In this section, I will introduce only one of the many existing ones, as it occupies a central piece in the thesis.

Suppose we prepare the signal using SE, except now, instead of applying an arbitrary phase / frequency gradient combination, we apply one such that the k-space "cursor" moves to position ($+k_{xmax}$, $-k_{ymax}$). After the 180° pulse, the k-space cursor is moved to position ($-k_{xmax}$, $+k_{ymax}$), corresponding to a mirroring along the k-space origin. After the first frequency/readout gradient, we have sampled the first k-space line at $+k_{ymax}$ and the k-space "cursor" has moved to position ($+k_{xmax}$, $+k_{ymax}$).

Now comes the clever part: instead of waiting for the longitudinal magnetisation to recover, we move the k-space "cursor" one k-space line down, by applying another phase

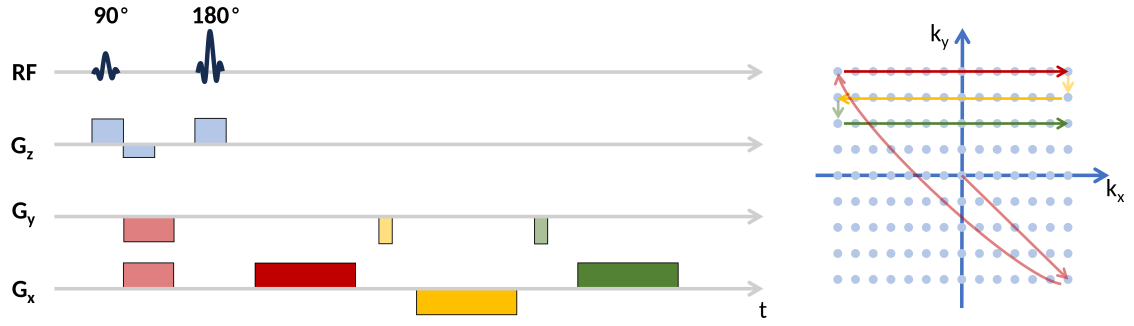

Figure 2.8.: *Echo planar imaging. This type of readout allows the acquisition of the full k-space with just one excitation. After the first readout, shown by the red line, a G_y blip is applied, shifting the k-space line followed by a second readout. These gradients produce another echo at the centre of k-space, and are repeated until the whole k-space has been sampled.*

encoding gradient, followed by a readout gradient opposite to the previous one, moving the "cursor" to $(-k_{xmax}, +k_{ymax} - \Delta k_y)$. These last two steps are repeated until the k-space has been sampled in a sort of zig-zag pattern. This readout method is called echo planar imaging (EPI) (Mansfield, 1977), shown schematically in Fig 2.8, and is a staple of fast imaging methods allowing to acquire a full brain image in just a few seconds.

2.3. Imaging contrasts

Now that the foundations of image formation and imaging sequences have been established, it is important to understand how all of these concepts interplay to generate image contrast. From the Bloch equations (Bloch, 1946) it follows that a signal prepared with an SE sequence will be

$$S(t) \propto \rho(x,y,z)(1 - e^{-\frac{TR}{T_1}})e^{-\frac{TE}{T_2}} \tag{2.15}$$

where $\rho(x,y,z)$ is the proton density of the sample at position (x,y,z). It becomes apparent, therefore, that the retrieved signal depends on three aspects: the local proton concentration,

the TR, and the TE. The manipulation of the latter two parameters will give rise to different imaging contrasts (Perman et al., 1984).

When TR is long compared to T_1, the term e^{-TR/T_1} will tend to 0, and $(1 - e^{-TR/T_1})$ will tend to 1, meaning that the effects of T_1 will have disappeared. In other words, at long TRs, spins with different T_1 would have had time to recover most of their longitudinal magnetisation, so that differences in signal between these populations are neglectable. Conversely, shorter TRs compared to T_1 tend to manifest in a T_1-weighting, as the different spins are still recovering their longitudinal magnetisation, each at different stages of this recovery, producing different signals.

On the other hand, a TE that is much shorter than T_2 will lead to the term e^{-TE/T_2} tend to 1, which means that the T_2 contributions are largely neglectable. If TE is made longer than T_2 then the respective exponential term becomes more and more relevant, increasing the T_2-weighting in the image.

When TR is kept long compared to T_1 and TE is kept short compared to T_2, then both T_1 and T_2 contributions have mostly disappeared. This results in an image that is proton density-weighted.

Finally, short TR compared to T_1 and long TE compared to T_2 produces an image influenced by both T_1- and T_2-weighting. Due to the lack of predominant contrast, this type of image is of little practical use and, so, sequences with these parameters are not employed.

Examples of all these contrasts can be seen in Fig. 2.9.

If the preparation is performed with a GRE sequence, the signal will be given by:

$$S(t) \propto \rho(x, y, z)(1 - e^{-\frac{TR}{T_1}})e^{-\frac{TE}{T_2^*}} \tag{2.16}$$

Note that the transverse relaxation effect is no longer dependent on T_2 but rather on T_2^*. This means that, conversely to an SE sequence, a GRE sequence with long TR and long TE will produce a T_2^*-weighted image, instead of a T_2-weighted one.

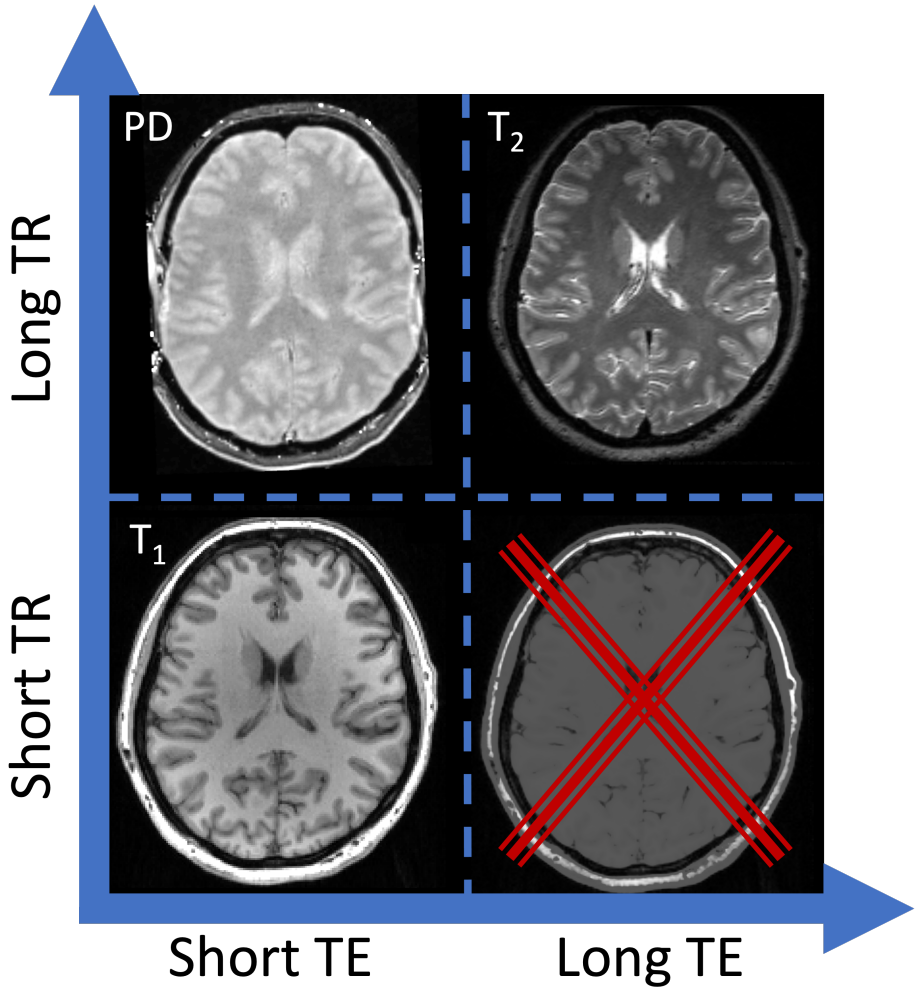

Figure 2.9.: *TR, TE, and imaging constrasts. By manipulating the TR and TE, different contrast weightings can be obtained. A relatively short TE combined with a short TR will produce a T_1-weighted image, while when combined with a long TR will result in a proton density-weighted image. Long TE combined with long TR will result in a T_2-weighted image, and long TE with short TR produces an image with mixed effects, resulting in a poor contrast image.*

2.3.1. Diffusion MRI

Up until now, one consideration was purposeful omitted for the sake of simplicity: the water molecules, our imaged substance, in the sample do not move. However, this is not strictly true. In fact, in biological tissues, water molecular movement can happen due to a number of reasons but one can sort them into two main categories: flow and diffusion, i.e. organised

and unorganised movement, respectively. Flow is mostly seen in the blood vessels of the body and so its imaging is mainly used to assess vessel structure. Diffusion, on the other hand, occurs pretty much everywhere in the human body and its imaging can be used to infer on microstructural changes of tissue due to, e.g., pathology.

Due to their thermal energy, water molecules diffuse within the biological tissues. This motion will contribute to the loss of spin coherence: the faster the motion, the quicker the coherence loss. In order to measure this coherence loss, Stejkal and Tanner proposed applying an additional set of gradients, responsible for picking up moving molecules along a particular direction (Stejskal and Tanner, 1965). The original sequence proposed by Stejkal and Tanner was based on the SE sequence, with the addition of two identical gradient pulses surrounding the 180° RF pulse. This sequence was called pulsed gradient spin echo (PGSE) and to these additional gradients we give the name of diffusion encoding gradients. An illustration of the PGSE sequence is shown in Fig. 2.10.

To understand the effect of these gradients, let us consider two scenarios: the case in which the molecules do not move between the two pulsed gradients and the case in which they do. These are demonstrated in Fig. 2.10. For the sake of simplicity, let us ignore the imaging gradients.

In the first case, i.e. the spins do not move, these get tipped to the transverse plane, xy, after the 90° pulse. The first diffusion encoding gradient is then applied along a given direction, causing the spins to precess with different frequencies along this direction, dephasing with respect to each other. Then, at time TE/2, the 180° RF pulse is applied, flipping the spins. This is then followed by the application of the second diffusion encoding gradient, ultimately forcing the spins to rephase. A fully-refocused echo is then produced at TE (Fig. 2.10, upper row of boxes).

In the second case however, after the application of the first diffusion encoding gradient pulse, the spins are allowed to move. What this means is that, after the application of the 180° RF pulse and the second diffusion encoding gradient, the spins which moved along the direction of the diffusion gradients will no longer experience the same field strength as they did during the first diffusion encoding gradient. This means that the refocus of the spins

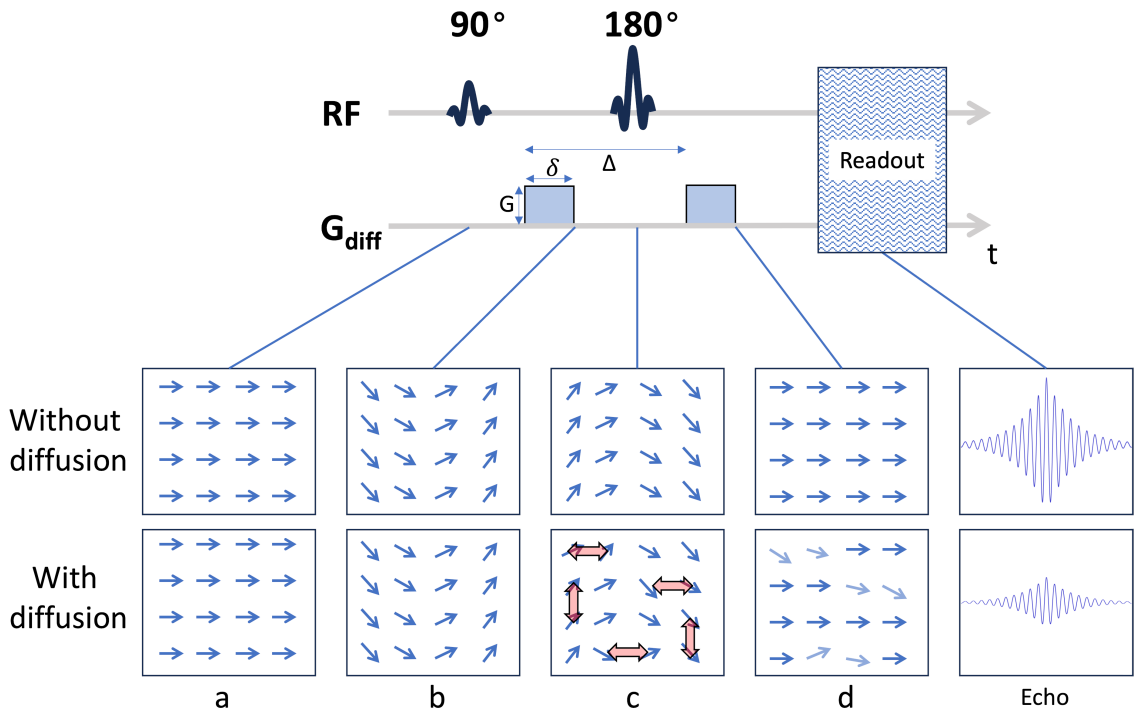

Figure 2.10.: *Diffusion weighting gradients and effects of diffusing spins. On the top is shown a schematic of the pulsed gradient spin echo sequence with diffusion gradients, G_{diff}. The characteristics of G_{diff} are shown next to the first gradient: G is the gradient amplitude, δ is the gradient duration, and Δ is the elapsed time between the beginning of both gradients. On the bottom are shown hypothetical pixels with an ensemble of spins, represented by arrows. The diffusion gradient direction in this example is always from left to right of the pixels. After the 90° RF pulse (a) and the first G_{diff} is applied (b), spins can precess either slower (arrows pointing up) or faster (arrows pointing down) according to the encoding principles described in 2.2. Between the first and second gradients, molecules either stay stationary (row labelled "without diffusion") or diffuse (row labelled "with diffusion"). In the case spins stay stationary (c), the second gradient fully refocuses the spins (d), leading to a full echo at TE. If the molecules diffuse, demonstrated by the red arrows (c), the spins do not fully refocus at TE, shown by the light blue arrows (d), leading to an attenuated echo. Note that only diffusing molecules along the diffusion gradient direction (left-to-right) contribute to the echo attenuation as only these will experience different G_{diff}.*

will be impartial, leading to an attenuated echo, when compared to that obtained in the case of no molecular motion (Fig. 2.10, bottom row).

The echo attenuation is dependent on the characteristics of the applied gradients and the amount of diffusion weighting is commonly quantified using the so-called b-value (Le Bihan et al., 1986), defined thusly for rectangular gradients:

$$b = \gamma^2 G^2 \delta^2 (\Delta - \delta/3) \tag{2.17}$$

where G is the gradient amplitude, δ is the gradient pulse duration, Δ is the time elapsed between the beginning of the first and second gradients, and b has units of s/mm^2. The direction in which the diffusion encoding gradients are applied is called b-vector.

Considering now the effects of relaxation, the retrieved signal will depend not only just on TR and TE, but also on the b-value and b-vector (or simply b). Diffusion acquisitions almost ubiquitously include the measurement of an image at b = 0 s/mm^2, essentially a non-diffusion weighted image, i.e. a T_2-weighted image. This image serves as a reference for all the other images produced at b-values greater than 0, while keeping TR and TE constant. This ensures that the relaxation effects can be ignored so that the retrieved signal can be modelled only as a function of b, and therefore reflect only the effects of diffusion.

In the absence of diffusional barriers - say in a glass of water - diffusion is said to be unrestricted and the displacement of the water molecules can be modelled by a Gaussian function (Einstein, 1905). The average displacement of the molecules after a given time t, $\overline{r(t)}$, is given by

$$\overline{r(t)} = \sqrt{2Dt} \tag{2.18}$$

where D is the diffusion coefficient of the water molecules.

In biological tissues, however, the movement of the water molecules is hindered by the presence of microstructural barriers. These include cell organelles, cell membranes, extracellular matrix, etc. Changes in the tissue microstructure, either due to physiological (e.g. brain development) or pathological (e.g. brain tumour) events, can manifest themselves

in a change of the diffusion properties of the tissue, and, consequently, in the retrieved signal from a dMRI experiment. The signal measured by dMRI allows us therefore to probe microstructural changes that neither T_1-, T_2-, nor T_2^*-weighted images can provide. The next chapter will introduce clinical imaging to the reader and show applications of the different MRI contrasts to a very particular pathology: brain tumour.

3. Brain Tumour Imaging

The term "brain tumour" encompasses a wide variety of entities, with the 2016 WHO brain tumour classification containing over 100 different entries (Louis et al., 2016). Of these, gliomas are by far the most common type of adult brain tumours and they can be sorted into 3 main categories: oligodendrogliomas, astrocytomas, and glioblastomas. These can be further sub-divided into grades which reflect the degree of severity of the tumour, ranging from I (benign, good prognosis) to IV (extremely malignant, very bad prognosis), with grades I and II constituting low grade gliomas (LGGs), and III and IV high grade gliomas (HGGs). Grade assignment depends on histological features like cellularity, nuclear atypia, mitotic activity, pleomorphism, vascular hyperplasia, and necrosis (Louis et al., 2016). While both astrocytomas and oligodendrogliomas can have any grade according to this classification, glioblastomas are all grade IV, with the worse prognosis of all adult brain tumours and a median survival of around 1 year (Stupp et al., 2005; Ostrom et al., 2014).

In vivo brain tumour imaging can be performed with a myriad of techniques, like computerised tomography (CT), MRI, positron emission tomography (PET), etc. One of the hallmarks of malignant tumours is the destruction of the blood-brain barrier (BBB) (Herholz et al., 2012). The BBB is responsible for restricting the passage of macromolecules from the blood in the vessels into the brain. If the BBB is disrupted, its restrictive effect is compromised, resulting in leakage of macromolecules into the brain parenchyma. Through the administration of contrast agents, BBB disruption can be easily seen as hyperintense on both CT and MRI. While CT is the fastest and cheapest of the two, most brain tumour imaging is performed using MRI due to its versatility and superior soft tissue contrast, owed to the wide variety of imaging contrasts. On the other hand, PET, a slower and

logistically more demanding technique, is a highly specific imaging method which offers insights into the metabolism of the brain and metabolic changes due to tumour. Another point that distinguishes MRI is that it has the added benefit of being the only one of the three that does not use ionising radiation to produce the images. In the following sections, an overview of MRI and PET applications to brain tumour imaging will be presented; CT-based applications will not be revised since CT did not play a role in this thesis and is, therefore, outside of its scope.

3.1. MRI in tumours

3.1.1. Clinical MRI

As seen in chapter 2, there are many parameters that influence the quality and contrast of the obtained MR images. Guidelines for brain tumour imaging have been introduced which aim at maximising diagnostic efficiency and homogenising the acquisitions across centres. This has the advantage that images can be more readily pooled in multi-centre studies, in particular in diseases of small incidence. These guidelines include the acquisition of a high resolution 3D T_1-weighted (T_1) image, an axial T_2-weighted (T_2) fluid-attenuated inversion recovery (FLAIR), three axial diffusion-weighted images, an axial T_2 image, and a T_1-weighted post-contrast (T_1C) image with the same acquisition parameters as that of the 3D T1 (Weller et al., 2014; Ellingson et al., 2015; Weller et al., 2021). An example of such an acquisition is shown in figure 3.1

The superior soft tissue contrast of MRI allows it to better assess lesion extent, as it more accurately depicts potential infiltrative regions (Villanueva-Meyer et al., 2017). The acquisition of a T_1 image pre- and post-contrast highlights the disruption of the BBB, evidenced in Fig. 3.1 (Fig. 3.1, first and last tiles, respectively). Contrast enhancement can be a sign of malignancy as it hints towards BBB disruption, however, some high grade tumours show no enhancement whereas some low grade tumours do (Ginsberg et al., 1998; Smirniotopoulos et al., 2007). Images obtained from T_2/FLAIR weighting reveal peritumoural hyperintense lesions typically associated to oedema, i.e. abnormal

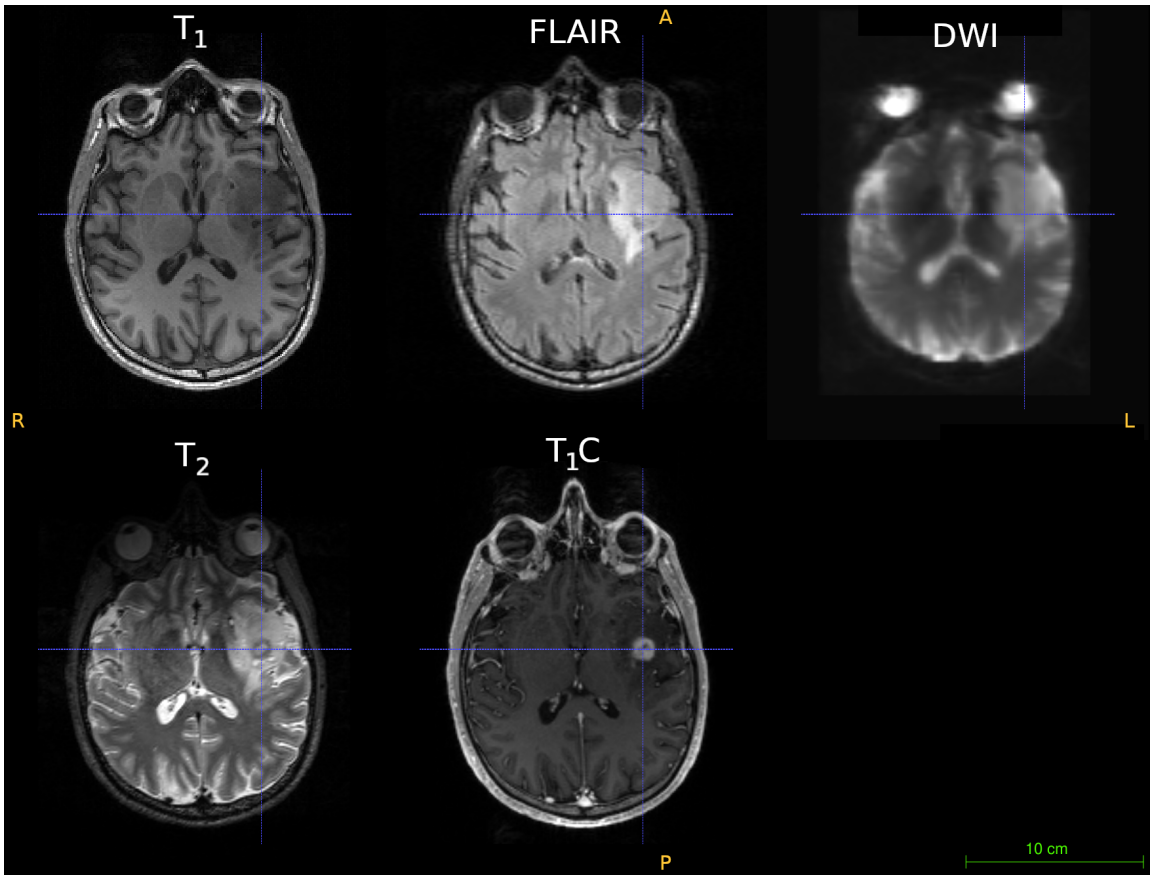

Figure 3.1.: *Standard clinical MRI acquisition example in a 45 year-old male patient with a recurrent glioblastoma in the left insula. The images shown are (top to bottom, left to right): T_1, FLAIR, DWI, T_2, T_1C. The cross-hair is located at the centre of the contrast enhancing lesion of T_1C.*

accumulation of water in the tissues. This oedema can be of either vasogenic or infiltrative nature. Vasogenic oedema arises when extracellular water content increases as a result of plasma leakage from the vessels, without tumour cells. When tumour cells are present, due to their invasion of the extracellular space (ECS) (Goldbrunner et al., 1998), oedema is said to be infiltrative. The T_2/FLAIR hyperintensities are, much like the T_1C enhancement, not very specific, as in some cases the primary lesion can be undistinguishable from the surrounding oedema (Wen et al., 2010; Barajas et al., 2013).

MRI is used routinely in the clinic not only for diagnostic purposes, but also to monitor progression and treatment response. Glioma treatment depends primarily on the grade. Regardless, first line of treatment is usually surgical resection, if possible, and/or some form

of chemoradiotherapy (Stupp et al., 2014; Duffau and Taillandier, 2015; Le Rhun et al., 2016).

Imaging treatment response is not straightforward, as effects of therapy can be confounded with tumour growth. The typical hallmark of progression is an increase in the volume of the contrast enhancing lesion in T_1C and/or an increase in the T_2/FLAIR hyperintense lesion. However, radiation therapy can cause vasodilation, disruption of the BBB, and oedema, such that changes in the MRI can be misinterpreted to be disease progression when in fact they are transient and due to the treatment (de Wit et al., 2004; Brandsma et al., 2008). Such changes, called pseudo-progression, typically resolve on their own but failure to recognise them can lead to undue termination of adjuvant treatment (Wen et al., 2010).

3.1.2. Quantitative MRI

Recently introduced, the WHO tumour classification of 2021 no longer relies mostly on histopathological features but has incorporated both molecular and genetic information to sort out tumour entities and their response to treatment (Louis et al., 2021). The observation that patients diagnosed with the same tumour type develop different responses to the same therapy contributed to the identification of molecular and genetic biomarkers which correlate to treatment response (Louis et al., 2021). The necessity to tailor treatment to the patient, as opposed to the overarching disease type, is now much higher, leading to the development of precision medicine. In order to support it, imaging methods need to be able to provide with precise and accurate information which can help clinicians reach decisions regarding treatment, with the development of such imaging-based biomarkers being the main driving force of the field of quantitative MRI (qMRI). While qMRI has many branches, only few found their way into standard clinical practice, with dMRI being one of them due to its relative ease of use and high clinical relevance.

Diffusion MRI

As introduced in chapter 2, dMRI is an imaging technique sensitive to the Brownian motion of water molecules. The medium in which the molecules navigate modulates their

movement and, through the measurement of the diffusion properties, the underlying tissue microstructure can be inferred. After its introduction in the mid-1980's, dMRI was first introduced in the clinic for stroke imaging, due to its increased sensitivity not only to the infarcted region but also to the penumbra (Moseley et al., 1990; Leigh et al., 2018). It has since been gaining favour among clinicians for its ability to probe microstructural changes and has found its way into brain tumour imaging.

Quantification of diffusion in dMRI is performed typically via the ADC, which assumes the MR signal decays mono-exponentially with b-value (Le Bihan and Brenton, 1985), described by:

$$S_b/S_0 = e^{-bADC} \tag{3.1}$$

with the typical b-value acquired in the clinic being 1,000 s/mm^2.

In the clinical context, dMRI signal is primarily driven by the degree of diffusion in the extracellular space, resulting in the ADC being negatively correlated to cell density and proliferation (Sugahara et al., 1999; Higano et al., 2006).

Generally, in brain tumours, cellularity is positively correlated with tumour grade (Louis et al., 2021), with the increase in cellularity, and thus the increase in relative intracellular volume, leading to the decrease of relative extracellular volume. Additionally, the proliferation of tumour cells through the ECS leads to changes in the diffusion parameters measured in this space, as confirmed by tetramethylammonium-based iontophoresis (Vargová et al., 2003). This means that higher ADC values have been related to LGGs and *vice-versa*. In fact, studies have shown that the ADC is able to distinguish LGG from HGG (Zhang et al., 2017; Wang et al., 2020), with HGG tumours having lower ADC in general; tumour from metastases (Suh et al., 2018); and glioma recurrence from pseudo-progression (Yu et al., 2020). Additionally, ADC has been shown to be sensitive to genetic mutations of prognostic importance (Suh et al., 2019; Aboian et al., 2017).

Beyond the ADC, which only provides a measure of the quantity of diffusion, dMRI based methods imaging the directionality of diffusion can be useful in the determination degree of infiltration of a tumour. Diffusion tensor imaging (DTI) is the most popular of these

methods. By acquiring multiple diffusion directions, a diffusion tensor can be fit in each voxel. A 3D characterisation of the diffusion in the tissues is then obtained, allowing the extraction of quantitative metrics summarising this diffusion.

Despite the multitude of studies showing potential clinical use of DTI-derived metrics, quantitative assessment of these values in clinical routine is scarce. Instead, DTI is most commonly used in the context of surgical planning, making use of a technique called tractography. With it, one can reconstruct the white matter tracts of the brain and assess whether or not there are white matter structures at risk. Since a mechanical damage to these structures is linked to poor recovery, the neurosurgeon uses tractography to avoid damaging the white matter tracts, hence avoiding post-operative functional damage (Weiss Lucas et al., 2022).

3.2. PET in brain tumours

Structural imaging is appealing due to its high image resolution and soft tissue contrast. However, the lack of specificity from the obtained imaging procedure can mean that metabolic processes are often not captured. Metabolic imaging can be achieved using PET, which relies on radioactive tracers. Molecules are chosen to investigate specific metabolic pathways and get tagged with a positron-emitting radioactive isotope, creating a tracer. The activity emitted from this tracer is then captured by the PET scanner and spatially reconstructed to reveal where in the tissue a high concentration of this tracer was absorbed. The two major branches of PET in brain tumour imaging are glucose and amino acid based PET.

3.2.1. Glucose and FDG-PET

Glucose based PET is used to probe the energy cycles of the tissues, with the typical tracer being ^{18}F-fluoro-2-deoxy-D-glucose (FDG). Since tumour cells tend to have an increased energy demand and therefore glucose metabolism, FDG uptake in the tumour region is increased, in particular in highly malignant tumours (Chen, 2007; Herholz et al., 2012). Consequently, this tracer has been shown to be useful in the grading of tumours (Patronas et al., 1983; Delbeke et al., 1995; Kaschten et al., 1998; De Witte et al., 1996), biopsy

guidance (Goldman et al., 1997), and differentiation of recurrence from radiation necrosis (Langleben and Segall, 2000).

Despite this, FDG-PET in the context of brain tumours suffers from the fact that physiological grey matter and inflammatory tissues (even those independent of tumour development) have a relatively high uptake of glucose, which potentially eclipse that of the tumour, particularly in low grade gliomas (Chen, 2007; Olivero et al., 1995). This precludes a proper delineation of the tumour extent, in particular in regions close to the grey matter (Pauleit et al., 2009).

3.2.2. Amino acid and FET-PET

Another way to investigate tumour tissue with PET is through the use of amino acid tracers (Jager et al., 2001). Amino acids play an important role not only in the metabolism of the cell but they are also the building blocks of proteins. Amino acids can be synthesised in the cell or are incorporated via external sources. In order for amino acids to partake in their respective metabolic pathways, cell membrane transport via specific membrane transporters needs to occur, either to import or export amino acids into or out of the cell. In malignant brain tumours, it has been shown that expression of these membrane transporters is increased compared to that of normal brain glial cells (Busch et al., 1959; Isselbacher, 1972; Saier et al., 1988; Haining et al., 2012).

The most popular amino acids for PET imaging are L-[methyl-^{11}C]methionine (MET), 3,4-dihydroxy-6-[^{18}f]-fluoro-L-phenylalanine (FDOPA), and O-(2-^{18}F-fluoroethyl)-L-tyrosine (FET). Comparing the three, the ^{11}C-labelled MET has a much shorter half life than the ^{18}F-labelled FDOPA and FET (20 vs. 110 minutes), which restricts the application of MET to sites with their own means of production. Initially, FDOPA was developed to probe the dopaminergic synthesis within the basal ganglia (Becherer et al., 2003). Its uptake in this region is particularly high, which means it is poorly suited for the delineation of tumours close to these structures. Finally, FET has the added advantage that once the tracer is absorbed into the cell it is not further metabolised (Langen et al., 2003), while

both MET and FDOPA get degraded and integrated into proteins or otherwise partake in further metabolic processes (Singhal et al., 2008).

Comparing FET and FDG in brain tumours, it has been shown that FET is superior to FDG in the delineation of tumours for surgical resection planning and identification of tumour core for biopsy guidance, with FET showing significantly higher uptake in HGG compared to LGG albeit with a small effect size (Pauleit et al., 2009).

4. Modelling of IVIM and non-Gaussian Diffusivity

4.1. Motivation

As seen in the previous chapter, MRI has established itself as the gold standard for non-invasive, *in vivo* brain tumour imaging. Typically, T_1-, T_1C, and T_2-weighted images are acquired. Changes caused by contrast agents are based on alteration in the T_1 relaxation time, and FLAIR contrast is based on the lengthened T_2 relaxation time in the tumour and oedema regions. However, these changes are often measured qualitatively and seldom quantitatively.

On the other hand, qMRI-based acquisitions offer an objective approach by enabling the measurement of parameters that do not depend on the scanner or the scanning protocol, even in different magnetic field strengths. Such a quantitative approach can potentially improve accuracy in tumour lesion assessment, ultimately improving diagnosis (Hattingen and Pilatus, 2016). Furthermore, these techniques facilitate multi-centre and meta-analyses, allowing larger cohort studies to be carried out.

As brain tumours progress, the tissue generally becomes increasingly heterogeneous (Dagogo-Jack and Shaw, 2018). This heterogeneity is mostly present at the microscopic level, due to different cell mutations resulting in distinct microstructural regions (Lengauer et al., 1998). A full characterisation of this range of differentiation is, therefore, very challenging,

This chapter is based on Loução et al. (2021): A Fast Protocol for Multiparametric Characterisation of Diffusion in the Brain and Brain Tumours, Front Oncol. 2021 Sep 21;11:554205. doi: 10.3389/fonc.2021.554205

requiring a multi-parametric approach for effective segmentation and characterisation of tumour.

Several MRI-derived parameters, such as T_1, T_2, T_2^*, chemical exchange saturation transfer, magnetisation transfer, and dMRI, can be used to probe relevant aspects of the brain's micro-environment and its alterations due to tumours (Villanueva-Meyer et al., 2017; da Silva et al., 2018; Tozer et al., 2011; Maier et al., 2010). Among these, dMRI is particularly valuable due to its sensitivity to different regimes of water mobility, thus capturing microscopic environments of varying characteristic lengths, well below the voxel dimension (Le Bihan and Brenton, 1985).

A traditional dMRI experiment assumes that diffusion within tissue is Gaussian (Tanner and Stejskal, 1968), resulting in a mono-exponential signal decay. This decay is then described by:

$$\frac{S_b}{S_0} = e^{-bD_{app}} \tag{4.1}$$

where b represents the diffusion weighting value (b-value), S_b and S_0 denote the magnitude of the signal at diffusion weighting b and 0 s/mm^2, respectively, and D_{app} is the apparent diffusivity (Le Bihan and Brenton, 1985).

4.1.1. Expansion of the mono-exponential model

IVIM

At low b-values, the diffusion-weighted signal displays a fast-decaying component, which is often considered as a result of the water moving within randomly oriented capillaries. This phenomenon was introduced in (Le Bihan et al., 1988) and is known as intravoxel incoherent motion (IVIM). The signal equation encompassing the IVIM signal is then:

$$\frac{S_b}{S_0} = fe^{-bD^*} + (1-f)e^{-bD_{app}} \tag{4.2}$$

where $f$is the perfusion fraction, D^* is the pseudo-diffusion coefficient, and D_{app} the apparent diffusivity. In previous works, $f$has been considered to be related to cerebral blood volume

(CBV) obtained from dynamic susceptibility contrast (DSC) measurements; the product f.D^* relates to cerebral blood flow (CBF) (Le Bihan and Turner, 1992). Due to the relatively small contribution of D^* to the signal in brain tissues (approximately 10% (Federau et al., 2012)), its effects are no longer evidenced even at moderately low b-values ($b > 200$ s/mm^2). This results in a degeneration of Eq. 4.2 into the mono-exponential of Eq. 4.1, leading to the apparent diffusivity (D_{app}) being the most commonly considered quantity of water diffusion in the tissues.

Due to the presence of microscopic barriers, the motion of water molecules is hindered, resulting in the D_{app} of water in tissue to be reduced by a factor of three or more, compared to that of free water. This restricted regime is, however, still described by Gaussian diffusion, characterising the hindered motion of water in the extracellular space.

Non-Gaussian diffusivity

Not only is Eq. 4.1 limited by an lower b-value, it is also limited by an upper b-value. For $b > 1,000$ s/mm^2, diffusion is no longer considered Gaussian (Maier and Mulkern, 2008; Jensen et al., 2005; Jensen and Helpern, 2010), due to the high heterogeneity of the microstructure: regions containing many restrictive barriers to diffusion lead to slow diffusion, while regions with sparse barriers lead to high diffusion (Kärger, 1985; Maier and Mulkern, 2008). At the voxel level, the convolution of these domains leads to the observation of non-Gaussian diffusion (NG-diff). This behaviour, however, is only seen when measuring large b-values ($> 3,000$ s/mm^2) (Maier and Mulkern, 2008).

In the intermediate range of b-values, deviations from Gaussian-diffusion can be characterised by describing the first-order expansion of Eq. 4.1, a formalism known as diffusion kurtosis imaging (DKI) (Jensen et al., 2005). This expansion is defined thusly:

$$\frac{S_b}{S_0} = e^{-bD_{app}+\frac{1}{6}b^2D_{app}^2K_{app}} \tag{4.3}$$

where apparent kurtosis (K_{app}) is the apparent diffusion kurtosis coefficient. The different regimes are shown in Fig. 4.1.

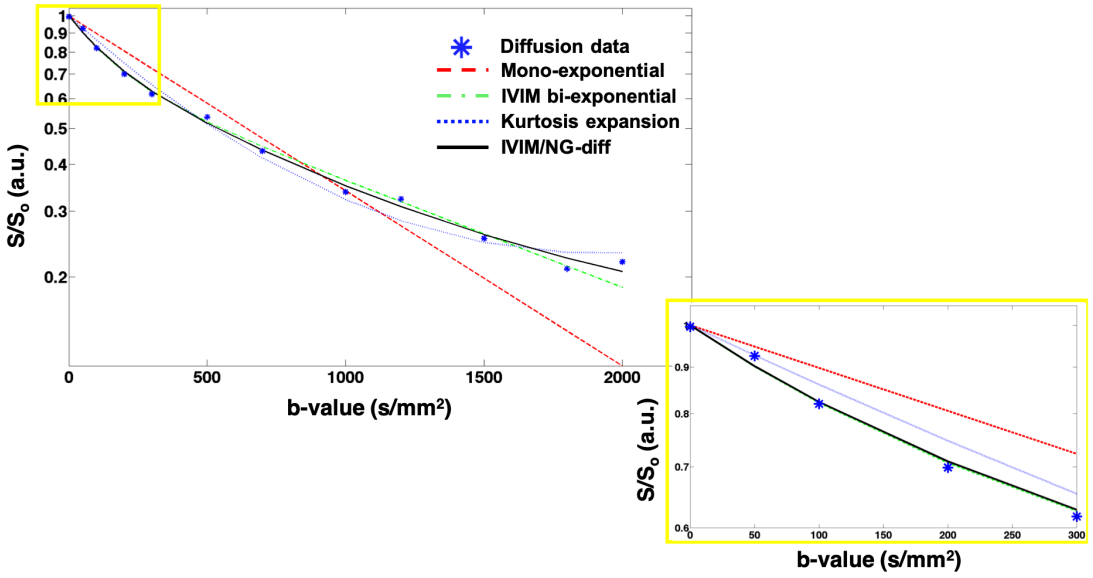

Figure 4.1.: *Diffusion signal decay* vs. *b-value between 0 and 2,000 s/mm^2. The blue stars represent the measured diffusion signal, while the lines represent a fitted curve taking into account: a mono-exponential (red dashed), a IVIM bi-exponential (green dash dotted), a kurtosis expansion (blue dotted), and a combined IVIM/NG-diff (green line) modelling approach. At lower b-values (0-200 s/mm^2- bottom right inset), the influence of the IVIM effect is apparent, while at the higher ones (1,500-3,000 s/mm^2), a deviation from the mono-exponential can be seen, as a consequence of non-Gaussianity (kurtosis).*

In tumour assessment, both the complexity of the microstructure and tissue irrigation are important features to consider. Due to the rapid growth of tumour cells, angiogenesis - that is, the growth of new blood vessels - is promoted in and around the lesion (Jain et al., 2007). Through the injection of contrast-agent, high temporal resolution DSC can be used to investigate tissue irrigation, with increases in CBF, derived from DSC, being associated with tumour regions (Svolos et al., 2014; Verger et al., 2017). Beyond irrigation, previous studies on tissue microstructure have suggested that mean kurtosis (MK) holds brain tumour grading capabilities, as it is more sensitive to the tissue microstructural changes compared to mean diffusivity (MD) as obtained from DTI (Qi et al., 2017; Jiang et al., 2015; Van Cauter et al., 2012).

The acquisition of the images used to compute these parameters is often performed in separate and either require the administration of a contrast agent (as in DSC) or acquisition times that are prohibitively long for standard clinical examinations (as is the case of a fully-sampled DKI protocol). To circumvent these limitations, a fast hybrid IVIM/NG-diff

protocol is proposed here. The goal is to deliver complementary parameters, reflecting both the microstructural (MD and MK) and the irrigation ($f$and D^*) changes, in a clinically acceptable measurement time. Ultimately, this enables a multi-parametric characterisation of tumour tissue, potentially enhancing diagnostic accuracy, staging, and treatment planning.

4.2. Methods

4.2.1. *In vivo* imaging

This study included 17 brain tumour patients (seven female, with a mean age of 46.2 ± 12.4 years). Ethical approval was obtained from the University Hospitals of Aachen, Cologne, and Düsseldorf in accordance with the requirements of the local ethics committees. Written, informed consent was provided by the patients before undergoing the imaging procedures.

Patients were referred to the Institute of Neuroscience and Medicine of the Research Centre Jülich from the above-mentioned hospitals to undergo simultaneous PET-MRI scans. The measurements were performed in a hybrid Siemens (Erlangen, Germany) scanner, based on a 3T Tim-TRIO MR system with a BrainPET insert (Herzog et al., 2011). The MRI dataset comprised standard clinical protocols, including high-resolution volumetric T_1 before and after gadolinium contrast ($T_1$and T_1C), high-resolution volumetric T_2, FLAIR, and DSC. Given the 50-minute duration imposed by the PET acquisition, research protocols can be measured after the clinical ones until the prescribed duration of the PET measurement is over, which included quantitative MRI scans, such as DKI, multi-echo gradient echo (meGRE), further described elsewhere (Oros-Peusquens et al., 2017), and the proposed protocol (IVIM/NG-diff).

For the proposed protocol, imaging parameters were: spin-echo echo planar imaging (SE-EPI) with TR/TE = 5100/92 ms, 3 orthogonal diffusion directions and 16 b-values (0, 50, 100, 200, 300, 500, 700, 1000, 1200, 1500, 1800, 2000, 2200, 2500, 2700, and 3000 s/mm^2), with a voxel size of 2x2x2 mm^3, 24 slices with a 1.4 mm slice gap, covering a FOV of 220x156 mm^2, partial Fourier coverage of 5/8, iPAT of 2, and bandwidth of 909Hz/pixel, resulting in an acquisition time of four minutes 19 seconds.

For comparison, a DKI protocol was adapted from a clinically validated one used at the institute for brain tumour assessments. This protocol was slightly modified to reduce distortions and echo time, matching the FOV and the orientation of the trace-base acquisition, while the bandwidth was increased to the limit allowed by duty cycle constraints. The DKI dataset was based on a SE-EPI with TR/TE = 4000/115 ms, BW = 1299Hz/pixel, without iPAT, 3 non-zero b-values (1000, 2000, and 3000 s/mm^2), each with 30 non-collinear diffusion directions. A FOV of 220x160 was used, with the same voxel size, number of slices, slice gap, and Fourier coverage as the proposed protocol. The acquisition time was six minutes and one second.

For perfusion assessment, a contrast-enhanced DSC T_2^*-weighted sequence was used. Single-shot EPI was used with TR/TE = 1500/32 ms, a voxel size of 1.79x1.79x5 mm^3, 20 slices with a 1.75 mm slice gap and an image matrix of 128×128. The contrast agent (GdDTPA) was administered using a power injector (Injektron 82 MRT, Medtron AG) at a dose of 0.1 mmol/kg of bodyweight at a flow rate of 5 mL/s. Images were acquired continuously for one minute.

Simultaneously with the MR protocols, amino acid FET PET scans were acquired. The amino acid was synthesised via nucleophilic ^{18}F fluorination with radiochemical purity above 98%, specific radioactivity greater than 200 GBq/mol, and a radiochemical yield of around 60% (Hamacher and Coenen, 2002).

4.2.2. Image pre-processing

The complete image processing pipelines are outline in 4.2-a). The initial step was a visual quality assurance on all datasets included in this study across all patients.

Noise reduction was then applied on the multi-contrast diffusion data obtained from either the diffuson-based protocols, using a PCA-based algorithm (Jolliffe, 2002). This algorithm has been previously described for other types of multi-contrast acquisitions (Bydder and Du, 2006; Oros-Peusquens and Shah, 2013) and shares similarities to that proposed by (Veraart et al., 2016a) – for further details, see 4.4.1.

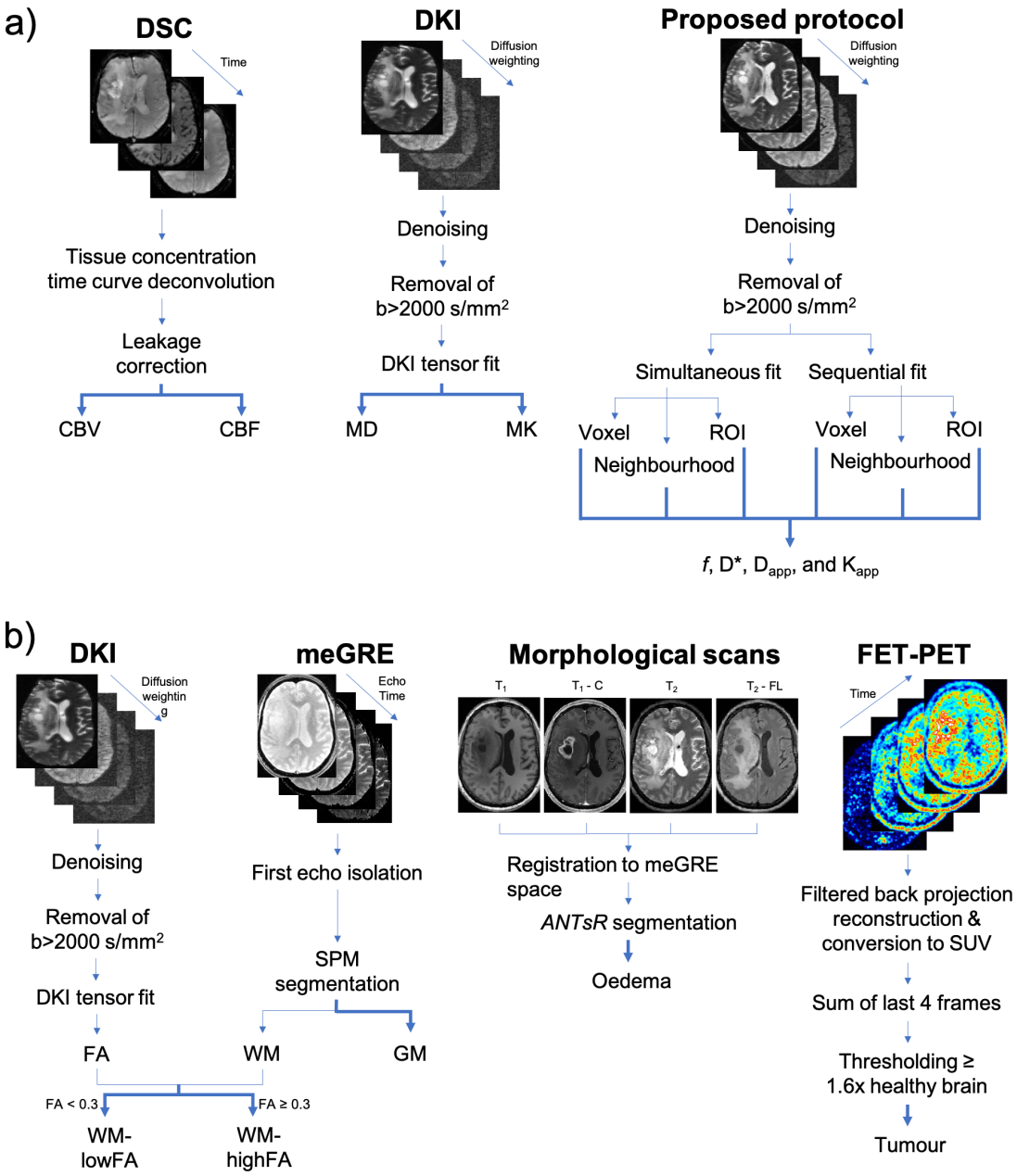

Figure 4.2.: *Image processing diagrams. (a) Processing steps leading to the estimated diffusion metric maps. (b) Processing steps leading to the tissue masks.*

For the DKI data, motion and eddy current artefacts were corrected using FSL's *eddy* (Andersson and Sotiropoulos, 2016), followed by Gaussian filtering with full-width-half-maximum of 1.5 and a kernel size of 3x3x3 voxels.

For the trace-based protocol, motion and eddy current compensation was performed using FSL's *eddy_correct* (Andersson et al., 2003), due to the lack of diffusion weighting orientation information. A Gaussian filter with the same properties as that used for the DKI data was subsequently applied. Finally, the noise floor was removed from the images by subtracting the average signal of the corner voxels of the image.

Parallel imaging with factor iPAT=2 was used for the trace-based protocol to help reduce the susceptibility-induced distortions, so that the performance of the two different algorithms (*eddy* and *eddy_correct*) on the two different datasets yielded very comparable results.

4.2.3. Data processing

Diffusion data fitting

The DKI data were used to estimate both the diffusion and kurtosis tensors, as well as several rotationally invariant metrics, including MD, MK and fractional anisotropy (FA), using United DKI (Neto Henriques et al., 2015).

Conversely, the IVIM/NG-diff data were fit using three different approaches: a simultaneous fit, a sequential fit, and a region of interest (ROI)-based fit.

The sequential fit estimated D_{app} from Eq. 4.2, using the assumption that the IVIM effect is negligible at b < 200 s/mm^2, turning the signal equation into

$$\frac{S_b}{S_0} = (1-f)e^{-bD_{\text{app}}} \tag{4.4}$$

Rearranging these terms, the logarithm of the signal can be taken, resulting in

$$log(S_b) = -bD_{\text{app}} + const. \tag{4.5}$$

where

$$const = log(S_0(1-f)) \tag{4.6}$$

Equation 4.5 is a straight line with slope D_{app}. Using two data points within the valid b-value range (200-1,000 s/mm^2), D_{app} can be calculated by

$$D_{\text{app}} = -\frac{log(S_{b_2}) - log(S_{b_1})}{b_2 - b_1} \tag{4.7}$$

where b_1 and b_2 were empirically set at 500 and 1000 s/mm^2, respectively. Once D_{app} has been determined, f can be obtained by substituting D_{app} in Eq. 4.4, yielding

$$f = 1 - \frac{S_{b_2}}{S_0} e^{b_2 D_{\text{app}}} \tag{4.8}$$

Following that, D^* can be calculated by revisiting Eq. 4.2 and expanding the b-value range (0 to 1,000 s/mm^2). Rearranging Eq. 4.8, one obtains

$$S_0.f = S_0 - S_{b_2} e^{b_2 D_{\text{app}}} \tag{4.9}$$

and

$$1 - f = \frac{S_{b_2}}{S_0} e^{b_2 . D_{\text{app}}} \tag{4.10}$$

Plugging Eqs. 4.9 and 4.10 in Eq. 4.2 allows the D^* term to be derived:

$$D^* = \frac{log(S_0 - S_{b_2} e^{b_2 D_{\text{app}}}) - log(S_{b_3} - S_{b_2} e^{b_2 - b_3 D_{\text{app}}})}{b_3} \tag{4.11}$$

where b_3 was empirically set to 50 s/mm^2, since, among the b-values sampled, it is the one in which the IVIM effect is expected to be the most prominent.

Finally, K_{app} is estimated using a constrained variation of the Nelder-Mead simplex algorithm (Lagarias et al., 1998), applied to Eq. 4.3 using the signal from the b-values ranging from 800 to 2,000 s/mm^2, using the function $fminsearch$ of MATLAB (R2014a, MathWorks, Massachussets, USA).

The simultaneous fitting approach estimated all four parameters simultaneously (f, D^*, D_{app}, and K_{app}) using the above mentioned constrained fitting routine. The target signal equation was set to

$$\frac{S_b}{S_0} = fe^{-bD^*} + (1-f)e^{-bD_{app}+\frac{1}{2}b^2D_{app}^2K_{app}} \tag{4.12}$$

The constraints were used to mitigate the effects of local minima, as well as to guarantee that each fitted parameter was biologically plausible, based on existing literature. The perfusion fraction, *f*, was set to be between 0 and 0.3, D^* between 0.004 and 0.05 mm^2/s (Federau et al., 2012), D_{app} between 0.0001 and 0.003 mm^2/s, and K_{app} between 0 and 3 (Lätt et al., 2013).

Both the sequential and simultaneous routines were performed voxel-by-voxel (single voxel fit) and on a kernel basis (neighbourhood fit). In the latter, signal decays from an in-slice 3x3 neighbourhood were averaged before fitting.

The third fitting approach, ROI-based fitting, averaged signals from specific tissue classes (see 4.2.4). The averaged signal was fitted to different models (mono-exponential, kurtosis expansion, IVIM bi-exponential, and IVIM/NG-diff), in order to investigate the added value of the additional terms describing non-Gaussian diffusion when SNR is sufficiently high. The fitting parameters were obtained using the simultaneous approach, and an additional sequential fitting was also performed when fitting Eq. 4.12.

The fitting routines were performed on a MacBook Pro (early 2015), with an Intel Core i5 2.7GHz processor and 16GB of RAM.

Additional image processing

DSC data were processed using in-house built routines, as described in (Caldeira et al., 2019). The tissue concentration time curve was deconvoluted from the measured signal using singular value decomposition, with the arterial input function derived automatically (Leu et al., 2016). Signal was corrected for leakage and maps of CBV and CBF were generated.

PET data were reconstructed using a 3D filtered back-projection algorithm and expressed as standard uptake value (SUV) (Pauleit et al., 2005).

All resulting maps were warped to the DKI space using affine transformations determined by SPM12, with visual quality control performed at each step.

4.2.4. Tissue classes

The proposed protocol's performance was evaluated across multiple tissue types. For each subject, masks were generated for five tissue classes: normal-appearing grey matter (GM), normal appearing white matter with either low or high FA (WM-lowFA and WM-highFA, respectively), tumour, and oedema. The flowcharts in Fig. 4.2-b) provide an overview of the process.

First, the lesioned and normal-appearing hemispheres where identified based on information from the clinical protocols, DKI, and PET.

Normal-appearing GM and WM probability maps were obtained using the meGRE images and SPM12's united segmentation (Ashburner and Friston, 2005). A threshold of 98% was applied to generate the GM and WM masks, which were then co-registered to the DKI space. The WM class was further subdivided into low FA ($0.05 < \text{FA} < 0.3$), and high FA ($\text{FA} \geq 0.3$), based on the DKI-fitting of the standard protocol. This was done to reflect different microscopic fibre arrangements: in WM regions of low FA, fibre arrangements are complex, e.g. crossing or fanning fibres, which present as isotropic diffusion at the voxel level; conversely, WM regions of high FA contain fibres which are very well aligned, resulting in highly anisotropic diffusion.

Active tumour tissue was identified using high-SNR data obtained from the sum of the last four frames of the dynamic ^{18}F-FET scans. Voxels with an intensity 1.6x equal or higher than that of normal tissue were considered to be active tumour (Pauleit et al., 2005).

Oedema masks were obtained using the morphological data (T_1, T_1C, T_2, and FLAIR) on the ANTsR framework (Tustison et al., 2015), trained on data from the BRATS 2015 challenge, available from the Sicas Medical Image Repository (www.smir.ch) (Kistler et al., 2013).

This process led to the creation of five masks (GM, WM- lowFA, WM-highFA, tumour and oedema), which might not be mutually exclusive, either due to multiple resolutions or thresholding. Mask overlap was resolved in one of two ways: voxels belonging to both tumour and oedema masks were assigned to tumour; voxels belonging to multiple healthy appearing tissues were removed from the analysis.

4.2.5. Simulations

Simulations were conducted to assess the impact of noise, tissue-specific parameters and fitting procedures on IVIM/NG-diff metrics estimation. Using the same b-value array used in the *in vivo* acquisition, theoretical signals was generated from Eq. 4.12 for all five tissue classes (ground truths were taken from the results of the ROI-based fit - see Table 4.1). A noisy signal was generated by adding a noise contribution according to

$$S_N = \sqrt{(S_T + \eta_{Re}^2) + \eta_{Im}^2} \tag{4.13}$$

where S_T is the theoretical tissue signal and η_{Re} and η_{Im} are the real and imaginary noise components, respectively, determined based on a Gaussian distribution with zero mean and standard deviation of 1/SNR. From each theoretical tissue, 10,000 independently drawn noisy signals were fitted at different SNR levels (ranging from 20 to 60, in increments of 10), using the simultaneous and sequential routines (see 4.2.3). The accuracy and precision of each fitting procedure were then assessed.

4.2.6. Statistical analyses

Spearman's ρ correlation coefficients were calculated to compare the IVIM/NG-diff metrics (f, f.D*, $\mathrm{D_{app}}$, and $\mathrm{K_{app}}$) with their canonical counterparts (CBV, CBF, MD, and MK, respectively).

The corrected Akaike's information criterion (AICc) (Akaike, 1998) was used to evaluate the goodness of fit at the tissue class level. The AICc is given by

$$AICc = nlog(\hat{o}^2) + 2k + \frac{2k(k+1)}{n-k-1} \tag{4.14}$$

where n is the number of samples used in the fit, k are the degrees of freedom in the model, and $\hat{o}^2$ is the mean squared error, given by

$$\hat{o}^2 = \frac{1}{n}\sum_{i=1}^{n}\epsilon_i^2 \tag{4.15}$$

Lower AICc shows an improved relationship between the residuals of the fit and the information gain, i.e., models that represent the data better will have a comparatively smaller AICc.

Differences in the means of the metrics derived from the sequential and simultaneous tissue class level fitting to Eq. 4.12 were tested at the different SNR levels using the Wilcoxon signed-rank test. Reproducibility was assessed by calculating the coefficient of variation (CV) for each parameter obtained from the simulations, defined by

$$CV = \frac{\sigma}{\mu} \tag{4.16}$$

where σ and μ are the standard deviation and the mean, respectively, of the distributions for each metric.

All statistical analyses were carried out in MATLAB, with significance set at p-value $<$ 0.05.

4.3. Results

4.3.1. Noise reduction

The effects of the denoising algorithm are illustrated in Fig. 4.3, showing a representative slice taken from a brain tumour patient of both the DKI and IVIM/NG-diff protocols. From left to right, the images display a slice at b = 3000 s/mm^{2}for each acquisition, along with the maps for D*, f,D$_{\text{app}}$, and K$_{\text{app}}$derived from the simultaneous fit. The signal decay of a WM-highFA voxel is plotted against the b-value for both the noisy (blue) and denoised (red) images.

4.3.2. *In vivo* imaging

Average voxel-wise computation time of the fitting routines was 4.6 $\pm$ 0.8 ms for the sequential and 27.7 $\pm$ 9 ms for the simultaneous fitting.

Figure 4.4 presents maps of the five parameters estimated from the proposed protocol, showing the simultaneous fit in the upper block, the sequential fit in the middle block, and

the canonical counterparts in the lower block, for a representative patient and slice. The corresponding FET-PET slice is also included in the bottom left corner.

The tissue class fitting results are summarised in Table 4.1, listing the mean ± standard deviation values across all patients for both fitting routines. The IVIM parameters derived from the are generally lower compared to those from the sequential fit, whereas the tissue D_{app} are higher. Statistically significant differences were found for f and D_{app} across all tissues, and for D^* in GM (Wilcoxon signed-rank test, p-value < 0.05).

Table 4.2 summarises the mean ± standard deviation of the IVIM/NG-diff metrics per tissue class per fit across all subjects, alongside their canonical counterparts. The root mean squared error (RMSE) and the AICc of the tissue level fits are shown in Table 4.3.

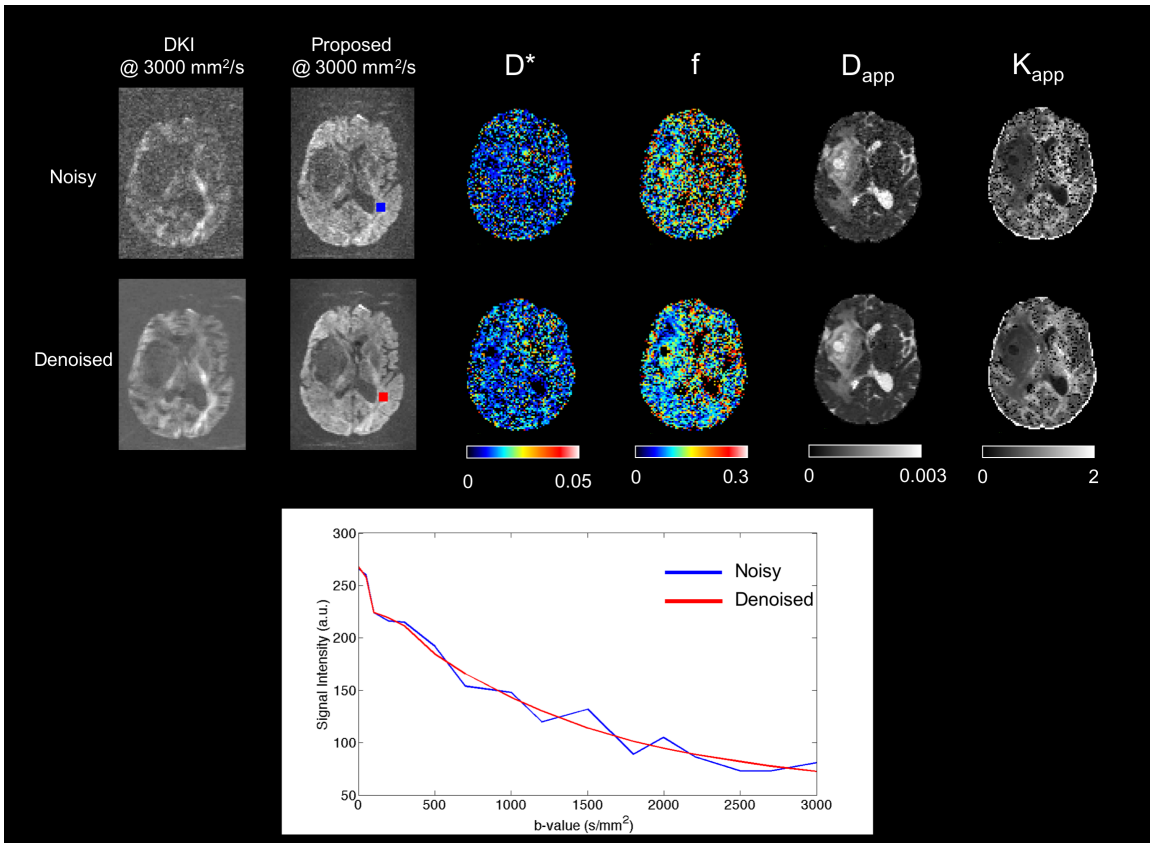

Figure 4.3.: *Denoising effect on diffusion signal, images, and maps. On the top row are depicted the images/maps from the DKI acquisition, while on the bottom row are those from the proposed protocol, without Gaussian filter. The plot beneath depicts the signal decay of a white matter voxel: before (blue) and after (red) denoising. As the b-value increases, the influences of the denoising also increase.*

Fig. 4.5 shows the voxel-by-voxel ratio histograms for D_{app}/MD and K_{app}/MK, with the orange line representing a ratio of 1.

In Fig. 4.6 are shown two brain tumour examples, one LGG and one HGG, together with the respective metrics derived from the proposed protocol.

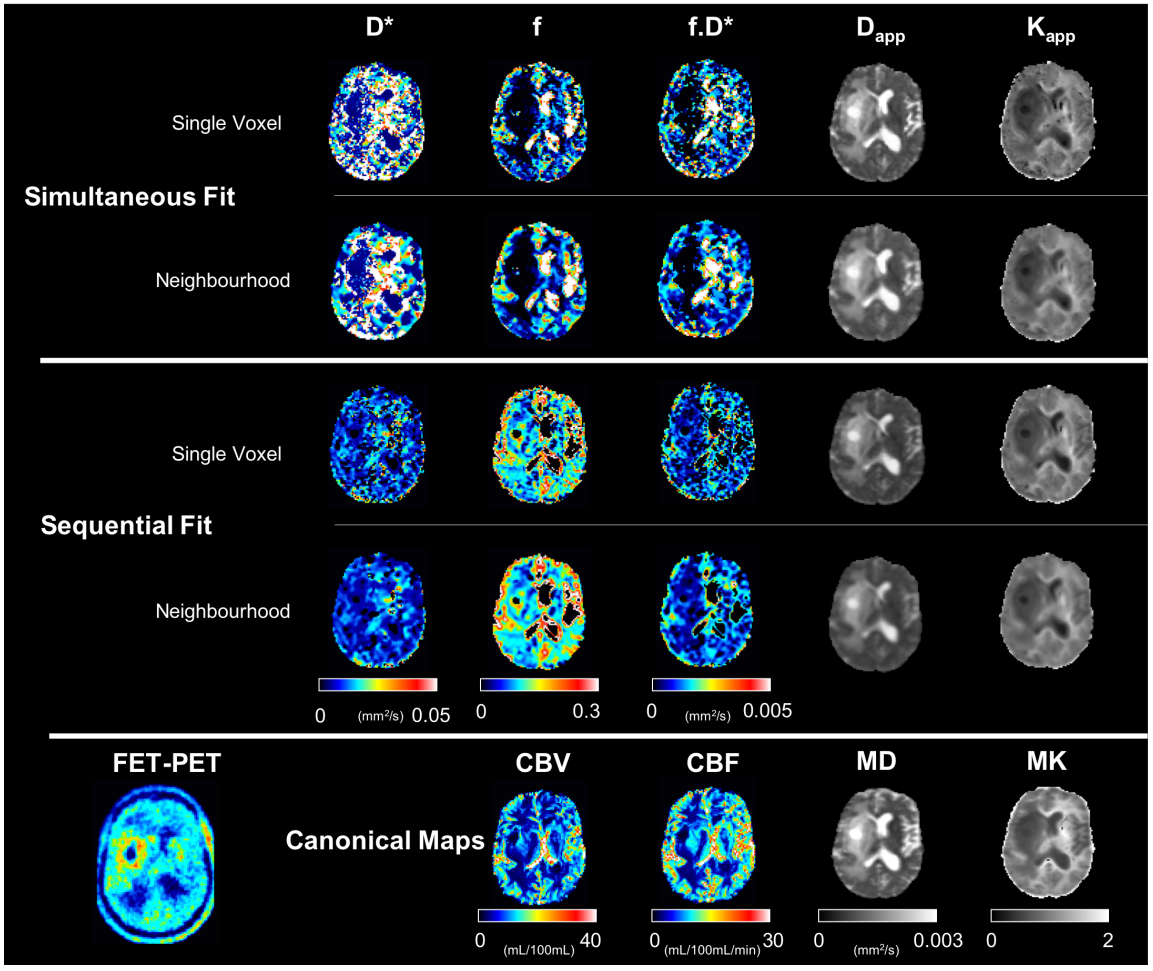

Figure 4.4.: *Estimated maps derived from the proposed protocol for a representative subject, using all fitting approaches. The respective canonical counterparts are shown at the bottom, together with the corresponding FET-PET slice. Colour bars for each metric are the same.*

Table 4.1.: *Cohort level averages of the ROI-based fitting of both routines to the IVIM/NG-diff model (Eq. 4.12). The routines showed significantly different results for* f *and* D_{app} *in all tissues, and in* D_{app} *in GM, (p-value < 0.05).*

	Simultaneous Fit				
	GM	WM-lowFA	WM-highFA	Oedema	Tumour
f	0.13 ± 0.04	0.03 ± 0.02	0.03 ± 0.01	0.03 ± 0.02	0.01 ± 0.01
D^* (x10^{-3} mm^2/s)	8.43 ± 2.65	21.6 ± 12.5	23.0 ± 13.8	29.0 ± 15.0	29.5 ± 17.8
D_{app} (x10^{-3} mm^2/s)	1.12 ± 0.12	0.94 ± 0.05	0.88 ± 0.04	1.42 ± 0.22	1.38 ± 0.41
K_{app}	0.83 ± 0.04	1.03 ± 0.04	1.12 ± 0.05	0.74 ± 0.11	0.72 ± 0.22
	Sequential Fit				
	GM	WM-lowFA	WM-highFA	Oedema	Tumour
f	0.20 ± 0.04	0.10 ± 0.02	0.10 ± 0.01	0.14 ± 0.04	0.11 ± 0.01
D^* (x10^{-3} mm^2/s)	12.2 ± 1.46	17.6 ± 3.89	17.7 ± 2.63	20.0 ± 9.30	25.9 ± 11.0
D_{app} (x10^{-3} mm^2/s)	0.86 ± 0.06	0.71 ± 0.03	0.66 ± 0.02	1.05 ± 0.15	1.06 ± 0.32
K_{app}	0.83 ± 0.03	1.02 ± 0.04	1.11 ± 0.05	0.73 ± 0.10	0.72 ± 0.22

Table 4.2.: *Mean ± standard deviations for the voxel- and neighbourhood-based estimated parameters at cohort level. Parameters from the standard protocols are shown at the bottom, aligned with their counterparts from the proposed protocol.*

	f					$f.D^*$ (x10^{-4} mm^2/s)					D^* (x10^{-3} mm^2/s)				
	GM	WM-lowFA	WM-highFA	Oedema	Tumour	GM	WM-lowFA	WM-highFA	Oedema	Tumour	GM	WM-lowFA	WM-highFA	Oedema	Tumour
Simultaneous Fit	0.13 ± 0.02	0.06 ± 0.01	0.05 ± 0.01	0.03 ± 0.02	0.06 ± 0.03	21.4 ± 6.08	14.9 ± 5.24	13.9 ± 1.88	9.65 ± 5.29	18.8 ± 3.25	26.3 ± 6.35	37.5 ± 4.98	41.2 ± 4.96	36.3 ± 9.91	37.0 ± 8.34
Sequential Fit	0.14 ± 0.01	0.11 ± 0.01	0.10 ± 0.01	0.09 ± 0.02	0.12 ± 0.03	11.4 ± 0.96	9.11 ± 0.89	8.85 ± 0.80	6.82 ± 1.84	9.70 ± 1.70	8.37 ± 1.18	8.38 ± 0.73	8.57 ± 0.78	7.52 ± 1.33	8.65 ± 1.00
Neighbourhood Simultaneous Fit	0.14 ± 0.03	0.07 ± 0.02	0.05 ± 0.01	0.03 ± 0.02	0.06 ± 0.03	19.6 ± 5.95	12.5 ± 3.19	11.0 ± 2.05	7.98 ± 4.79	11.7 ± 3.04	20.8 ± 6.26	31.8 ± 6.47	37.2 ± 6.73	37.0 ± 11.4	37.7 ± 10.8
Neighbourhood Sequential Fit	0.15 ± 0.01	0.12 ± 0.01	0.10 ± 0.01	0.10 ± 0.02	0.13 ± 0.03	12.0 ± 0.97	8.73 ± 1.12	7.98 ± 0.92	6.73 ± 1.73	9.68 ± 1.78	8.08 ± 1.17	7.42 ± 0.83	7.48 ± 0.82	7.11 ± 1.34	8.00 ± 1.07
Canonical Metrics	18.5 ± 2.37	11.7 ± 2.30	9.88 ± 1.71	7.47 ± 4.64	12.7 ± 5.76	17.0 ± 8.34	10.3 ± 5.10	8.62 ± 4.23	9.21 ± 4.47	16.9 ± 4.11					
	CBV (mL/100mL)					**CBF (mL/100mL/min)**									

	D_{app} (x10^{-3} mm^2/s)					K_{app}				
	GM	WM-lowFA	WM-highFA	Oedema	Tumour	GM	WM-lowFA	WM-highFA	Oedema	Tumour
Simultaneous Fit	0.90 ± 0.23	0.88 ± 0.05	0.85 ± 0.04	1.20 ± 0.26	1.20 ± 0.29	0.80 ± 0.03	1.00 ± 0.05	1.06 ± 0.05	0.68 ± 0.14	0.66 ± 0.12
Sequential Fit	0.69 ± 0.19	0.66 ± 0.03	0.97 ± 0.03	0.97 ± 0.19	0.79 ± 0.21	0.79 ± 0.03	0.99 ± 0.04	1.06 ± 0.05	0.69 ± 0.13	0.70 ± 0.12
Neighbourhood Simultaneous Fit	0.92 ± 0.24	0.91 ± 0.05	0.87 ± 0.04	1.26 ± 0.22	1.24 ± 0.22	0.82 ± 0.04	0.99 ± 0.04	1.06 ± 0.05	0.69 ± 0.13	0.70 ± 0.11
Neighbourhood Sequential Fit	0.74 ± 0.19	0.70 ± 0.03	0.67 ± 0.03	1.00 ± 0.21	1.00 ± 0.21	0.81 ± 0.03	0.98 ± 0.04	1.05 ± 0.04	0.70 ± 0.13	0.70 ± 0.11
Canonical Metrics	1.13 ± 0.22	0.91 ± 0.06	0.85 ± 0.05	1.31 ± 0.30	1.32 ± 0.24	0.89 ± 0.06	1.21 ± 0.08	1.35 ± 0.06	0.79 ± 0.16	0.81 ± 0.18
	MD (x10^{-3} mm^2/s)					**MK**				

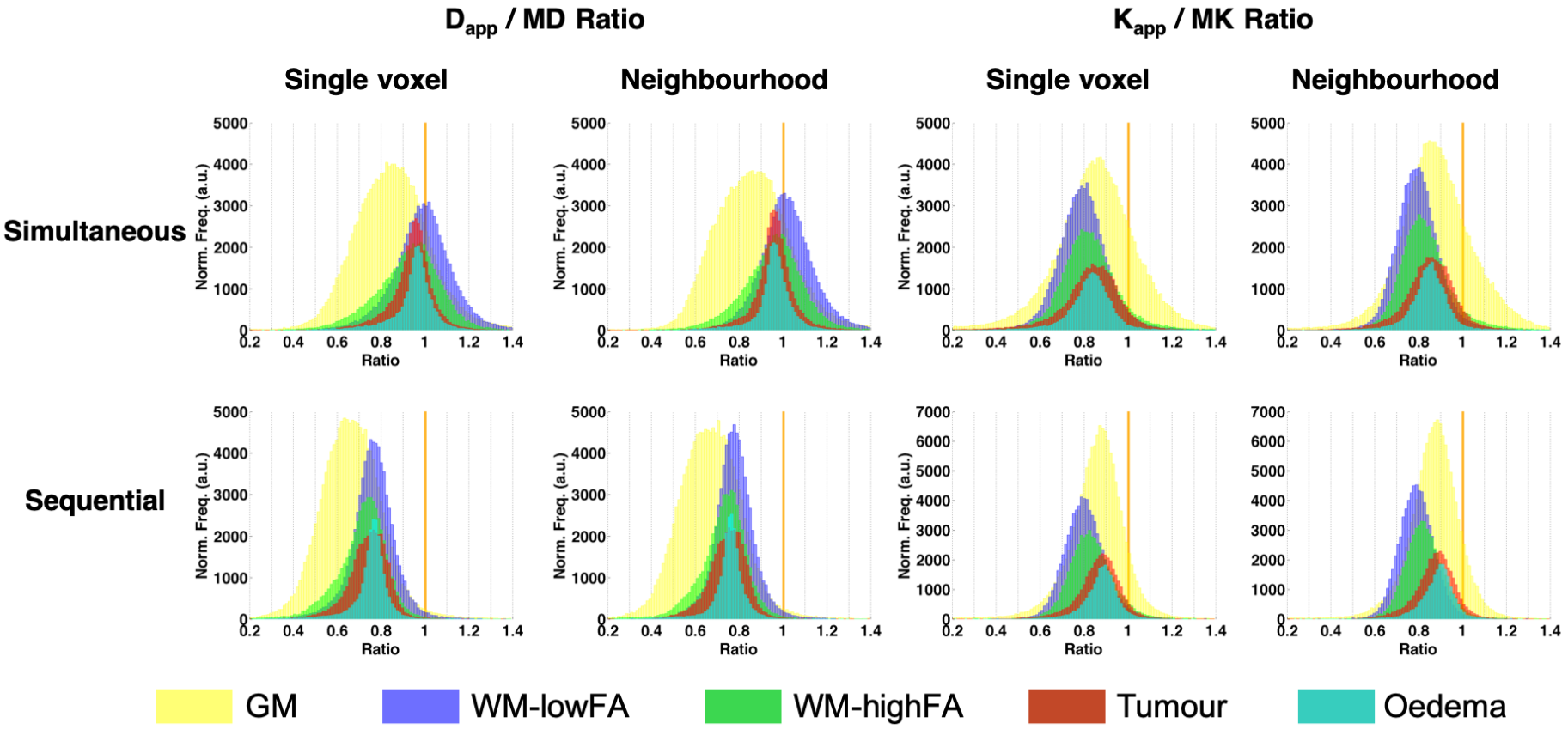

Figure 4.5.: *Histograms of the ratios D_{app}/MD and K_{app}/MK. A ratio of 1 is indicated by the vertical orange line.*

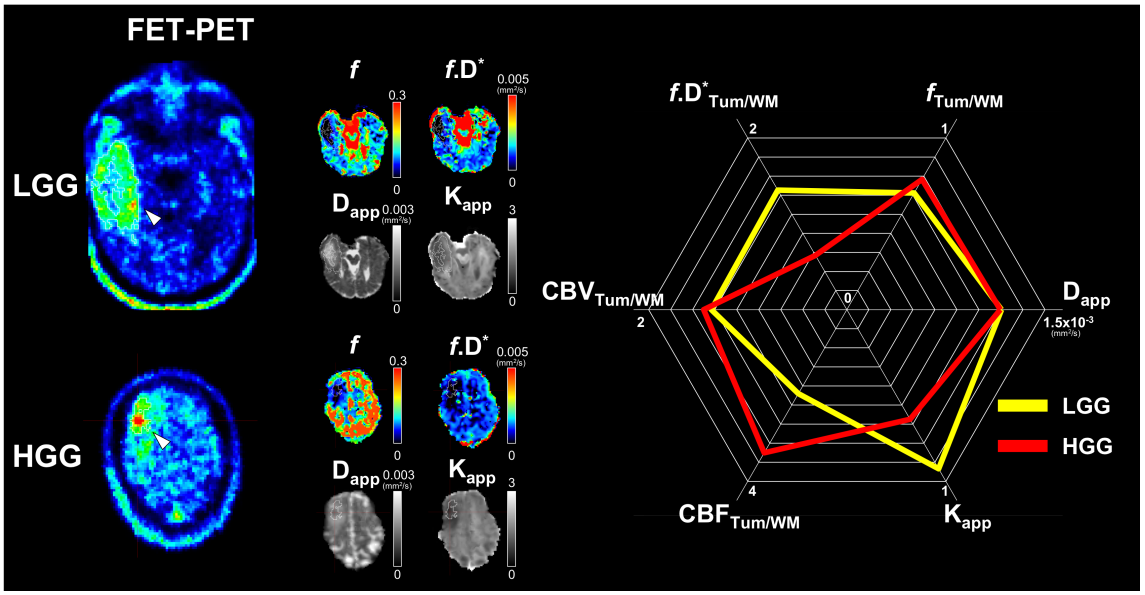

Figure 4.6.: *Comparatve example of two brain tumour patients (LGG and HGG). An FET-PET slice showing a region of high uptake (white arrow) is shown on the left the corresponding slices of the maps from the proposed protocol estimated from the mean neighbourhood fit are shown beside them. On the right hand side, the multi-parametric signature of the respective tumours shown on the left is presented. Such approaches could be used to identify biomarker combinations of high and low grade tumours.*

The Spearman ρ correlation coefficients are summarised in Table 4.4. IVIM and DSC metrics showed weak correlations, particularly when using the simultaneous fit approach (Spearman $\rho \approx 0.15$). This is even more evident in the voxel-by-voxel fit, where even weaker correlations (Spearman $\rho < 0.15$) occur when using the sequential fit. The strongest correlations between IVIM and DSC were observed in pathological tissues, with a Spearman's ρ of around 0.2 in oedema when using the simultaneous fit.

Overall, diffusion metrics displayed strong correlations with the DKI-derived parameters, with the weakest correlation seen in WM-highFA using both sequential and simultaneous fit (sequential fit: diffusivity Spearman $\rho = 0.48 \pm 0.10$, kurtosis Spearman $\rho = 0.49 \pm 0.11$; simultaneous fit: diffusivity Spearman $\rho = 0.50 \pm 0.10$, kurtosis Spearman $\rho = 0.45 \pm 0.11$), and the strongest being oedema (diffusivity Spearman $\rho = 0.89 \pm 0.05$; kurtosis Spearman $\rho = 0.84 \pm 0.14$).

Table 4.3: *Average root mean squared error (RMSE) and corrected Akaike information criteria (AICc) for each tissue class at the cohort level. Both lower RMSE and lower AICc indicate comparatively better fitting*

	Mono Exponential		IVIM Bi-exponential		Kurtosis Expansion		IVIM + Kurtosis Expansion	
	RMSE (x10^{-3})	AICc	RMSE (x10^{-3})	AICc	RMSE (x10^{-3})	AICc	RMSE (x10^{-3})	AICc
GM	38.5 ± 5.9	-69.4 ± 3.6	7.7 ± 3.0	-104.4 ± 7.87	11.8 ± 3.0	-93.5 ± 5.6	2.1 ± 0.6	-120.3 ± 7.6
WM-lowFA	28.4 ± 3.3	-76.6 ± 2.7	8.9 ± 1.3	-99.7 ± 3.3	5.4 ± 2.6	-113.9 ± 10.1	1.4 ± 1.1	-133.4 ± 15.9
WM-highFA	27.8 ± 2.2	-77.0 ± 1.9	9.0 ± 0.8	-99.3 ± 2.0	4.2 ± 1.4	-118.7 ± 6.8	1.1 ± 0.3	-135.1 ± 8.22
Oedema	30.2 ± 6.4	-75.5 ± 5.2	9.9 ± 3.1	-98.0 ± 6.9	4.6 ± 1.7	-117.6 ± 12.5	1.6 ± 1.2	-129.2 ± 14.0
Tumour	26.6 ± 5.0	-78.5 ± 4.8	9.8 ± 1.3	-97.4 ± 3.4	3.7 ± 1.8	-123.2 ± 12.0	2.2 ± 0.9	-119.7 ± 10.4

Table 4.4.: *Mean ± standard deviations Spearman ρ correlation values.*

			f vs. CBV		
	GM	WM-lowFA	WM-highFA	Oedema	Tumour
Simultaneous fit	0.15 ± 0.06	0.13 ± 0.06	0.07 ± 0.05	0.21 ± 0.21	0.17 ± 0.09
Sequential fit	0.15 ± 0.06	0.09 ± 0.06	0.08 ± 0.05	0.11 ± 0.31	0.15 ± 0.10
Mean Simultaneous fit	0.12 ± 0.06	0.17 ± 0.08	0.11 ± 0.08	0.21 ± 0.18	0.18 ± 0.09
Mean Sequential fit	0.13 ± 0.07	0.14 ± 0.08	0.12 ± 0.06	0.15 ± 0.30	0.18 ± 0.12
			f.D* vs. CBF		
	GM	WM-lowFA	WM-highFA	Oedema	Tumour
Simultaneous fit	0.15 ± 0.05	0.10 ± 0.05	0.06 ± 0.03	0.12 ± 0.25	0.17 ± 0.12
Sequential fit	0.13 ± 0.04	0.09 ± 0.02	0.06 ± 0.05	0.12 ± 0.13	0.15 ± 0.08
Mean Simultaneous fit	0.16 ± 0.05	0.15 ± 0.06	0.10 ± 0.05	0.15 ± 0.26	0.22 ± 0.08
Mean Sequential fit	0.15 ± 0.06	0.14 ± 0.04	0.10 ± 0.06	0.14 ± 0.25	0.20 ± 0.13
			MD vs. D_{app}		
	GM	WM-lowFA	WM-highFA	Oedema	Tumour
Simultaneous fit	0.64 ± 0.10	0.50 ± 0.09	0.46 ± 0.06	0.83 ± 0.07	0.80 ± 0.09
Sequential fit	0.68 ± 0.09	0.54 ± 0.10	0.51 ± 0.08	0.84 ± 0.05	0.79 ± 0.09
Mean Simultaneous fit	0.68 ± 0.09	0.56 ± 0.13	0.52 ± 0.08	0.86 ± 0.05	0.80 ± 0.09
Mean Sequential fit	0.70 ± 0.08	0.61 ± 0.11	0.57 ± 0.08	0.86 ± 0.05	0.80 ± 0.09
			MK vs. K_{app}		
	GM	WM-lowFA	WM-highFA	Oedema	Tumour
Simultaneous fit	0.44 ± 0.12	0.53 ± 0.08	0.42 ± 0.11	0.68 ± 0.23	0.58 ± 0.15
Sequential fit	0.70 ± 0.09	0.64 ± 0.10	0.49 ± 0.14	0.83 ± 0.12	0.68 ± 0.20
Mean Simultaneous fit	0.52 ± 0.12	0.60 ± 0.09	0.49 ± 0.12	0.77 ± 0.19	0.61 ± 0.22
Mean Sequential fit	0.76 ± 0.07	0.70 ± 0.10	0.55 ± 0.13	0.85 ± 0.16	0.73 ± 0.18

4.3.3. Simulations

Simulation results are displayed in Figures 4.7-4.10, which depict the mean and standard deviation of the metrics *f*, D^*, D_{app}, and K_{app} respectively, at the different SNR levels.

Further analyses regarding the effects of sampling scheme, neighbourhood averaging and ROI-based averaging are included in Annex A. The CV and relative error for each metric at SNR levels 30 and 60 are summarised in Table 4.5.

The precision of the parameter estimation improved with increasing SNR for all metrics, as evidenced by the decrease in CV. Generally, the simultaneous fit yielded more precise results than sequential fit, except for K_{app}. Accuracy also improved with SNR, with K_{app} being the most accurately determined parameter.

The Wilcoxon signed-rank test revealed statistically significant differences in the means of the metrics estimated by both fitting routines across tissues and SNR levels, except for K_{app}.

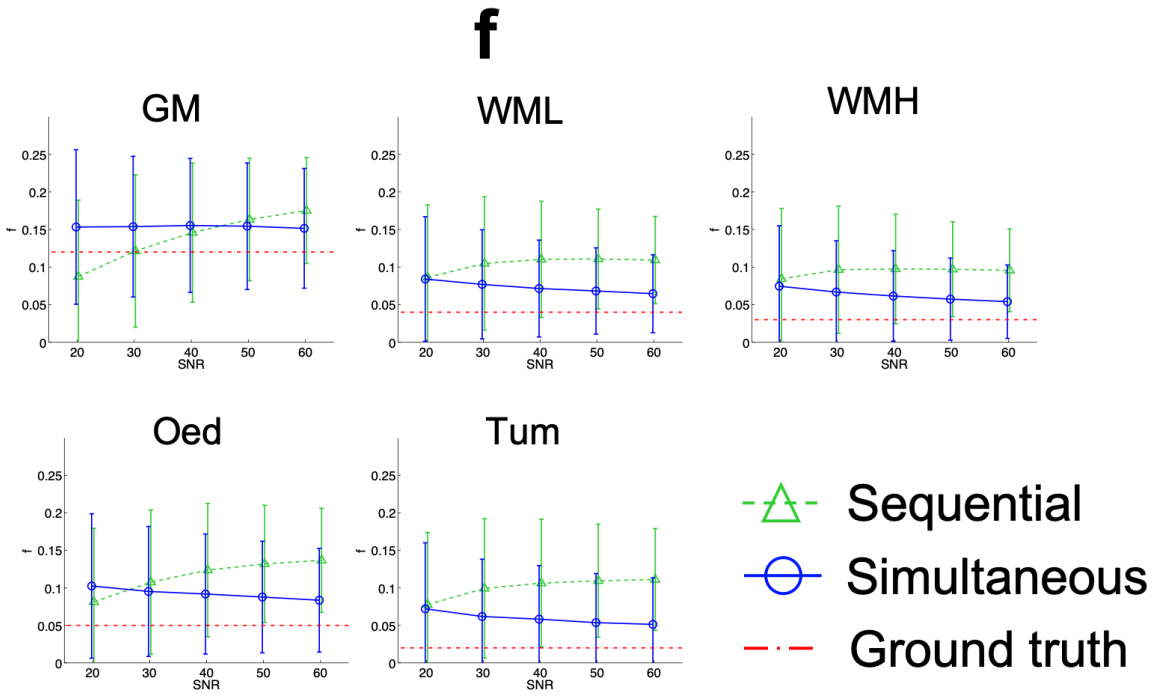

Figure 4.7.: *Plots of simulation results for* f. *The mean is represented by the geometric figures while th vertical bars represent the standard deviation at each SNR level.*

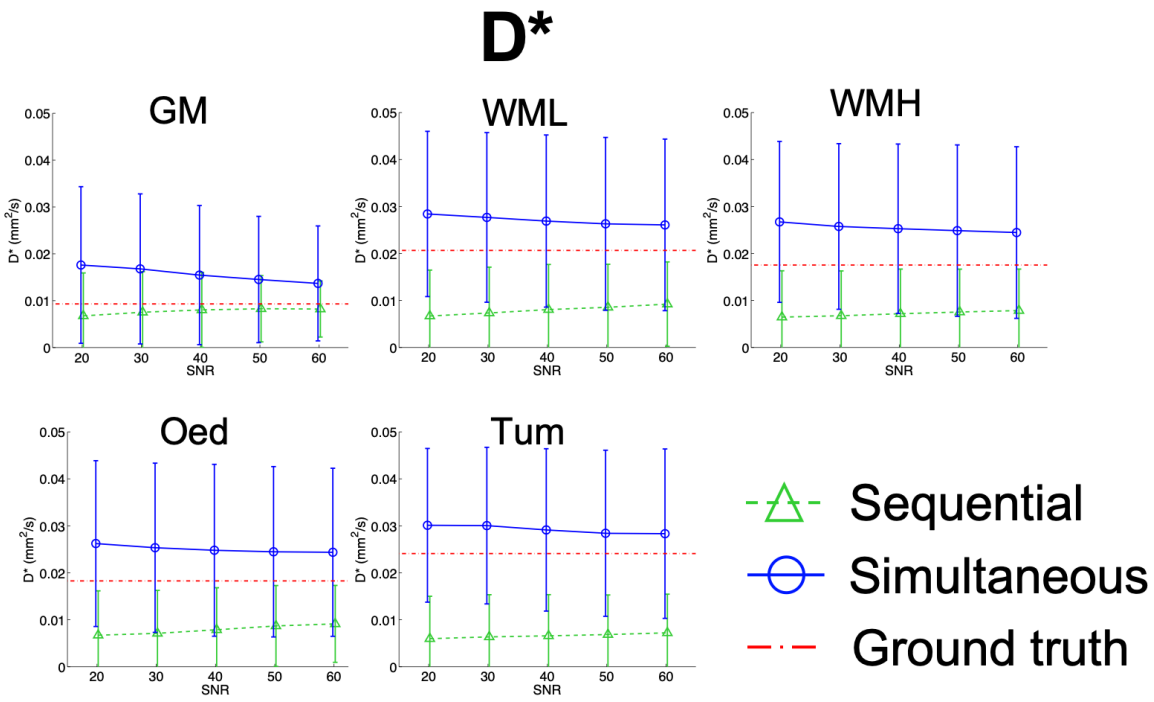

Figure 4.8.: *Plots of simulation results for* D^*. *The mean is represented by the geometric figures while th vertical bars represent the standard deviation at each SNR level.*

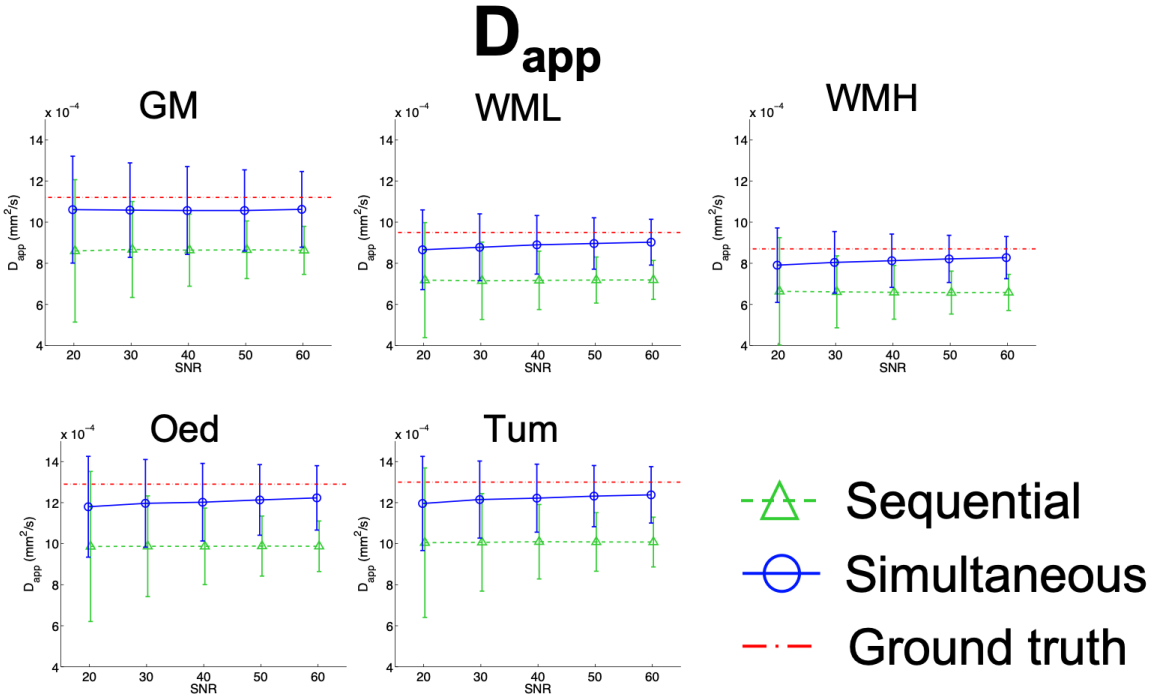

Figure 4.9.: *Plots of simulation results for D_{app}. The mean is represented by the geometric figures while th vertical bars represent the standard deviation at each SNR level.*

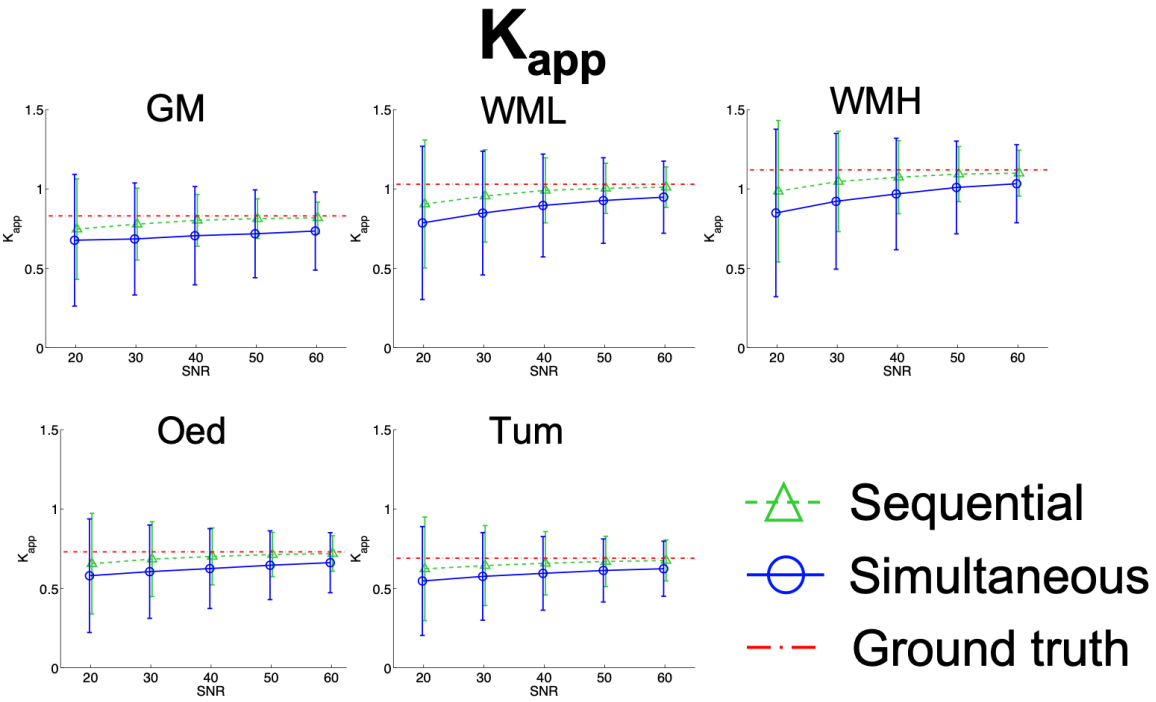

Figure 4.10.: *Plots of simulation results for K_{app}. The mean is represented by the geometric figures while th vertical bars represent the standard deviation at each SNR level.*

Table 4.5.: *Coefficients of variation and relative errors of the IVIM/NG-diff simulations at SNR levels 30 and 60*

Coefficient of Variation (%)

			f	D*	D_{app}	K_{app}
SNR = 30	Simultaneous fit	GM	62.0	95.3	21.8	50.8
		WM-lowFA	93.9	67.2	18.7	46.3
		WM-highFA	103	68.5	19.0	47.8
		Oedema	91.5	71.2	18.0	49.4
		Tumour	122	56.7	15.5	49.5
	Sequential fit	GM	85.0	117	27.2	28.8
		WM-lowFA	83.2	133	26.1	29.7
		WM-highFA	88.1	141	27.0	30.7
		Oedema	89.8	127	25.0	37.9
		Tumour	95.9	142	24.3	40.8
			f	D*	D_{app}	K_{app}
SNR = 60	Simultaneous fit	GM	52.2	89.8	17.4	33.6
		WM-lowFA	80.3	70.1	12.4	23.9
		WM-highFA	90.8	73.9	12.2	23.0
		Oedema	82.6	74.2	12.8	28.3
		Tumour	119	63.3	10.7	27.0
	Sequential fit	GM	39.9	73.0	13.5	12.3
		WM-lowFA	52.8	96.4	13.1	12.7
		WM-highFA	57.4	111	13.3	12.7
		Oedema	49.8	88.5	12.2	15.7
		Tumour	60.7	111	11.9	19.0

Relative error (%)

			f	D*	D_{app}	K_{app}
SNR = 30	Simultaneous fit	GM	27.4	81.8	5.33	16.9
		WM-lowFA	95.8	30.1	7.82	17.6
		WM-highFA	127	46.4	7.79	18.8
		Oedema	91.9	38.6	7.43	17.6
		Tumour	213	23.2	6.86	18.0
	Sequential fit	GM	0.170	19.3	23.1	6.02
		WM-lowFA	165	64.7	24.8	6.57
		WM-highFA	225	62.0	24.5	7.16
		Oedema	116	60.1	23.8	6.56
		Tumour	387	73.9	22.2	7.93
			f	D*	D_{app}	K_{app}
SNR = 60	Simultaneous fit	GM	27.3	45.7	5.36	11.6
		WM-lowFA	62.2	26.0	5.00	7.84
		WM-highFA	78.0	41.3	4.68	7.21
		Oedema	67.5	32.6	5.25	9.41
		Tumour	151	17.8	4.70	9.23
	Sequential fit	GM	45.3	11.6	22.9	1.42
		WM-lowFA	175	55.6	24.3	1.67
		WM-highFA	220	54.9	24.4	1.48
		Oedema	174	50.9	23.5	1.50
		Tumour	450	70.5	22.4	2.07

4.4. Discussion

This study introduces a clinically feasible protocol for the simultaneous acquisition of IVIM and non-Gaussian diffusion parameters. The protocol is based on the acquisition of trace-based diffusion data across a wide range of b-values in a manner intended to compensate for SNR loss at increasing b-values.

The option to export the diffusion-weighted images as “trace”, opposed to the three images with orthogonal diffusion-weighting directions originally acquired by the scanner, reflects a standard practice in clinical environments, where images are acquired with a b-value of 1,000 s/mm^2. The proposed protocol includes this widely used information, making it compatible with retrospective patient evaluations if integrated into oncological routine.

It is important to note that the exported "trace" images do not, strictly speaking, correspond to the more commonly known trace of DTI. Exceptions being in regions where fibres happen to be aligned with one of the orthogonal directions, or for voxels with macroscopic isotropic diffusion - generally used for IVIM (Le Bihan et al., 1988). By adopting the DTI formalism to obtain a more robust estimation of the trace, more directions are needed (six, instead of three from the proposed protocol). Thus doubling the measurement time and still being insufficient to determine the kurtosis tensor. In fact, even six directions have been shown to provide an improper characterization of even the diffusion tensor (Jones, 2004). In this work, an extensive sampling of the diffusion-weighting domain was preferred to the number of diffusion directions, exactly to cover a wider range of diffusivities.

The typical diffusion kurtosis protocol contains 30 directions and two non-zero b-values, rendering it often prohibitively long in a clinical context. By incorporating the kurtosis expansion to the "trace"-based fit would allow the adoption of kurtosis metrics in the competitive clinical environment. A good agreement between D_{app} and K_{app} derived from the proposed protocol, and MD and MK derived from the standard DKI was demonstrated here (Fig. 4.5), particularly in tumour and oedema regions. The proposed acquisition seems, therefore, sufficient for the characterisation of diffusion in brain tumours, even if spherical invariance is not preserved.

While the proposed protocol has a shorter acquisition time than the combined acquisitions for DKI and DSC, this is not not considered to be the main advantage, as other, faster DKI protocols have also been proposed (Hansen et al., 2013, 2016). Instead, the proposed protocol provides a wider characterisation of tumour properties relevant for diagnosis in a short amount of time. Other fast diffusion protocols have been successfully applied to brain tumours (Nael et al., 2017; Hu et al., 2011; Li et al., 2020), with the caveat that MD and MK alone are estimated. With interest in multi-parametric characterisation of pathological tissue growing (Jacobs et al., 2001; Wu et al., 2001; Livne et al., 2017; Hansen et al., 2013, 2016; Tietze et al., 2015), the proposed protocol strives in the acquisition of multi-parametric, clinically relevant information in a short amount of time. Compared to those in Nael et al. (2017) and Hu et al. (2011), the proposed protocol has the advantage of providing IVIM metrics, with a slight increase in acquisition time. Multi-parametric tissue characterisation can be explored simultaneously using the method shown in Fig. 4.6, with the radial plot leveraging the information of multiple parameters to potentially reveal pathological signatures.

4.4.1. Design of acquision and denoising

Diffusion metrics like D_{app} and K_{app} are known to be directionally dependent (Nael et al., 2017). However, in tumour tissue, where FA has been shown to be significantly reduced (White et al., 2011), the influence of directional dependency decreases. This allows for the replacement of a multi-directional shell-based acquisition with a faster, "trace"-based one, particularly when the primary objective is to characterise tumour properties.

Diffusion data in clinical scanners tend to have long TE and be inherently noisy, especially at high b-values due to its inherent decay. Therefore, noise reduction is a crucial step when trying to estimate diffusion properties spanning multiple regimes. In this study, denoising was performed using PCA on the entire dataset and then identifying and removing components classified as noise. The effectiveness of denoising is defined as $\sqrt{n_c/r}$ (n_c = number of contrasts, r = rank of approximation). This evidences that the noise suppression is proportional to the redundancy of the acquired contrasts, which decreases when the

directionality aspect is included, as the complicated fibre structure of white matter leads to different signals with different diffusion directions. Since the proposed protocol acquires a small amount of directions, its redundancy is derived from the extensive sampling of the b-value range covered, translating in a higher quality and stability of the parameter estimates, as shown in Fig. 4.3.

From the standpoint of acquisition design, denoising properties, and simplicity of fitting, the acquisition of a "trace"-based protocol with an extensive range and number of b-values appears beneficial, even if spherical invariance is not guaranteed. Overall, the results suggest that denoising performance should be critically assessed when designing and optimising a diffusion-based protocol.

4.4.2. Simulations

The levels of SNR used in the simulations were determined to cover values typically seen in *in vivo* acquisitions. For comparison, the mean ± standard deviation SNR of the non-diffusion-weighted images acquired in this study was 51 ± 8 for the proposed protocol and 60 ± 6 for the DKI protocol, ranging from 35 to 69.

Regarding the simulation results, for low SNR levels, the IVIM parameters obtained from both fits differ to some extent, with the sequential fit having an overall lower accuracy. The exception to this is in the case of GM, as evidenced in Figures 4.7 and 4.8.

As SNR increases, the sequential fit increasingly overestimates f while that from the simultaneous fit increases in accuracy, moving towards the ground truth. In contrast, as evidenced by Fig. 4.8, the estimation accuracy of D^* increases with SNR, regardless of fitting approach. In either case, reproducibility of the IVIM metrics is generally low, demonstrated by the high CV, summarised in Table 4.5, and agreeing with reported literature (Meeus et al., 2016; Wu et al., 2015).

The highest reproducibility was seen in the D_{app} estimated by either approach, remaining constant with increasing SNR levels in the simultaneous fit ($CV_{D_{app}@SNR30_{SimFit}} = 22\%$, $CV_{D_{app}@SNR30_{SeqFit}} = 27\%$). When it comes to accuracy, a systematic bias was seen in D_{app} when estimated using the sequential fit (Fig. 4.9), which was reproduced by the *in vivo*

results (Fig. 4.5). On the other hand, this bias was not seen when fitting the data with the simultaneous approach, as D_{app} approaches the ground truth with an increase in SNR.

The K_{app} was overall the most accurately estimated parameter, but its reproducibility was still lower than that of D_{app} at smaller SNRs. The simultaneous fit of K_{app} showed broader distributions compared to those of the sequential fit across all SNR levels ($CV_{K_{app}@SNR30_{SimFit}}$ = 51%, $CV_{K_{app}@SNR30_{SeqFit}}$ = 29%), which hat a narrower and less biased distribution (Rel. $Err._{K_{app}@SNR30_{SimFit}}$ = 17%, Rel. $Err._{K_{app}@SNR30_{SeqFit}}$ = 6%). In fact, both fitting approaches showed an underestimation at lower SNR levels, which is then minimized at higher SNR, as shown in Figures 4.9 and 4.10. Of important note, even for an SNR of 1000, the bias seen in the sequential fitting of *f*, D^* , and D_{app} was still present (results not shown).

The persistent bias highlights the limitations of the sequential approach. The sampling scheme used here did not incorporate extra low b-value information ($b < 100$ s/mm^2). A finer b-value sampling resolution would have proven of value for the estimation of the IVIM metrics. However, due to limitations imposed by the scanner software, increments in b-values smaller than 50 s/mm^{2}are not allowed, precluding a finer sampling rate in this range.

In line with the moulds described in 4.2, additional simulations were performed using a dense sampling scheme with 20 b-values in the IVIM-relevant interval in order to emulate an optimised experimental setup (see Annex A). These revealed that a denser sampling scheme at clinical SNR yields similar results in terms of precision and accuracy to those from a sparser sample at a higher SNR. Increasing SNR is often done by averaging data: either by repeating the acquisition, thus increasing the measurement time; or by averaging the signal of neighbouring voxels. Simulations showed that a number of 8 averages leads to very similar results as the simulated dense sampling scheme in terms of accuracy and precision (see Figs. A.5 and A.8 of Annex A). It is therefore expected that the neighbourhood-based fit approximately compensates for the lack of the b-values in the IVIM regime in homogeneous regions over the 3x3 voxel neighbourhood. The simulations show that the precision and accuracy of the neighbourhood-based fit of IVIM parameters is modest but it becomes increasingly better when SNR is increased by averaging over several hundreds or

even thousands of voxels, mirroring the ROI-based approach. For reference, the tumours observed in this study had volumes ranging from 108 to 10,611 voxels. The simulations suggest that averaging data from a homogeneous region of 1,000 voxels, the CV for f is around 10%, with negligible bias, while D^* still retains a relatively high CV of 30% and overestimation of 8-10%. Reliable estimates of the IVIM parameters are obtained for averages over 10,000 voxels (an equivalent SNR of 1,500-2,000). Apart from the small number of b-values sampled in the IVIM range, the low IVIM fraction also plays a role, being around of 10% or less in the brain. In an organ with much higher perfusion fraction, for example 30% (as seen for example in the kidney), the simulations show that precision and accuracy would improve by roughly a factor 3 with the same sampling scheme and SNR.

In summary, the simulations showed that the simultaneous fitting approach is, overall, more accurate and reproducible in the estimation of diffusion parameters in the presence of noise. The results also suggest that while D_{app} and K_{app} are relatively robust metrics, careful consideration must be given to the sampling scheme and noise reduction techniques to optimise the performance of the IVIM/NG-diff protocol, especially in the IVIM regime.

4.4.3. *In vivo* acquisitions

The *in vivo* performance of the proposed protocol was evaluated by comparing its derived parameters to their canonical counterparts. These comparisons were performed at multiple levels, including voxel-wise, neighbourhood level, and tissue class level, assessing the validity and reliability of the protocol in different conditions.

Considering implementation in the clinical workflow, the simultaneous fit is much slower to compute (almost seven fold increase) than the sequential fit. Fitting the signal in the sequential manner is computationally efficient, an important factor in providing the estimated parameters directly at the scanner's console. The disadvantage here, however, is the added sensitivity to noise. Conversely, simultaneous fitting is more stable to noise, by virtue of the algorithm used, at the cost of increased computational time. Noise influences were especially apparent for the voxel-based fits of the IVIM parameters (see Fig. 4.5). While

the neighbourhood-based fit decreased the spatial variability of the parameters, the IVIM maps, D^*in particular, still lacked the anatomical consistency seen in their counterparts derived from DSC. This suggests that while the protocol is effective, further refinements may be necessary to improve reliability of these metrics.

At the tissue class level, the combined IVIM/NG-diffusion model provided the best fit for the data, outperforming the simpler models (lowest RMSE and AICc shown in Table 4.3). This shows that the combined IVIM/NG-diff is the best model to capture the complex diffusion behaviour of brain tumours amongst the models considered.

As for the IVIM *in vivo* parameters, the sequential fitting results for normal-appearing tissue showed higher values than those found in the literature, while those for tumour tissue were within the expected range (Federau et al., 2012, 2014b; Bisdas et al., 2013) (f_{WM} = 0.03-0.09, f_{Tum} = 0.08-0.15). Conversely, the simultaneous fit yielded IVIM values in accordance with those reported in the literature for in healthy tissue but are lower than expected in tumour tissue. This highlights the importance of considering the fitting routine depending on clinical context and specific tissue being analysed.

The correlation between IVIM and DSC metrics was generally weak, as seen in Table 4.4, especially at the voxel level. This result suggests that, despite IVIM providing valuable insight to the microstructural environment, it might not be a direct substitute for DSC in this context. In fact, there is supporting evidence that IVIM and DSC metrics in the brain might not be as interchangeable, with some studies reporting good correlations between the techniques and others showing poor to negative correlations (see (Federau, 2017) for review). This can be a result of many confounding factors. One of these factors might be that IVIM and DSC are sensitive to different kinds of flow and, therefore, be suitable to characterise different microstructural features (Federau, 2017). Generally, IVIM probes blood micro-circulation but other types of intravoxel incoherent motion are also present (Le Bihan et al., 1988; Le Bihan and Turner, 1992), as the flow in larger vessels can also lead to incoherent intravoxel dephasing. Additionally, DSC is not equally sensitive to all vessel sizes, emphasizing large vessels (see Caldeira et al. (2019) and Leu et al. (2016) for review). Quantification of DSC metrics is further influenced by extravasation of contrast

agent, in which case, the CBV tends to be underestimated if T_1-weighting effects dominate due to increased permeability of tumour vessels, or overestimated if T_2^*-weighted effects dominate (Caldeira et al., 2019; Leu et al., 2016).

Regardless, the IVIM maps obtained from the *in vivo* data align with the fact that capillary density is higher in GM than in WM (Craigie, 1945), as higher f values were seen in GM than in WM and all the other tissues. Irrespective of the fitting method, the IVIM quantities share a trend with those from their DSC counterparts across the tissue classes, i.e. they exhibit higher values in GM, and lower in oedema.

In oedema, a redistribution of water takes place, leading to excess accumulation in the extracellular space (Stokum et al., 2015). This is reflected in the increase in D_{app} and decrease in f (Table 4.1). Due to the high heterogeneity in vascularisation and perfusion in the tumour micro-environment (Jain et al., 2007), IVIM parameters are expected to vary with respect to tumour type, stage, and region, making them potentially useful in tumour grading. Indeed, there are already studies supporting the notion that these parameters are relevant in characterising brain tumours (Puig et al., 2016; Federau et al., 2014a; Iima et al., 2014) and even breast lesions (Iima et al., 2015). The relatively high standard deviation seen in this study in both f and $f.D^*$ in the tumour tissue class across patients seems to support that idea. Investigating the potential of the IVIM parameters in grading would be very useful in this respect but was precluded here by the size and heterogeneity of the cohort.

While D_{app} and K_{app} showed strong correlations with their counterparts from the kurtosis tensor (Table 4.4), they showed a systematic bias compared to the DKI-derived parameters (Fig. 4.5). This could be a consequence of the modelling approaches. On the one hand, explicit correction of the IVIM fraction present in S_0 is performed in the proposed method (Eq. 4.12), which goes uncorrected in either the DTI or the DKI formalisms. This results in a faster signal decay having to be modelled by DTI/DKI, yielding higher MD and/or MK values. On the other hand, the inclusion of the kurtosis expansion was also shown to lead to differences in MD and FA obtained from conventional DTI and DKI (Lanzafame et al., 2016). In this study, MD is derived by means of DKI modelling, using data up to

a b-value of 2,000 s/mm^2, the same range used by the simultaneous fit of the proposed protocol. Conversely, D_{app} estimated from the sequential fit is more similar to a DTI fit, in that it only uses data up to b = 1,000 s/mm^2. These differences are evidenced in Fig. 4.5, where the histograms of the D_{app}/MD ratio show an underestimation of D_{app} for all tissue classes when the fit is performed with the sequential method (similar to DTI), which gets reduced when the fit is performed with the simultaneous method (similar to DKI).

As hinted towards in 2, the measured diffusion signal depends not only on b-value but also on TE, with acquisitions performed at longer TE values yielding overestimated MD (Chou et al., 2012). Since the TE used in each protocol was different ($TE_{IVIM/NG\text{-}diff}$ = 92 ms vs TE_{DKI} = 115 ms), it could have also contributed to the discrepancies seen between D_{app} and MD, and K_{app} and MK. The effect of TE also extends to the IVIM parameters: it has been previously shown in the prostate that both f and D^* significantly increase with an increase in TE (Feng et al., 2018), due to the fact that the bi-exponential model of IVIM does not account for the different T_2 values from blood and tissue water.

4.4.4. Limitations

While the proposed protocol shows promise in the multi-parametric characterisation of tissues, there are several limitations that need to be addressed.

The results of the simulations suggest a shortcoming either in the fitting or in the sampling of the data, as evidenced by the observed bias in the IVIM parameters. Of particular importance is the sequential fit, where the determination of D_{app} using the slope of the logarithm is heavily dependent on which b-values are chosen (Ogura et al., 2011), as well as the level of noise in the signal. In this study, a slope between b_1 = 500 s/mm^2 and b_2 = 1,000 s/mm^{2}was used, offering the largest range for signal attenuation within a range with negligible effects of both IVIM and kurtosis.

The b-value sampling scheme in the proposed protocol has fewer points in the IVIM regime than those often seen in the literature (Federau et al., 2012, 2014b; Bisdas et al., 2013). Since the protocol was developed having in mind an easy integration in the clinic with minimal changes to product sequences, the sampling scheme was chosen considering

manufacturer settings: $b_{min} = 0$ s/mm^2, $\Delta b_{min} = 50$ s/mm^2. These restrictions result in too few data points with which to perform a proper fit of the IVIM parameters, especially D^*, at clinical SNR levels.

Effects of partial-volume could have been considered in this study. Larger voxels, as is the case with the ones in the proposed protocol, can lead to multiple tissue classes within the same voxel, resulting in biases in the estimation of diffusion parameters for each class (Alexander et al., 2001). Additional simulations including mixed tissue classes or the more careful analysis of voxels with tissue probabilities below the used threshold could have helped determine to which degree the proposed protocol and processing routines are affected by this effect.

State-of-the-art pre-processing routines like *topup* and *eddy* cannot be run on the proposed protocol due to the lack of required images with different phase-encoding directions and different diffusion directions, respectively. Instead, motion and eddy current correction had to be performed with *eddy_correct*, a tool lacking important features like susceptibility-induced distortions, signal pile-up, and slice dropout correction, making the combination *topup* / *eddy* superior (Graham et al., 2016). Future changes would include the acquisition of a b = 0 s/mm^2 image with opposing phase encoding direction, conforming to *topup*, and exporting directional data from the proposed protocol individually, allowing *eddy* to be used.

Finally, since the number of diffusion-encoding directions was small, the proposed protocol provides with metrics which are not rotationally invariant. Despite the considerations given to the design of the protocol, sub-optimal sampling of the micro-architecture is performed, which could lead to biases in the results (Jones, 2004).

5. Analysis of Diffusion MRI Using NNLS

5.1. Motivation

The work of the previous chapter focused on capturing diffusivity phenomena at low and moderately high b-values (up to 2,000 s/mm^2). However, characterising the tissue's microstructure benefits from very high b-values, reflecting the movement of very slow diffusing molecules. Therefore, extending the b-value range even further can provide with additional insight to tissue microstructure.

As mentioned previously, characterisation of diffusivity in the tissues in the clinic is typically performed using the ADC. This assumes that the obtained signal decays mono-exponentially with b-value. However, the b-value range of the ADC is relatively short (valid until maximum b = 1,500 s/mm^2) and it fails to properly capture highly complex and heterogeneous tissues like brain tumours, where, within the same voxel, multiple pools of diffusing water molecules contribute to the observed signal. To compensate for this, bi-exponential or tri-exponential decays can be applied, assuming that these complex media are described by two or three diffusing water pools, respectively (Mulkern et al., 1999; Zeng et al., 2018).

Alternatively, data-driven methods, including non-negative least squares (NNLS), make no assumption regarding the amount of diffusing water pools. Instead, for each voxel, a spectrum of diffusivities is estimated, where the amplitude of the spectrum at a given diffusivity indicates the relative contribution of that particular water pool to the observed signal (Kroeker and Henkelman, 1986). Application of NNLS to *in vivo* dMRI data in humans has already been successfully demonstrated in the brain (Keil et al., 2017; De Luca et al., 2018).

Recently, in the context of malignant brain tumour, lesions of restricted diffusion, i.e. hyperintense in high b-value images and with low ADC values, have been shown to develop alongside a myriad of processes during tumour management. These include treatment response (Bähr et al., 2014; Mong et al., 2012; Rieger et al., 2010), pseudo-progression (Yamasaki et al., 2012; Kothari et al., 2013), tumour progression (Gerstner et al., 2010; Gupta et al., 2011), and atypical necrosis accompanied by viable tumour (Farid et al., 2013; LaViolette et al., 2014; Nguyen et al., 2016; Zhang et al., 2016; Goyal et al., 2018). Each of these is accompanied with increasingly poorer prognosis. Therefore, properly identifying the type of underlying process leading to these lesions can be of critical importance to brain tumour management.

In this work, the use of NNLS is demonstrated in the fit of dMRI data in a broad brain tumour cohort. Additionally, restricted diffusion lesions are quantitatively assessed under the guise of dMRI and PET in a subset of patients, in an effort to provide a better characterisation of the type of processes that gave rise to these lesions. It is hypothesised that the use of NNLS might lead to a better characterisation of the diffusion signal in the tissues, in particular in those where the microstructure is not well understood and so the use of fixed component models might be inappropriate.

5.2. Methods

5.2.1. NNLS simulations

Within the NNLS formalism, the acquired signal is assumed to be a sum of exponentially decaying terms, each with its own diffusivity. Fitting of noisy data using NNLS is an ill-posed problem and it is known to produce spurious and sparse spectra. To address this, NNLS solutions are typically regularised, imposing smoothness along the solution space. The most common type of regularisation is Tikhonov regularisation (Tikhonov and Arsenin, 1977), making the NNLS problem take the form

$$\begin{aligned} \min_{x,\lambda} \quad & ||Ax - y||^2 + \lambda||x||^2 \\ s.t. \quad & x \geq 0, \quad \lambda > 0 \end{aligned} \tag{5.1}$$

with A being the forward operator and λ the regularisation parameter. Note that if $\lambda = 0$ the problem turns into a non-regularised NNLS one. For λ values greater than 0, spurious solutions are penalised in favour of smoother ones.

Throughout this work, A has the form

$$A = e^{-bD} \tag{5.2}$$

with D being a range of diffusivities, ranging from 10^{-6} to 10 mm^2/s in 250 logarithmically spaced steps.

Simulations were performed to determine the effects of signal-to-noise ratio (SNR), diffusivity pool fraction, and λ on the NNLS results. The base signal was given as the following exponential composition

$$S(b) = \underbrace{f_{fast}e^{-0.01758\times b}}_{Fast\ component} + \underbrace{f_{water}e^{-0.003\times b}}_{Free\ water\ component} + \underbrace{f_{slow}e^{-0.00087\times b}}_{Slow\ component} + \underbrace{f_{vslow}e^{-0.0001\times b}}_{Very\ slow\ component} \tag{5.3}$$

such that

$$f_{fast} + f_{water} + f_{slow} + f_{vslow} = 1 \tag{5.4}$$

This model features a fast component, with an IVIM-like diffusivity value; a free water component; a slow, restricted diffusion component, as seen typically in WM; and a very slow, highly restricted diffusion component, simulating the restricted diffusion lesion micro-environment. Diffusion fractions were varied such that one of the fractions was set as predominant, with a value of $1 - f_1 - f_2 - f_3$, where f_1, f_2, and f_3 are the fractions of the remaining components. The other three fractions were varied from 0 to 0.2 in intervals of 0.10, satisfying Eq. 5.4. The values of the fast and slow diffusivity pools are inspired by

D^* and D_{app} obtained for WM with high FA of the ROI fits shown in the previous chapter (Table 4.1).

For each combination of diffusion fractions, noise was added to the decay curve simulating SNR levels of 20, 60, and 200, as described in 4.4.2. Each SNR/fraction combination was simulated 1,000 times with independently sampled noise and was fitted using regularised NNLS. To test the influence of the regularisation parameter, 20 λ values were tested per SNR/fraction combination, ranging from 10^{-3} to 1.4 in logarithmically spaced steps.

5.2.2. Patient cohort and imaging

From February 2016 to July 2019, patients that were referred to the Institute of Neuroscience and Medicine of the Research Centre Jülich from the hospitals in the region for diagnostic imaging purposes were randomly selected to undergo the dMRI protocol described below. Ethical approval was obtained from the individual hospitals, in accordance to the requirements of the local ethics committees, and prior written and informed consent was given by the patients. The patients underwent simultaneous PET-MR acquisitions, performed on a hybrid Siemens (Erlangen, Germany) scanner based on a 3T Tim-TRIO MR system with a BrainPET insert (Herzog et al., 2011).

FET was synthesised and administered to the patients according to the description in the previous chapter (see 4.2.1), followed by a 50-minute PET acquisition.

Concurrently to the PET acquisition, standard clinical MRI protocols were acquired, including high-resolution volumetric T_1-weighted, high-resolution volumetric T_2-weighted, and FLAIR images. At the discretion of the supervising physician, gadolinium-based contrast agent was administered and a second T_1-weighted image was acquired (T_1C).

Following these, research protocols were acquired until the 50 minutes dictated by PET were finished. Among the research protocols were two dMRI acquisitions covering two ranges of b-values: one low and one high. The low b-value range acquisition included 16 b-values: 0, 50, 100, 200, 300, 500, 700, 1000, 1200, 1500, 1800, 2000, 2200, 2500, 2700, and 3000 s/mm^2 with TE of 92 ms; the high b-value range included 13 b-values: 0, 1000, 1500, 2000, 2500, 3000, 4000, 5000, 6000, 7000, 8000, 9000, 10000 s/mm^2 at TE of 134 ms. Each

b-value was acquired along three orthogonal diffusion encoding directions (b-vector). Shared imaging parameters included: TR = 5000 ms, voxel size 2x2x2 mm^3, FOV = 220x156 mm^2, 24 slices with a 1.4 mm slice gap, partial Fourier of 5/8 and IPAT factor of 2. An additional non-diffusion-weighted image was acquired per b-value range with opposing phase encoding direction to correct for susceptibility artefacts. Acquisition time for the low b-value range was 4 mins 19 secs and for the high b-value range 3 mins 30 secs.

5.2.3. Image processing

The dMRI images were processed using TORTOISE (Pierpaoli et al., 2010; Irfanoglu et al., 2017). First, they were denoised using a PCA-based algorithm (Oros-Peusquens and Shah, 2013; Veraart et al., 2016a,b), then corrected for eddy-current artefacts and subject motion as part of the DIFFPREP routine. Afterwards, susceptibility distortions were corrected with DRBUDDI (Irfanoglu et al., 2015).

Due to the acquisition of images with the same b-values and different TEs, effects of T_2 relaxation seen between the low and high b-value scans can be removed based on the images with shared b-values - see Annex B for further details.

Then, the scans were merged into a single dataset and the diffusion trace signal was computed following

$$S(b) = \sqrt[3]{\prod_{i=1}^{3} S_{b_i}} \tag{5.5}$$

where $S(b)$ is the trace signal at b-value b and S_{b_i} is the acquired diffusion signal with b-vector i and b-value b. These steps were performed in MATLAB (R2018b, Mathworks, Nattick, MA, USA) using custom scripts.

Linear transformations between the PET and T_1, and T_1 and dMRI images were calculated using ANTs (Tustison et al., 2015). All computations were performed on an Ubuntu 20.04 with an AMD Ryzen7 3800X, an NVIDIA RTX 3070 and 32 GB of RAM.

5.2.4. Diffusion data fitting

Mono, bi-, and tri-exponential

A fit to mono-, bi-, and tri-exponential decays was performed to identify the value of the additional exponential terms and to be able to compare them to NNLS fitting. The merged data were averaged by tissue class, as described below in 5.2.5, and fitted to the following models:

$$S(b)/S(0) = e^{-bD} \tag{5.6}$$

,

$$S(b)/S(0) = f_{slow}e^{-bD_{slow}} + (1 - f_{slow})e^{-bD_{fast}} \tag{5.7}$$

, and

$$S(b)/S(0) = f_{vslow}e^{-bD_{vslow}} + f_{slow}e^{-bD_{slow}} + f_{fast}e^{-bD_{fast}} \tag{5.8}$$

subject to

$$f_{vslow} + f_{slow} + f_{fast} = 1 \tag{5.9}$$

NNLS

The merged data were also fit via NNLS with zero order Tikhonov regularisation (Mackay et al., 1994) to the following equation:

$$S(b) = \sum_{n=1}^{N} f(D_n)e^{-bD_n} \tag{5.10}$$

were $f(D_n)$ is the fraction of the diffusing water pool given by diffusivity D_n. This fit was performed using the NNLS implementation available from *lsqnonneg* in MATLAB.

The resulting spectra were then normalised to their sum and divided into six compartments based on the diffusivity values: D = [0.055, 0.25]x10^{-3} mm^2/s, D = [0.3, 0.5]x10^{-3} mm^2/s, D = [0.55, 1]x10^{-3} mm^2/s, D = [1.20, 2.30]x10^{-3} mm^2/s, D = [2.5, 4]x10^{-3} mm^2/s, and D = [9, 80]x10^{-3} mm^2/s.

5.2.5. Tissue classes

The brain images were segmented into six ROI: normal appearing grey matter (GM), normal appearing white matter (WM), cerebrospinal fluid (CSF), FLAIR-based oedema, FET-PET hotspot, and dMRI hyperintense lesion.

The normal appearing masks, i.e. GM, WM, and CSF, were estimated using a two-step approach. First, the T_1-weighted data of the whole brain was fed into *united segmentation* provided by SPM12 (Ashburner and Friston, 2005). Secondly, a hemispheric mask corresponding to the healthy hemisphere was applied on the *united segmentation* results to determine the normal appearing masks.

The oedema ROI was defined manually on representative slices of the FLAIR acquisition, based on the hyperintense signal in these images. The ROI was drawn across multiple FLAIR slices to account for the different resolutions between FLAIR and the dMRI acquisitions. Since FLAIR hyperintensities can represent oedema, infiltrative tissue, or even active tumour - as mentioned in 3.1.1 -, the hand-drawn ROI was subject to an exclusion of the voxels identified by the FET-PET hotspot and dMRI hyperintense lesion masks (described below), thus increasing the specificity of the FLAIR-based ROI to oedema.

The FET-PET hotspot was defined by summing the last four frames of the PET dynamic acquisition and applying a threshold of 1.6x the average contralateral WM intensity, as described in Pauleit et al. (2005).

Finally, the dMRI hyperintense lesions were segmented in the following semi-automatic procedure. Firstly, the images from the original acquisition ranging from b-values = 6,000 to 10,000 s/mm^2 were summed along each b-vector. Then, k-means clustering with 3 clusters was performed on the brain voxels of each of the summed images. This number of clusters was chosen under the assumption that one can group the voxel intensities of brain tissue at the considered b-values in 3 classes: 1) voxels with no diffusion signal (GM and CSF); 2) voxels which still show some signal (portions of the WM); and 3) voxels with pronounced signal intensity (dMRI hyperintense lesions). In some cases, WM structures exhibit signal intensities which would lead to them be grouped with the dMRI hyperintensie lesions. Conversely to WM, however, dMRI hyperintensities display isotropic diffusion at the

macroscopic level, i.e. they are present in all three b-vectors. Therefore, the superposition of the third cluster of all three k-means resulted in the initial dMRI hyperintensity mask, free of WM structures. Finally, the dMRI hyperintense lesions were segmented using a region growing algorithm seeded on the highest intensity voxel. Manual intervention was only required in the case that multiple disconnected clusters of dMRI hyperintense lesions were present, in which case, the isolation of the different clusters was performed via region growing with manually placed seeds and the final mask was the conjunction of the isolated masks.

All ROI were then co-registered to the dMRI and PET spaces via the previously calculated transformations.

5.2.6. Statistical analyses

First, the AICc for the mono-, bi-, and tri-exponential fits were calculated, as described in 4.2.6.

The summed NNLS spectral amplitudes for each compartment were compared across tissues using Kruskal-Wallis test.

Patients presenting with dMRI hyperintense lesions were sorted into 3 groups, based on the PET dynamic curves of the dMRI hyperintense lesion: 1) lesion with increased FET uptake, 2) lesion with physiological FET uptake, 3) lesion with less than physiological FET uptake. Additionally, patients with histological information were grouped based on tumour entity, according to the WHO 2016 classification (Louis et al., 2016). Group differences in each compartment were assessed via Kruskal-Wallis test.

Multiple comparisons were corrected via Bonferroni adjustment.

5.3. Results

5.3.1. Patient cohort, DWI lesion prevalence, and histology

During the aforementioned period, 60 imaging sessions from 53 patients were randomly assigned to include the relevant dMRI protocols. From these, nine sessions were excluded

due to faulty MRI acquisitions (n=7) and severe image artefacts (n=2). The final cohort included 51 imaging sessions from 46 patients (three patients were scanned twice at different stages of disease progression and one patient thrice).

Upon visual inspection of the images of the 51 sessions, 24 (47%) sessions showed dMRI hyperintense lesions, 33 (65%) showed FET hotspot, and 17 (33%) sessions had both dMRI hyperintense lesions and FET-PET hotspot. Demographic and clinical information of the subset of patients presenting dMRI hyperintense lesions is summarised in Table 5.1.

Histological evaluation available at or around the scanning sessions which presented dMRI hyperintense lesions included: 12 (50%) glioblastoma multiform (GBM); six (25%) oligodendrogliomas, of which four grade III and two grade II; three (12%) astrocytomas of grade III; and three (12%) metastases (three sessions of the same patient).

Regarding the FET-uptake dynamics of the dMRI hyperintense lesion, 10 (42%) sessions showed increased FET-uptake dynamics in the region of the dMRI lesion, 10 (42%) sessions showed physiological FET-uptake dynamics in the dMRI lesion, and four (16%) sessions showed very little FET uptake. Examples for each group are shown in Fig. 5.1.

Table 5.1.: *Patient description and clinical information of the patients presenting dMRI hyperintense lesions. Patients are sorted according to their group: 1 - Increased FET uptake in dMRI lesion; 2 - No uptake in dMRI lesion; 3 - Physiological uptake in dMRI lesion. IoU - Intersection over union (Jaccard index). The entry "N.A." is shown in the last column whenever FET lesion size was 0 mL, i.e. there was no increased FET uptake observed.*

ID	Group	Sex	Age (years)	Tumour entity	Size of FET lesion	size of dMRI lesion	IoU dMRI / FET lesions
1	1	F	26	Anaplastic astrocytoma III	26.9 mL	4.55 mL	12.7 %
2	1	M	36	Astrocytoma II	28.0 mL	2.38 mL	7.71 %
3	1	M	52	Glioblastoma IV	40.9 mL	0.30 mL	0.50 %
4	1	M	53	Brain metastasis - Melanoma	0 mL	0.62 mL	N.A.
5	1	F	55	Glioblastoma IV	13.1 mL	1.30 mL	6.09 %
6	1	F	51	Glioblastoma IV	21.0 mL	1.90 mL	6.23 %
7	1	M	53	Glioblastoma IV	24.7 mL	0.76 mL	1.48 %
8	1	F	39	Oligodendroglioma II	2.68 mL	0.92 mL	0.13 %
9	1	F	34	Oligodendroglioma II	30.0 mL	7.05 mL	2.48 %
10	1	M	52	Oligoastrocytoma III	8.55 mL	0.17 mL	0 %
11	2	F	52	Oligoastrocytoma III	0 mL	6.90 mL	N.A.
12	2	M	58	Glioblastoma IV	34.4 mL	5.22 mL	0.61 %
13	2	M	62	Glioblastoma IV	0 mL	0.44 mL	N.A.
14	2	F	59	Astrocytoma III	18.8 mL	1.06 mL	0 %
15	3	F	49	Glioblastoma IV	12.8 mL	0.82 mL	0 %
16	3	F	33	Glioblastoma IV	7.05 mL	0.66 mL	1.34 %
17	3	F	33	Glioblastoma IV	12.1 mL	1.23 mL	0.84 %
18	3	M	53	Brain metastasis - Melanoma	0 mL	2.21 mL	N.A.
19	3	M	53	Brain metastasis - Melanoma	0 mL	2.76 mL	N.A.
20	3	F	51	Glioblastoma IV	0 mL	0.60 mL	N.A.
21	3	F	49	Glioblastoma IV	27.1 mL	8.41 mL	2.16 %
22	3	M	61	Glioblastoma IV	0 mL	0.72 mL	N.A.
23	3	F	53	Oligodendroglioma III	41.87 mL	6.40 mL	0.74 %
24	3	M	30	Oligoastrocytoma II	1.22 mL	3.47 mL	0.85 %

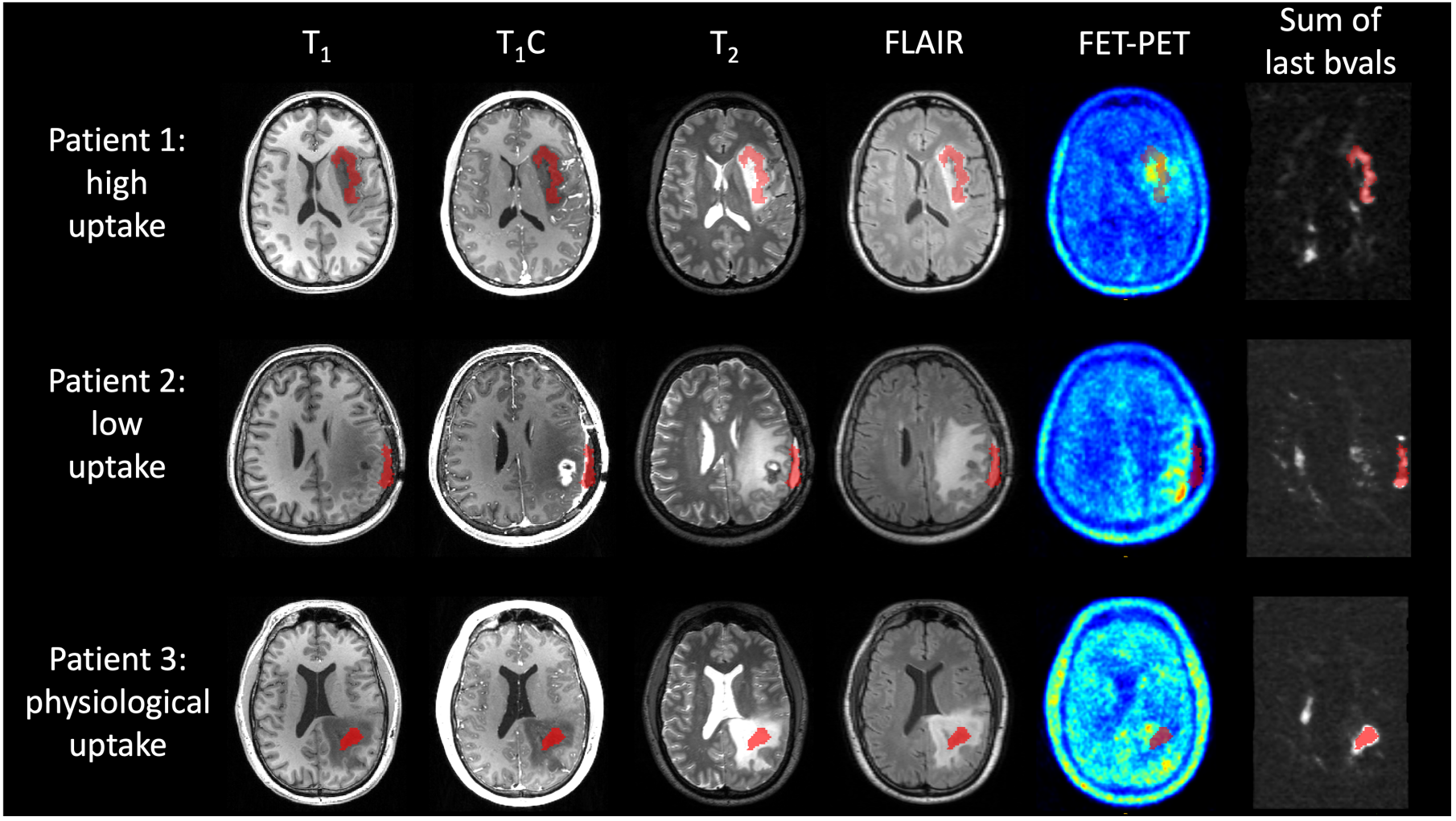

Figure 5.1.: *Example patients of each group based on FET uptake of the dMRI hyperintense lesion. From top to bottom: a 26 y.o. female with a recurrent Astrocytoma grade III in the left insula, belonging to the high uptake group (ID 1 from table* **??***); a 58 y.o. female with a recurrent GBM in the left parieto-occipital area, of the low uptake group (ID 12 from table* **??***); and a 30 y.o. male with a primary oligoastrocytoma grade II covering the pre- and post-central gyri, included in the physiological uptake group (ID 24 from table* **??***). From left to right are shown the following contrasts/modalities: T_1, T_1C, T_2, FLAIR, FET-PET, and summed image of the last 6 b-values of the diffusion protocol. The red overlay shows the hyperintense lesion mask. Note that even though the summed image shows signal in areas of the WM, these were not consistent across b-vectors and therefore were not included in the hyperintensity mask.*

5.3.2. Mono, bi- and tri-exponential

The mean estimated model parameters are shown in Table 5.2, while the corrected AIC values for each model in each tissue class are shown in Table 5.3.

5.3.3. NNLS simulations

In Figs. 5.2 and 5.3 are summarised the simulation results for the models with predominant free water and predominant very slow component, and Figs. 5.4 and 5.5 summarise the results of the λ dependence of the results for the other two models.

The simulations show that peaks with low spectral distance (i.e. diffusivity values too close to each other) could not be properly resolved, but at larger spectral distances, the peaks could be accurately identified. This is exemplified in Figs. 5.2 and 5.3. The peak of the non-dominant component that is more readily identified at lower SNR levels is never the one immediately adjacent to the dominant component. Even at higher SNR levels, NNLS seems to struggle to deconvolve peeks which are too close to each other, instead presenting with a convolved peak of intermediary diffusivity, best seen in Fig. 5.3 (second and third rows). The influence of each fraction's contribution is also relevant: uncertainty in the estimation of the diffusivity pools increases with decreasing fraction.

Regarding the λ simulations, it becomes apparent that using large regularisation factors leads to an over-smoothing of the results, as seen in Figs. 5.3 and 5.4. A relationship between SNR and λ is also apparent, as the decay of peak amplitudes is much sharper at increased SNRs with increasing λ.

5.3.4. NNLS *in vivo*

The average NNLS spectra for each tissue are presented in Fig. 5.6, together with their 95% confidence intervals and the underlying diffusivity compartments.

The spectra of the physiological tissues show typical peak values: WM has a first peak around $0.45\text{x}10^{-3}$ mm^2/s and a second peak around $1.7\text{x}10^{-3}$ mm^2/s; GM shows a first peak around $0.8\text{x}10^{-3}$ mm^2/s and again at $2.2\text{x}10^{-3}$ mm^2/s; and CSF shows a relatively small and wide peak between 0.4-$0.6\text{x}10^{-3}$ mm^2/s and a strong peak around $3\text{x}10^{-3}$ mm^2/s. The

Table 5.2.: *Estimated model parameters for mono-, bi-, and tri-exponential decays in each tissue class. Values represent the mean ± standard deviation across patients. GM: gray matter (N = 51); WM: white matter (N = 51); CSF: cerebrospinal fluid (N = 51); Oed: oedema (N = 49); Hot: FET-PET hotspot (N = 33); Hyp: dMRI hyperintense lesion (N = 24)*

	ADC (x10^{-3} mm^2/s)					
	GM	WM	CSF	Oed	Hot	Hyp
Mono-exponential	1.06 ± 0.06	0.80 ± 0.05	2.04 ± 0.31	1.29 ± 0.24	1.22 ± 0.22	0.96 ± 0.32

	f_{slow}						D_{slow} (x10^{-3} mm^2/s)						D_{fast} (x10^{-3} mm^2/s)					
	GM	WM	CSF	Oed	Hot	Hyp	GM	WM	CSF	Oed	Hot	Hyp	GM	WM	CSF	Oed	Hot	Hyp
Bi-exponential	0.50 ± 0.04	0.43 ± 0.03	0.17 ± 0.06	0.26 ± 0 07	0.33 ± 0.10	0.27 ± 0.10	0.61 ± 0.03	0.39 ± 0.03	0.41 ± 0.07	0.48 ± 0.10	0.50 ± 0.08	0.25 ± 0.07	2.67 ± 0.19	1.89 ± 0.15	3.00 ± 0.02	2.05 ± 0.28	2.24 ± 0.32	1.82 ± 0.38

	f_{vslow}						f_{slow}						f_{fast}						
	GM	WM	CSF	Oed	Hot	Hyp	GM	WM	CSF	Oed	Hot	Hyp	GM	WM	CSF	Oed	Hot	Hyp	...
Tri-exponential	0.01 ± 0.01	0.04 ± 0.03	0.02 ± 0.04	0.04 ± 0.04	0.04 ± 0.05	0.10 ± 0.05	0.50 ± 0.04	0.48 ± 0.04	0.22 ± 0.07	0.25 ± 0.10	0.30 ± 0.11	0.32 ± 0.13	0.49 ± 0.04	0.48 ± 0.03	0.76 ± 0.05	0.71 ± 0.10	0.65 ± 0.11	0.57 ± 0.16	

	D_{vslow} (x10^{-3} mm^2/s)						D_{slow} (x10^{-3} mm^2/s)						D_{fast} (x10^{-3} mm^2/s)						
	GM	WM	CSF	Oed	Hot	Hyp	GM	WM	CSF	Oed	Hot	Hyp	GM	WM	CSF	Oed	Hot	Hyp	
...	0.40 ± 0.10	0.11 ± 0.05	0.45 ± 0.03	0.31 ± 0.16	0.33 ± 0.16	0.12 ± 0.04	0.62 ± 0.03	0.51 ± 0.01	0.57 ± 0.04	0.55 ± 0.05	0.57 ± 0.10	0.60 ± 0.15	2.69 ± 0.21	2.13 ± 0.14	3.60 ± 0.33	2.11 ± 0.24	2.34 ± 0.43	2.29 ± 0.57	

Table 5.3.: *Corrected AIC of the different tissue classes for all models. The values presented are the mean ± standard deviation across the patients. The lower the AIC, the better the model.*

Model	GM	WM	CSF	Oedema	FET hotspot	dMRI lesion
Mono-exp	-147 ± 4.24	-142 ± 2.66	-139 ± 6.94	-157 ± 9.75	-152 ± 11.4	-136 ± 10.6
Bi-exp	-177 ± 5.12	-177 ± 5.00	-169 ± 9.55	-197 ± 12.5	-188 ± 17.8	-215 ± 18.4
Tri-exp	-164 ± 5.12	-166 ± 5.52	-162 ± 8.58	-185 ± 13.4	-176 ± 18.1	-213 ± 32.0
NNLS	-244 ± 5.61	-243 ± 5.75	-247 ± 8.24	-263 ± 13.3	-254 ± 18.2	-302 ± 33.3

pathological spectra show distinct signatures: the oedema curve shows peaks at the same diffusivity values as those for WM, but the peak at the highest diffusivity value is much stronger than that of the lowest diffusivity value (almost 3x higher). The FET-PET hotspot also shows two peaks with similar ratios as those from oedema, albeit at slightly higher diffusivity values, at 0.52x10^{-3} mm^2/s and 1.9x10^{-3} mm^2/s. Finally the dMRI hyperintense lesion also shows two identifiable peaks, one around 0.4x10^{-3} mm^2/s and one at 1.7x10^{-3} mm^2/s.

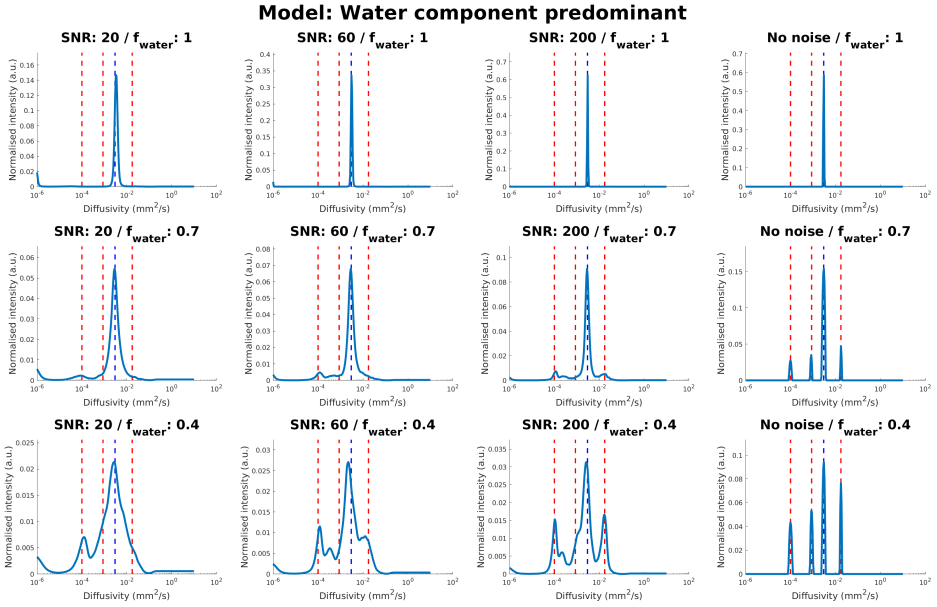

Figure 5.2.: *Mean spectra of the simulations of the effects of SNR and diffusivity pool fraction. The presented model is with predominant free water component. The spectra are displayed in semi-logarithmic plot in blue, while the ground-truth diffusivities in horizontal, dashed lines: blue for predominant component, red for others.*

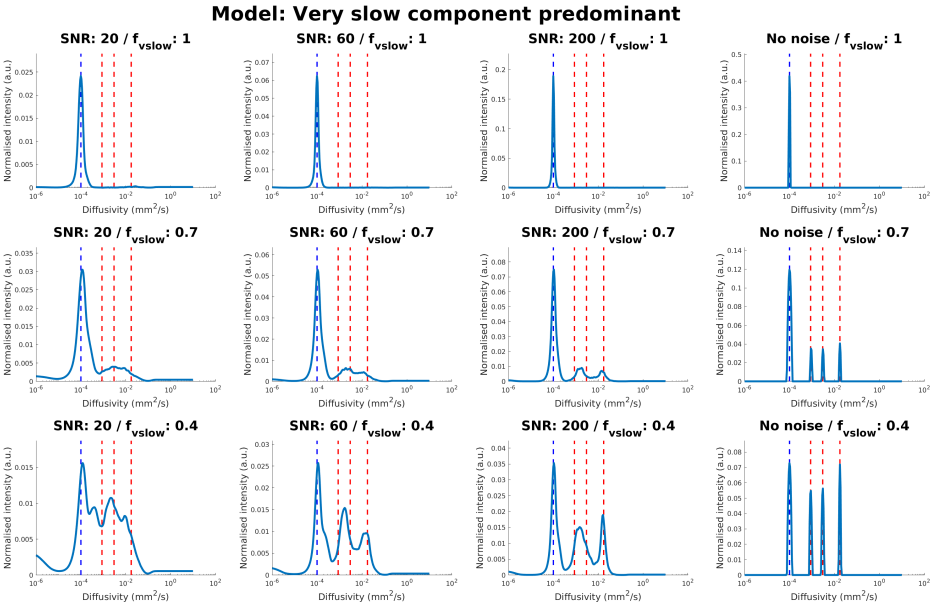

Figure 5.3.: *Mean spectra of the simulations of the effects of SNR and diffusivity pool fraction. The presented model is with predominant very slow component. The spectra are displayed in semi-logarithmic plot in blue, while the ground-truth diffusivities in horizontal, dashed lines: blue for predominant component, red for others.*

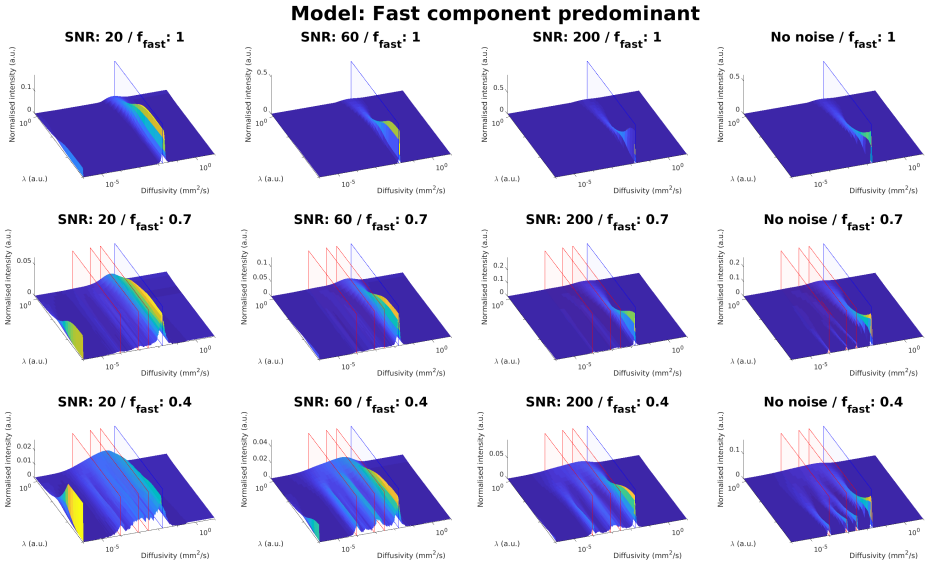

Figure 5.4.: *Mean spectra of the simulations of the effects of λ, SNR, and diffusivity pool fraction. The presented model is with predominant fast component. The spectra are displayed as surface plots in semi-logarithmic scale (x and y axis: diffusivity and λ, respectively). The ground-truth diffusivities are displayed as semi-transparent planes: blue for predominant component, red for others.*

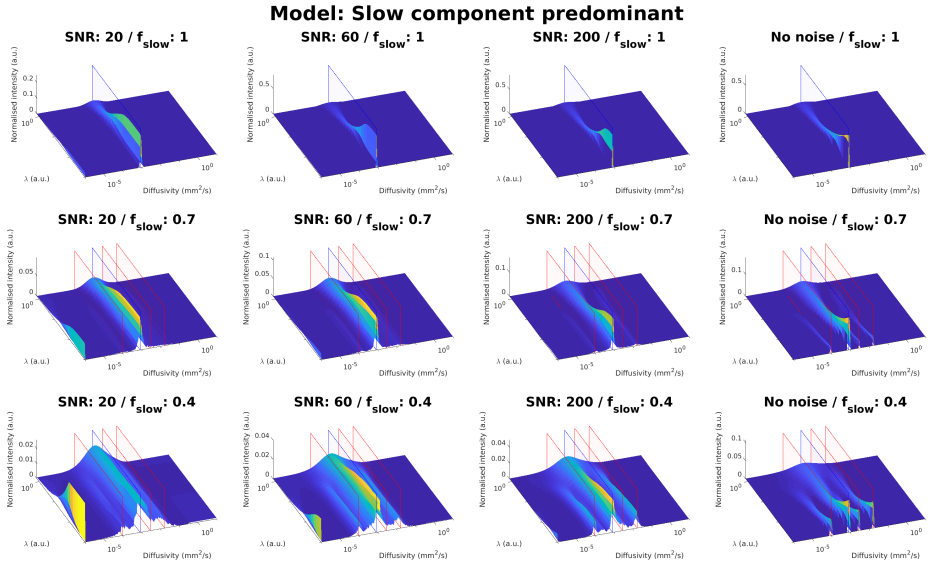

Figure 5.5.: *Mean spectra of the simulations of the effects of λ, SNR, and diffusivity pool fraction. The presented model is with predominant slow component. The spectra are displayed as surface plots in semi-logarithmic scale (x and y axis: diffusivity and λ, respectively). The ground-truth diffusivities are displayed as semi-transparent planes: blue for predominant component, red for others.*

The boxplots with the summed amplitudes in each compartment and their respective Kruskal-Wallis results are shown in Figure 5.7. Despite the lack of a clear peak in Fig. 5.6 for the dMRI lesion in compartment 1, the summed amplitude of the dMRI hyperintense lesion is significantly higher than that of any other class except for WM, which had the second highest amplitude. In compartment 2, the amplitude in WM is significantly higher than any other tissue. The dMRI hyperintensity presents with the second highest amplitude. Compartment 3 is dominated by GM, which was significantly higher than all the other tissues. In this compartment, the contribution of FET-PET hotspot was second highest, while the dMRI hyperintensity was the lowest. Compartment 4 is marked by a high sum of amplitudes in the oedema ROI relative to the normal appearing tissues; no significant difference to the pathological ROIs. Additionally, the sum of amplitudes in the CSF was significantly smaller than all other tissue classes and no significant differences were seen between WM and dMRI hyperintensity, nor WM and PET hotspot. Compartment 5 is dominated by CSF, with all other tissues showing a significantly smaller summed amplitude. Finally, compartment 6 is also dominated by CSF, followed by GM.

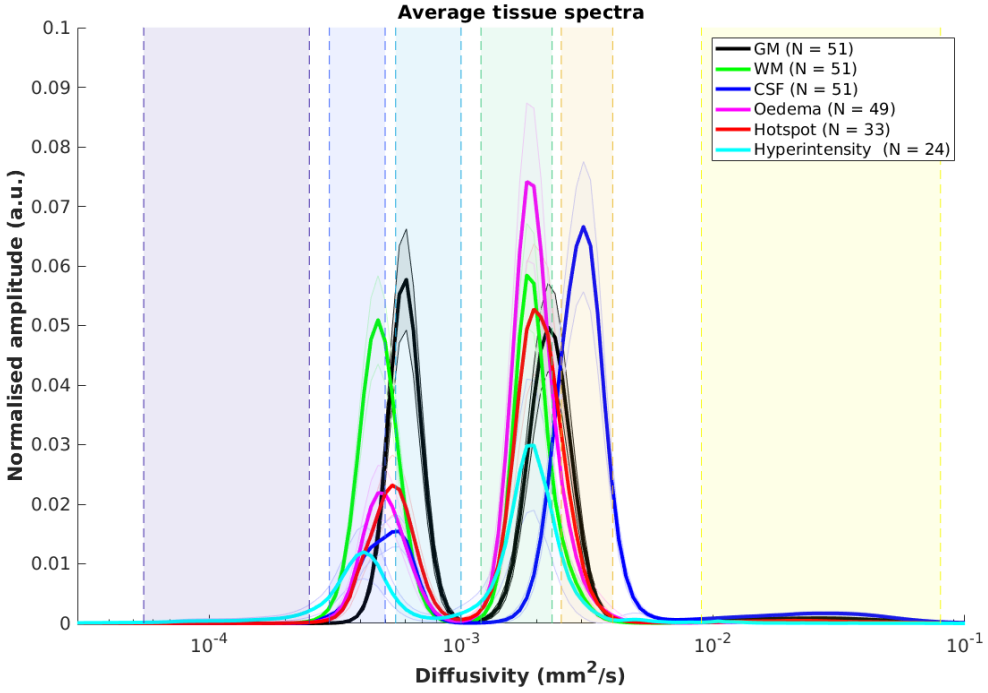

Figure 5.6.: *Average NNLS tissue spectra. The bold lines represent the average spectrum across patients, with the shaded areas around it the 95% confidence interval (shaded area around the lines). The vertical bars represent the limits of the diffusivity compartments. N (in the legend) represents the number of patients from which a specific tissue class was extracted.*

In Fig. 5.8 are the individual spectra and summed images over the different compartments for the three example patients of Fig. 5.1.

When looking at the group divisions based on the FET-uptake dynamics, the mean dMRI hyperintense lesion spectra for each group are shown in Fig. 5.9. Only compartment 4 showed statistically significant increased spectral amplitude of the increased uptake group vs the reduced uptake group (Kruskal-Wallis, corrected p-value = 0.02).

Regarding distinction based on tumour entity, no differences were found in any of the compartments, apparent by the spectra shown in Fig. 5.10.

5.4. Discussion

The study of brain tumour with dMRI is currently a hot topic. The microstructural tumour environment is highly heterogeneous which lends itself to be studied with a technique

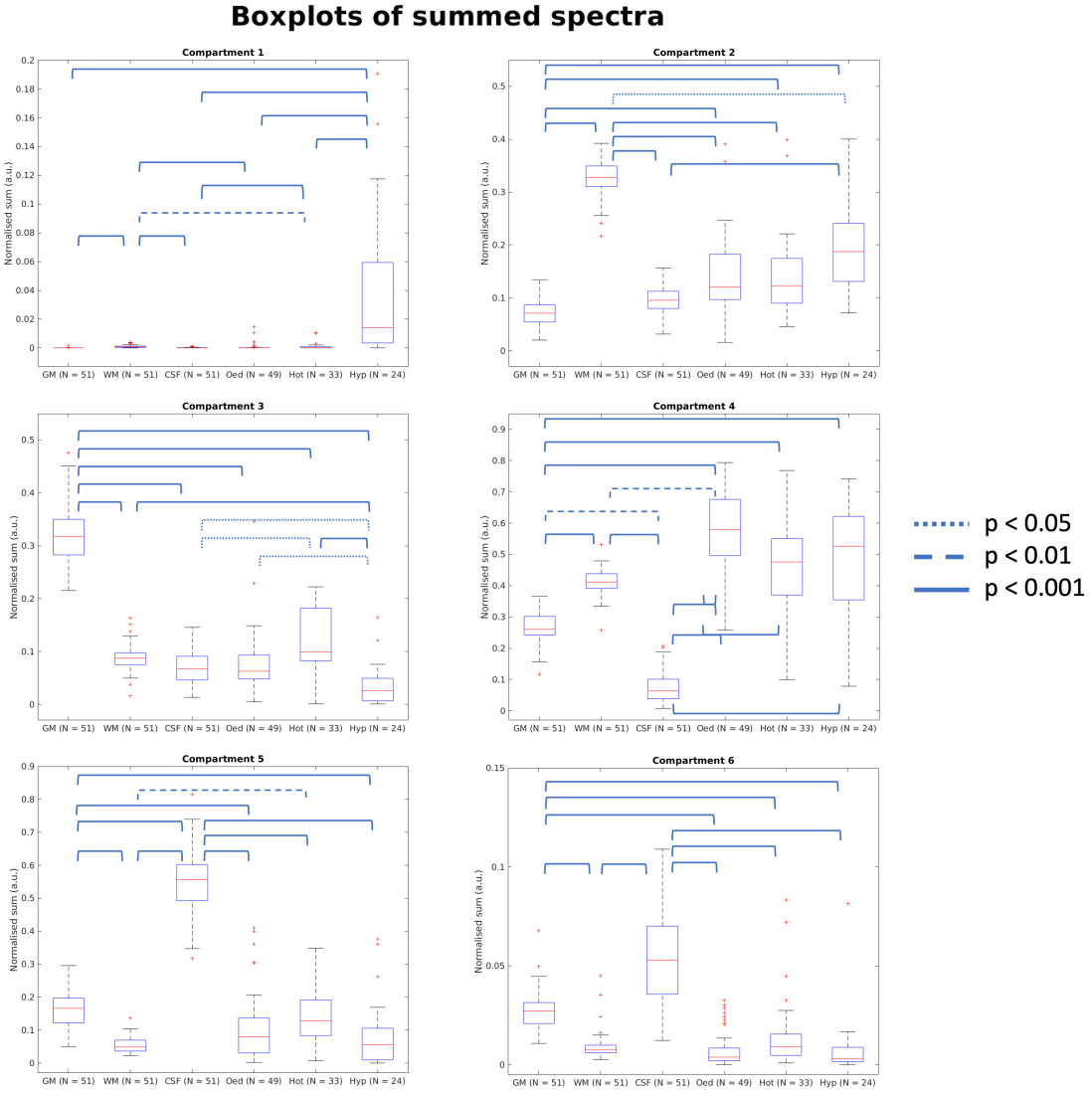

Figure 5.7.: *Boxplots of summed normalised amplitudes in the different diffusivity compartments. The horizontal lines on top of the boxplots represent significantly different pairs of summed amplitudes within the compartment (Kruskal-Wallis, Bonferroni corrected). The type of line reflects the p-value: dotted - $p < 0.05$; dashed - $p < 0.01$; continuous - $p < 0.001$*

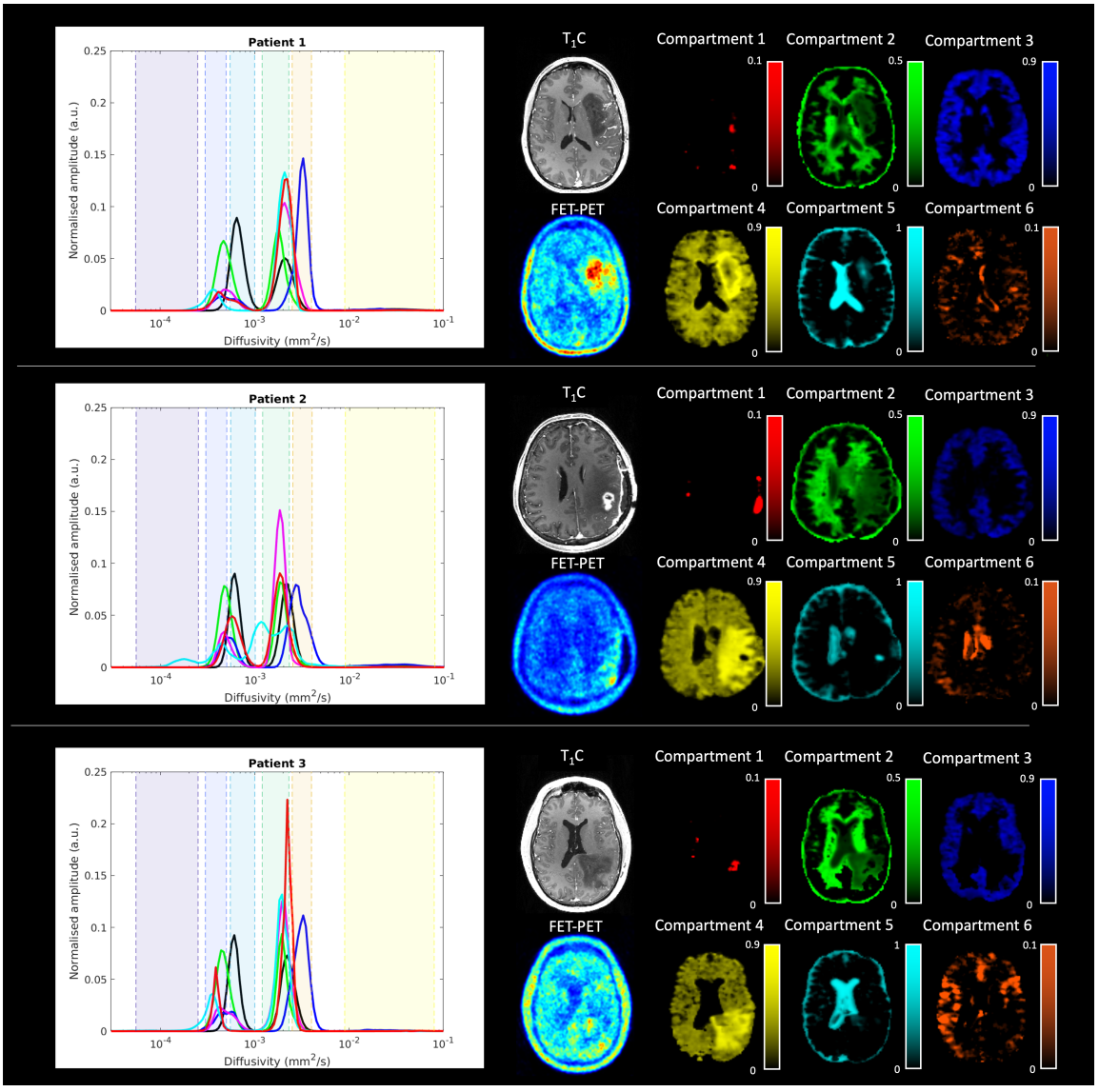

Figure 5.8.: *Tissue spectra and summed compartment images for the three example patients in Fig. 5.1*

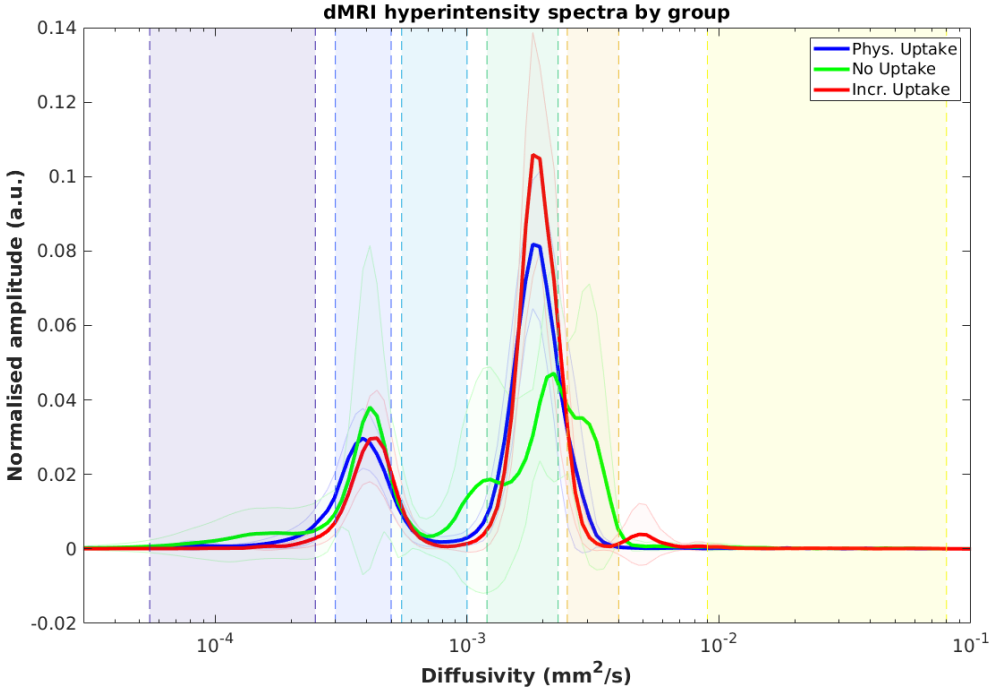

Figure 5.9.: *Average NNLS dMRI hyperintensity spectra sorted by FET-PET uptake groups. The bold lines reflect the mean spectral amplitude and the shade around them are the respective 95% confidence intervals. A significant difference in spectral amplitudes is present in compartment 4 between the increased and no uptake groups.*

able to pick up alterations at the microscopic level, like dMRI. Clinical workflow with dMRI typically involves using a single diffusion-weighted image, with a b-value of around 1,000 s/mm^2. Assessment can then be carried out either via the diffusion-weighted images themselves or via the ADC. However, it has been shown that higher b-values provide more sensitivity and specificity to the assessment of tumour grade (Seo et al., 2008; Kang et al., 2011; Chu et al., 2013; Han et al., 2015; Zeng et al., 2017). In this work, we analysed a diffusion dataset ranging from 50 to 10,000 s/mm^2 using NNLS in a cohort of brain tumour patients with the goal of identifying tissue spectral characteristics. A subset of these patients was identified as developing conspicuous restricted diffusion lesions, presenting as an increase in the dMRI images. NNLS was then employed on these lesions to try to shine a light on their nature.

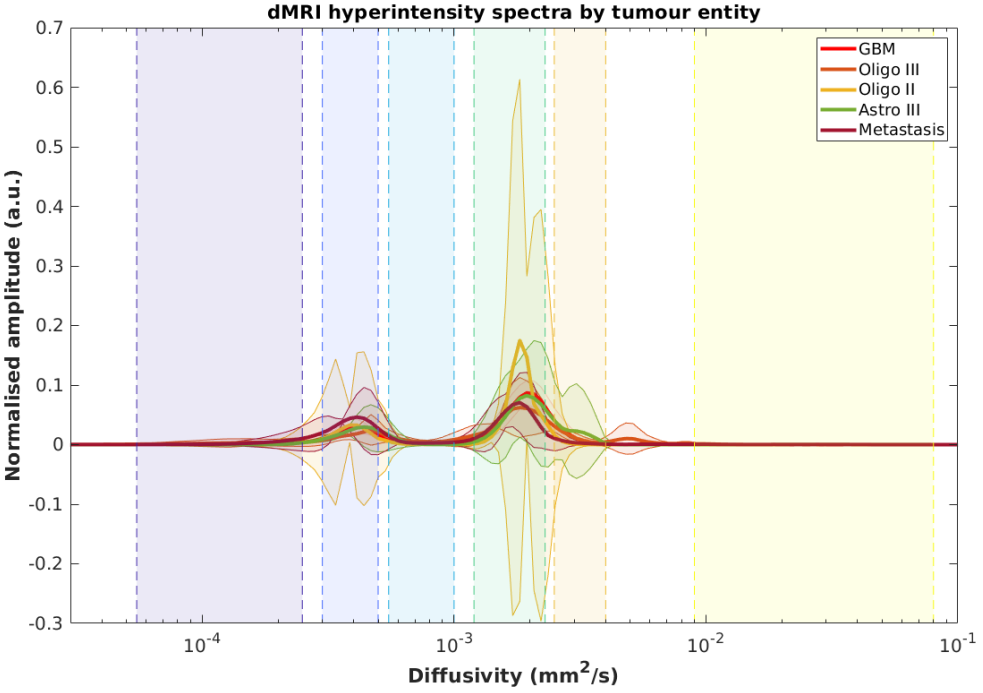

Figure 5.10.: *Average NNLS spectra per tumour entity in the cohort. The bold lines reflect the average spectral amplitude and the shaded areas the 95% confidence interval. No significant differences were seen between any of the entities in any of the compartments.*

5.4.1. dMRI hyperintense lesions

The origin of such dMRI hyperintense lesions is still elusive. Some studies implicate their appearance to tumour hypoxia as a result of GBM treatment with bevacizumab (Bähr et al., 2014; Mong et al., 2012; Rieger et al., 2010). This drug is a vaso-endothelial growth factor inhibitor, preventing the growth of new blood vessels, required to allow tumour expansion. Without new vessels to sustain the tumour, it enters a state of hypoxia, leading to cell death and increasing overall survival (Bähr et al., 2014). Other groups mention such lesions are related to tumour grade and precede the development of enhancing tumour (Gerstner et al., 2010; Gupta et al., 2011). This suggests that the lesions are a reflection of the tumour's aggressiveness and infiltration, with the presence of these lesions being implicated with poor prognosis. Others still point to either the development of coagulative necrosis and/or viable tumour (Farid et al., 2013; LaViolette et al., 2014; Nguyen et al., 2016; Zhang et al.,

2016; Goyal et al., 2018), with increased overall survival in the case of only necrosis, and decreased in the presence of viable tumour.

In our study, only four patients had history of bevacizumab treatment, of which three developed dMRI hyperintensities. The tumour entities that developed these signals were also not exclusively GBM, as the literature seems to suggest. In fact, in our cohort, two patients with low grade glioma (oligodendroglioma II) and one patient with a brain metastasis also developed these lesions.

The histological information gathered from our patients pertains only to the tumour proper region, and not from the dMRI lesion. We used FET-PET dynamic curves of the hyperintense region to divide the cohort into three groups - increased, physiological, and reduced FET uptake -, under the assumption that the dMRI hyperintense lesions with high FET uptake would correlate with viable tumour (Pauleit et al., 2005), while those with low FET uptake would correlate with necrotic regions. Potentially one of the most interesting findings is within the group with hyperintense dMRI lesions with physiological FET uptake. The presence of these dMRI lesions in a region with physiological metabolism suggests that dMRI is sensitive to tumour-related alterations that FET-PET is not. Looking at the spectra of Fig. 5.8, these lesions could reflect regions of tumour progression since the dMRI lesion spectra of the physiological uptake group is more similar to that of the group with increased FET uptake, although this warrants further investigation.

5.4.2. NNLS fit

In this work, NNLS was used to fit diffusion data with b-values up to 10,000 s/mm^2. Such images reveal areas where diffusion is very restricted, indicative of a high density of diffusional microstructural barriers. These barriers can be macroscopically anisotropic, as is the case in WM regions with highly aligned axons; or, as seen in the previous sections and chapters, macroscopically isotropic, arising from pathological processes. The use of three diffusion probing directions in this work allows for the distinction of these two.

Fitting data with plain NNLS is known to produce sparse spectra, composed of several spikes. To prevent this, Tikhonov regularisation can be introduced (Tikhonov and Arsenin,

1977), which penalises sparse solutions in favour of smooth ones. This regularisation can be of zero order (Mackay et al., 1994), first order (Kroeker and Henkelman, 1986), or second order (Whittall and MacKay, 1989). It relies on a parameter, λ, which has to be estimated for every fit. Approaches to estimate λ are manifold, of which two are amongst the most common: one based on the so-called "L-curve" (Hansen, 1992) and another based on the χ^2 of the fit (Whittall and MacKay, 1989).

The L-curve method is based on fitting NNLS for a full range of λ values and then plotting the norm of the regularised solution against the norm of the residuals (Hansen, 1992). This plot contains a vertical portion on the left-hand side and a horizontal portion on the right-hand side, resembling the letter "L" from which its name is derived. The optimal λ is determined at the corner of the L, that is, when the plot turns from vertical to horizontal.

On the other hand, choice of λ based on the χ^2 is performed by first fitting the signal without regularisation and then fitting it again with regularisation. The two solutions will result in two different χ^2 values (driven by the residuals) and a regularised solution will be chosen, if the χ^2 ratio falls within a specific range (Graham et al., 1996). In myelin water studies, ratios between 1.02 and 1.025 are considered (Alonso-Ortiz et al., 2018). Conversely, in this study a ratio range of 1.005 to 1.01 was used. This was empirically determined as being a range that ensured a sufficiently low λ without overly smoothing the results - higher ratios resulted in too high λ leading to over-smoothing (see e.g. Fig. 5.4).

A recent study on myelin water fraction estimation using NNLS looked at the effects of the order of Tikhonov regularisation and the strategies to estimate λ (Canales-Rodríguez et al., 2021). They found that for this particular quantity, χ^2 with zero order regularisation performed the best for moderate levels of SNR (SNR=50-150 in the study by Canales-Rodríguez et al. (2021)). The same regularisation strategy was used in the present study. It would be of interest to investigate if other strategies might be better suited for dMRI data taking into account factors like SNR, number of points in the fit, and spectral separation of the pools.

NNLS Simulations

Simulations of the NNLS fit showed that this technique requires a sufficient degree of SNR to accurately retrieve the simulated diffusivity pools. At the lower bound of SNR, SNR = 20, NNLS could not properly resolve peaks which are too close to each other. Instead, it returns a peak at the mid point between the two original peaks. Previous work done on a kidney model suggested that an SNR of 80 and a number of b-values of 25 provides a mean absolute percentage error of around 25-30% (Periquito et al., 2021). The simulations performed here show a similar trend, as at an SNR of 60 and with 24 unique b-values, the spectral resolution was greatly increased, albeit still presenting with convolved peaks if spectral separation was too small. Identification of all four pools was not possible, even at an SNR of 200 - as seen in, e.g. Fig. 5.3 -, although the accuracy of the results greatly improved.

When looking at the λ dependency of the spectra, it is shown in Figs. 5.4 and 5.5 that the smoothness of the results is also dependent on the SNR. That is to say that at lower SNR levels, a higher λ is required to obtain spectra which are less contaminated by noise. This can have implications in the choice of λ range, as a too narrow range could result in sub-optimal solutions; and of χ^2 ratio, as mentioned above.

It can, therefore, be concluded that NNLS benefits greatly from increasing SNR, implying that denoising is important when employing NNLS. In high b-value dMRI data, denoising is even more relevant due to the noise floor effect (Bernstein et al., 1989). Owing to the decaying nature of the diffusion signal with b-value, at very high b-values the noise floor will substantially contribute to the measured signal, leading to a non-linear effect over b-values. At b-values beyond 5,000 s/mm^2, the retrieved signal is almost only noise for most voxels in the image - see Fig 5.1, last column -, with only voxels with highly restricted micro-environment perpendicular to the acquired diffusion direction producing any appreciable signal above the noise floor. If this effect is not removed, data fitting will be impacted by the noise floor, leading to under estimation of the diffusivity values. Denoising approaches should therefore be able to compensate this effect, especially when analysing very high b-value data.

For the *in vivo* data, we used magnitude based PCA denoising (Oros-Peusquens and Shah, 2013; Veraart et al., 2016a,b; Cordero-Grande et al., 2019). Its usefulness has been demonstrated in a variety of studies, but in a recent study it has been shown that it does not properly deal with the noise floor issue (Manzano-Patron et al., 2023). Conversely, algorithms based on complex data, i.e. magnitude and phase, were shown to improve noise floor biases (Manzano-Patron et al., 2023). Inclusion of a complex-based denoising strategy was however not possible due to the lack of phase data. Provided phase data would be available, it would be interesting to test the influence of the different denoising techniques on the NNLS results.

5.4.3. *In vivo* experiments

In this work it was demonstrated that NNLS seems to explain the measured dMRI data better than either of the conventional mono-, bi-, or tri-exponential fits, as evidenced by the lower AICc. This is the case in spite of the increased level of complexity of NNLS in terms of estimated parameters: essentially, NNLS estimates N parameters per fit, where N is the amount of steps in the diffusivity spectrum (250 in this study); while the fixed compartment models estimate two, four, or seven parameters (mono-, bi-, and tri-exponential, respectively, including S_0 as a fit parameter). With increasing number of parameters, it is expected that the fitting errors decrease. However, arbitrarily increasing the number of fit parameters doesn't necessarily translate in a more plausible model. The AICc is a measure that weighs the fitting errors against the estimated parameters in order to identify, from a set of nested models, which of them better explains the data while penalising models with higher degrees of freedom (Akaike, 1998).

When looking at the values of the fixed component fits, the mono-exponential fit shows ADC values in accordance with those reported in the literature (Lebel et al., 2008), as well as those reported in the previous chapter (see 4.3).

When looking at the bi-exponential case, f_{slow} seems overestimated in GM and underestimated in WM, as one would expect a higher fraction of slow diffusivity in WM than in GM (Kiselev and Il'yasov, 2007). However, this can perhaps be explained when looking at D_{slow}

and D_{fast}. In GM, the estimated D_{slow} shows a value that, albeit underestimated, is still within range of reported literature values (Mulkern et al., 1999; Kiselev and Il'yasov, 2007), while the D_{fast} is close to that of free water. On the other hand, in WM, the bi-exponential model estimates D_{slow} and D_{fast} in accordance to reports from the literature (Mulkern et al., 1999; Clark and Le Bihan, 2000; Mulkern et al., 2001). The presence of a free water compartment in GM can be indicative of partial volume effects from voxels at the cortical level close to the CSF.

The tri-exponential fit seems to deal with this issue, as now the GM voxels show the typical diffusivities and diffusivity fractions of the very slow and slow components (literature on bi-exponential fits calls these slow and fast, respectively), plus a free water component (Clark and Le Bihan, 2000). Regarding the other normal appearing tissue classes, the values also agree with the literature (Mulkern et al., 1999; Clark and Le Bihan, 2000; Mulkern et al., 2001; Zeng et al., 2018). Regarding the pathological tissue classes, the dMRI hyperintensity shows the highest f_{vslow}, consistent with a region of highly restricted diffusion. The other two ROIs show f_{vslow} values similar to those of WM but D_{vslow} values similar to those of GM. The parameter f_{slow} is comparable between the FET-PET hotspot and the dMRI lesion, and higher than that seen in oedema, while D_{slow} is similar between all three pathological ROI. Conversely, oedema has a higher f_{fast} than the other two pathological tissues.

A high f_{high} in the oedema region can be a reflection of the accumulation of "free" water in the tissues as a result of pathological processes. Taking the nomenclature of Assaf and Cohen (1996), "free" water is considered to be sufficiently far away from membranes and other macro-molecules such that it behaves like bulk water at the probed diffusion times. As the ratio of "free" water increases, so too does the f_{fast} (Assaf and Cohen, 1996). Conversely, "bound" water, defined as water which interacts directly with macro-molecules, has a slow diffusing nature (Assaf and Cohen, 1996). A relative increase in f_{vslow} might indicate that the amount of membranes with which water molecules interact is increased in a given region.

Looking at the NNLS, all the tissue spectra produced consistently two peaks. The amplitude of the spectra produced by NNLS indicate the relative contribution of that particular diffusivity pool to the overall observed signal. In order to facilitate the analysis of

these spectra, the diffusivity range was divided into six compartments. Their borders were defined based on a combination of literature (Assaf and Cohen, 1996; Mulkern et al., 1999; Clark and Le Bihan, 2000) and empirical observation, in such a way as to provide maximal tissue separation per compartment. This was done to highlight the potential of NNLS in identifying tissue signatures based on the relative spectral amplitudes in the different compartments. The compartments are interpreted thusly, from most to least straightforward: compartments 5, 3, and 2 are dominated by CSF, GM, and WM, respectively, and therefore capture the respective microstructure; compartment 6 covers the range of diffusivity values typically seen in IVIM; compartment 1 represents tissue of highly hindered diffusion, which includes primarily regions of dMRI hyperintensity ("bound" water in Assaf and Cohen (1996)); and compartment 4 represents diffusing water molecules in an intermediate regime between "bound" and "free", which exchanges with both during the diffusion experiment (Assaf and Cohen, 1996).

Here, again, the notion of "free" and "bound" water appears and can be associated to the highest diffusivity peak of CSF and to the lower diffusivity peak ensemble of all ROIs, respectively (Assaf and Cohen, 1996; Mulkern et al., 1999). The nuances in the peak diffusivities can be a reflection of the underlying tissue microstructure. For example, among the peaks of the "bound" water, the dMRI hyperintense lesion peak has the slowest diffusivity ($0.4\text{x}10^{-3}$ s/mm^2) while GM has the highest ($0.6\text{x}10^{-3}$ s/mm^2). These differences in the diffusivities can be a result of the type of barriers with which water interacts: some bind water more than others, hence restricting diffusion more than others, ultimately creating distinct pools all associated to "bound" water diffusion. The same can be said of the intermediate pools of compartment 4, except here the barriers themselves might not play such a significant role, but rather the distinctive factor might be the exchange rate between the different regimes.

5.4.4. Limitations

This study is not without limitations. Due to the random patient assignment, our sample is very heterogeneous, not only in diagnosis, but also in stage of disease, types of treatment, etc.

Such a small and heterogeneous cohort precludes the identification of pathology/treatment-specific spectrum features, which would be of great value for clinicians. The heterogeneity of our sample can also explain the lack of distinct characteristic NNLS spectra for the tumour entities, when analysed by groups as per Fig. 5.10.

The clinical aspect of this study focused primarily on the dMRI lesions. However, the biopsy results which confirm the tumour entities are not derived from the dMRI lesions, but rather from either the clinical MRI or FET-PET. It would be very interesting to acquire biopsy samples from the dMRI lesions and correlate biopsy findings to NNLS spectra in these regions. Such an analysis could reveal biomarkers which would help identify the nature of such lesions in brain tumour patients, with potential implications towards treatment planning.

Some imaging sessions showed multiple hyperintensities (7 out of the 24 with hyperintensities). These were always grouped and treated as a single one. It is possible to argue that each hyperintensity in a single image can arise from different underlying phenomena, e.g. one hyperintensity can be a result of infiltrative tumour and another of necrotic tissue. If this is the case, and assuming each of these would present with a distinct NNLS spectrum, this contributes to uncertainty in the results. A follow-up analysis assigning not the imaging session but the hyperintense lesions to one of the three groups (increased, physiological, or no uptake) would help mitigate this uncertainty.

Additionally, no survivability data was gathered, which hindered the possibility of evaluating the prognostic value of the diffusion properties of the dMRI lesions. It has been shown that dMRI metrics such as FA and MD hold prognostic value in brain tumours (Jütten et al., 2019; Huber et al., 2016; Xiong et al., 2016; Rydelius et al., 2023). A tool like a diffusivity spectrum contains much richer information than a single value, as suggested by histogram studies (Kang et al., 2011; Kurokawa et al., 2023).

Regardless, the results shown here hint towards a potential tool for the advanced characterisation of microstructural changes in tissue. A method like NNLS in dMRI can be leveraged with a larger and more comprehensive sample, allowing to build larger and more

homogenous groups where NNLS spectra could potentially be used for grading, predicting response to treatment, or even predict recurrence.

6. Summary and Outlook

A thorough characterisation of pathological tissues is expected when complementary information is taken into account. Clinical routine makes use of imaging-based, metabolic, and molecular assessments to characterise brain tumours (Louis et al., 2021). However, clinical imaging is often qualitative and can benefit from quantitative approaches. Diffusion MRI can provide quantitative information about the molecular diffusion in the tissues, which has correlates to the underlying tissue microstructure. In dMRI, therefore, the complementary information comes from the different diffusion regimes, which have already been assessed with respect to their grading qualities (Svolos et al., 2014; Verger et al., 2017; Qi et al., 2017; Jiang et al., 2015; Van Cauter et al., 2012) and were found to be useful, to a greater or lesser extent. However, a multi-parametric approach has not yet been fully exploited.

In this work, methods for the analysis of multi-b-value dMRI data were developed, probing different diffusion regimes, with the aim of allowing a multi-parametric approach to tissue characterisation in clinically feasible times. These methods included a protocol and respective processing pipeline for joint IVIM/NG-diffusivity acquisition, and the analysis of broad range of b-value data using NNLS.

The first part of this work assessed the feasibility of acquiring several diffusion parameters for the characterisation of tumours within a short measurement time. Three diffusion regimes were investigated: IVIM, characterised by D^* and f; Gaussian diffusion, characterised by D_{app}; and non-Gaussian diffusion, characterised by K_{app}. These metrics were compared to similar ones derived from established protocols in an *in vivo* cohort of brain tumour patients. The Non-Gaussian diffusion metrics estimated from the proposed protocol showed high correlation with those from the standard DKI acquisition. Against to the initial hypothesis,

IVIM metrics were poorly correlated with DSC metrics, suggesting that they, at least in part, reflect different aspects of the microstructural environment. It was also shown that, to some extent, the IVIM parameters obtained from this protocol are reflective of tissue physiology and therefore hold some value in characterising brain tumours.

The proposed protocol covers the relevant b-value range well enough to allow for a simultaneous IVIM-diffusion-kurtosis fit. The short acquisition time means it can satisfy the strict demands of clinical routine, while also providing established standard information ("trace" at b = 1,000 s/mm^2). Characterisation of tumour/oedema tissue using D_{app} and $K_{app}$was shown to be similar to that obtained with a commonly used kurtosis acquisition, suggesting that the tumour grading power of D_{app} and K_{app} is kept to a large extent. Additionally, the IVIM parameters, which have also been shown to have grading power (Puig et al., 2016; Federau et al., 2014a; Iima et al., 2014, 2015), can be determined with reasonable precision and accuracy when using an ROI-based fit. The low correlation between IVIM and DSC seen here could be a hint that using both sets of parameters might provide complementary information in the context of tumour tissue. It is expected that through multi-parametric analysis, 'tumour signatures', like the one suggested in Fig. 4.6, can be explored, yet their value remains to be proven.

As for the second part of this work, the feasibility of NNLS in brain tumour was demonstrated using dMRI data from 50 to 10,000 s/mm^2. The clinical evaluation was focused on the characterisation of diffusion restricted lesions marked by hyperintense regions in the very high b-value images. These seem to be of importance in the management of brain tumour patients but their nature remains elusive. It is important to note that the information provided by the diffusion restricted lesion and the FET-PET hotspot is not the same, as demonstrated by the varied degree of overlap between the two lesions - shown in Table 5.1. One can conclude that dMRI might be sensitive to tumoural processes to which FET-PET is not. In fact, NNLS derived spectra seem to pick up on the microstructural differences of these lesions, showing distinct diffusivity signatures. Such a tool could hold clinical value. In this study, however, the heterogeneity of the cohort and the lack of

histological assessment at the site of the hyperintense lesion precluded the assessment of NNLS spectra as potential clinical biomarker.

Regardless, the expansion from a single or fixed-term exponential analysis to a full spectrum provided by NNLS allows for a much more thorough characterisation of the diffusion processes and, consequently, of the underlying microstructure. It was demonstrated that, despite the increased complexity in the number of free parameters, the NNLS approach explains the measured signal better than both the conventional mono-exponential, and the extended bi- and tri-exponential decays. The compartmentalisation of the NNLS spectra lead to the identification of diffusivity ranges which are shown to be specific to the normal appearing tissues and agree with the literature (Mulkern et al., 1999; Clark and Le Bihan, 2000; Mulkern et al., 2001; Zeng et al., 2018), further validating the method.

The multi-parametric approaches suggested in this work are far from being the single ones which can be of value in clinical practice. As an outlook, it would be of interest to explore the value of TE dependence in the obtained signal. As hinted at in 2.3.1, one can tailor a diffusion-weighted sequence to be measured at multiple TE's, allowing the estimation of T_2 - demonstrated in Annex B. This in turn has been shown to provide relevant information towards distinguishing tumour entities (Eis et al., 1995; Sun et al., 2004; Oh et al., 2005). An additional avenue includes the study of water exchange rates. Water exchange between intra- and extra-cellular spaces is an important feature of cell metabolism (Dix and Solomon, 1984). Pathologies like brain tumours have been shown to alter the exchange rate of water between these two compartments by expressing aquaporin channels (Hu and Verkman, 2006; Papadopoulos et al., 2008; Ruggiero et al., 2022). Imaging exchange rates, using techniques like the one proposed by Lasič et al. (2011) or by Springer Jr et al. (2023a,b), can therefore present with important biomarkers relating to tumour malignancy.

In conclusion, two methods for the analysis of multi-b-value dMRI signal were developed with the goal of providing a dMRI framework for multi-parametric assessment of pathological tissue. These methods were demonstrated here in brain tumours, although other pathologies might also benefit from them.

Bibliography

Aboian, M. S., Solomon, D. A., Felton, E., Mabray, M. C., Villanueva-Meyer, J. E., Mueller, S., and Cha, S. Imaging characteristics of pediatric diffuse midline gliomas with histone H3 K27M mutation. *AJNR. American journal of neuroradiology*, 38:795–800, Apr 2017.

Akaike, H. Information theory and an extension of the maximum likelihood principle. In Parzen, E., Tanabe, K., and Kitagawa, G., editors, *Selected Papers of Hirotugu Akaike*, pages 199–213. Springer New York, New York, NY, 1998. doi: 10.1007/978-1-4612-1694-0_15. URL https://doi.org/10.1007/978-1-4612-1694-0_15.

Alexander, A. L., Hasan, K. M., Lazar, M., Tsuruda, J. S., and Parker, D. L. Analysis of partial volume effects in diffusion-tensor MRI. *Magn. Reson. Med.*, 45(5):770–780, May 2001. ISSN 0740-3194. doi: 10.1002/mrm.1105. URL https://doi.org/10.1002/mrm.1105.

Alonso-Ortiz, E., Levesque, I. R., and Pike, G. B. Multi-gradient-echo myelin water fraction imaging: Comparison to the multi-echo-spin-echo technique. *Magnetic resonance in medicine*, 79:1439–1446, Mar 2018.

Andersson, J. L. R. and Sotiropoulos, S. N. An integrated approach to correction for off-resonance effects and subject movement in diffusion MR imaging. *NeuroImage*, 125:1063–1078, 2016. ISSN 1053-8119. doi: 10.1016/j.neuroimage.2015.10.019. URL https://www.sciencedirect.com/science/article/pii/S1053811915009209.

Andersson, J. L. R., Skare, S., and Ashburner, J. How to correct susceptibility distortions in spin-echo echo-planar images: application to diffusion tensor imaging. *NeuroImage*, 20(2):870–888, 2003. ISSN 1053-8119. doi: 10.1016/S1053-8119(03)00336-7. URL https://www.sciencedirect.com/science/article/pii/S1053811903003367.

Ashburner, J. and Friston, K. J. Unified segmentation. *NeuroImage*, 26(3):839–851, 2005. ISSN 1053-8119. doi: 10.1016/j.neuroimage.2005.02.018. URL https://www.sciencedirect.com/science/article/pii/S1053811905001102.

Assaf, Y. and Cohen, Y. Detection of different water populations in brain tissue using 2H single- and double-quantum-filtered diffusion NMR spectroscopy. *Journal of magnetic resonance. Series B*, 112:151–9, Aug 1996.

Barajas, R. F. J., Hess, C. P., Phillips, J. J., Von Morze, C. J., Yu, J. P., Chang, S. M., Nelson, S. J., McDermott, M. W., Berger, M. S., and Cha, S. Super-resolution track density imaging of glioblastoma: histopathologic correlation. *AJNR. American journal of neuroradiology*, 34:1319–25, Jul 2013.

Becherer, A., Karanikas, G., Szabó, M., Zettinig, G., Asenbaum, S., Marosi, C., Henk, C., Wunderbaldinger, P., Czech, T., Wadsak, W., and Kletter, K. Brain tumour imaging with pet: a comparison between [18F]fluorodopa and [11C]methionine. *European Journal of Nuclear Medicine and Molecular Imaging*, 30(11):1561–1567, 2003. ISSN 1619-7089. doi: 10.1007/s00259-003-1259-1. URL https://doi.org/10.1007/s00259-003-1259-1.

Bernstein, M. A., Thomasson, D. M., and Perman, W. H. Improved detectability in low signal-to-noise ratio magnetic resonance images by means of a phase-corrected real reconstruction. *Med. Phys.*, 16(5):813–817, September 1989. ISSN 0094-2405. doi: 10.1118/1.596304. URL https://doi.org/10.1118/1.596304.

Bisdas, S., Koh, T. S., Roder, C., Braun, C., Schittenhelm, J., Ernemann, U., and Klose, U. Intravoxel incoherent motion diffusion-weighted MR imaging of gliomas: feasibility of the method and initial results. *Neuroradiology*, 55(10):1189–1196, 2013. ISSN 1432-1920. doi: 10.1007/s00234-013-1229-7. URL https://doi.org/10.1007/s00234-013-1229-7.

Bloch, F. Nuclear induction. *PR*, 70(7-8):460–474, October 1946. doi: 10.1103/PhysRev.70.460. URL https://link.aps.org/doi/10.1103/PhysRev.70.460.

Brandsma, D., Stalpers, L., Taal, W., Sminia, P., and van den Bent, M. J. Clinical features, mechanisms, and management of pseudoprogression in malignant gliomas. *The Lancet Oncology*, 9(5):453–461, May 2008. ISSN 1470-2045. doi: 10.1016/S1470-2045(08)70125-6. URL https://doi.org/10.1016/S1470-2045(08)70125-6.

Busch, H., Davis, J. R., Honig, G. R., Anderson, D. C., Nair, P. V., and Nyhan, W. L. The uptake of a variety of amino acids into nuclear proteins of tumors and other tissues. *Cancer Res*, 19(10):1030–1039, November 1959. ISSN 0008-5472.

Bydder, M. and Du, J. Noise reduction in multiple-echo data sets using singular value decomposition. *Magnetic Resonance Imaging*, 24(7):849–856, 2006. ISSN 0730-725X. doi: 10.1016/j.mri.2006.03.006. URL https://www.sciencedirect.com/science/article/pii/S0730725X06001317.

Bähr, O., Harter, P. N., Weise, L. M., You, S.-J., Mittelbronn, M., Ronellenfitsch, M. W., Rieger, J., Steinbach, J. P., and Hattingen, E. Sustained focal antitumor activity of bevacizumab in recurrent glioblastoma. *Neurology*, 83(3):227, July 2014. doi: 10.1212/WNL.0000000000000594. URL http://n.neurology.org/content/83/3/227.abstract.

Caldeira, L. L., Seong Dae, Y., da Silva, N. A., Filss, C., and Shah, N. J. Dynamic susceptibility contrast parametric imaging using accelerated dual-contrast echo planar imaging with keyhole. *J. Magn. Reson. Imaging*, 50(2):628–640, August 2019. ISSN 1053-1807. doi: 10.1002/jmri.26639. URL https://doi.org/10.1002/jmri.26639.

Canales-Rodríguez, E. J., Pizzolato, M., Piredda, G. F., Hilbert, T., Kunz, N., Pot, C., Yu, T., Salvador, R., Pomarol-Clotet, E., Kober, T., Thiran, J.-P., and Daducci, A. Comparison of non-parametric T2 relaxometry methods for myelin water quantification. *Medical Image Analysis*, 69:101959, 2021. ISSN 1361-8415. doi: 10.1016/j.media.2021.101959. URL https://www.sciencedirect.com/science/article/pii/S1361841521000050.

Chen, W. Clinical applications of PET in brain tumors. *J Nucl Med*, 48(9):1468, September 2007. doi: 10.2967/jnumed.106.037689. URL http://jnm.snmjournals.org/content/48/9/1468.abstract.

Chou, M., Kao, E., and Mori, S. Effects of b-value and echo time on magnetic resonance diffusion tensor imaging-derived parameters at 1.5 T: A voxel-wise study. *Journal of Medicine and Biological Engineering*, 33(1):45–50, 2012. doi: 10.5405/jmbe.1126.

Chu, H. H., Choi, S. H., Ryoo, I., Kim, S. C., Yeom, J. A., Shin, H., Jung, S. C., Lee, A. L., Yoon, T. J., Kim, T. M., Lee, S.-H., Park, C.-K., Kim, J.-H., Sohn, C.-H., Park, S.-H., and Kim, I. H. Differentiation of true progression from pseudoprogression in glioblastoma treated with radiation therapy and concomitant temozolomide: Comparison study of standard and high-b-value diffusion-weighted imaging. *Radiology*, 269(3):831–840, December 2013. ISSN 0033-8419. doi: 10.1148/radiol.13122024. URL https://doi.org/10.1148/radiol.13122024.

Clark, C. A. and Le Bihan, D. Water diffusion compartmentation and anisotropy at high b values in the human brain. *Magn. Reson. Med.*, 44(6):852–859, December 2000. ISSN 0740-3194. URL https://doi.org/10.1002/1522-2594(200012)44:6<852::AID-MRM5>3.0.CO;2-A.

Cordero-Grande, L., Christiaens, D., Hutter, J., Price, A. N., and Hajnal, J. V. Complex diffusion-weighted image estimation via matrix recovery under general noise models. *NeuroImage*, 200:391–404, Oct 2019.

Craigie, E. H. The architecture of the cerebral capillary bed. *Biological Reviews*, 20(4):133–146, October 1945. ISSN 1464-7931. doi: 10.1111/j.1469-185X.1945.tb00446.x. URL https://doi.org/10.1111/j.1469-185X.1945.tb00446.x.

da Silva, N. A., Lohmann, P., Fairney, J., Magill, A. W., Oros Peusquens, A.-M., Choi, C.-H., Stirnberg, R., Stoffels, G., Galldiks, N., Golay, X., Langen, K.-J., and Jon Shah, N. Hybrid MR-PET of brain tumours using amino acid PET and chemical exchange saturation transfer MRI. *European Journal of Nuclear Medicine and Molecular Imaging*, 45(6):1031–1040, 2018. ISSN 1619-7089. doi: 10.1007/s00259-018-3940-4. URL https://doi.org/10.1007/s00259-018-3940-4.

Dagogo-Jack, I. and Shaw, A. T. Tumour heterogeneity and resistance to cancer therapies. *Nature Reviews Clinical Oncology*, 15(2):81–94, 2018. ISSN 1759-4782. doi: 10.1038/nrclinonc.2017.166. URL https://doi.org/10.1038/nrclinonc.2017.166.

De Luca, A., Leemans, A., Bertoldo, A., Arrigoni, F., and Froeling, M. A robust deconvolution method to disentangle multiple water pools in diffusion MRI. *NMR in biomedicine*, 31:e3965, Nov 2018.

de Wit, M. C. Y., de Bruin, H. G., Eijkenboom, W., Sillevis Smitt, P. A. E., and van den Bent, M. J. Immediate post-radiotherapy changes in malignant glioma can mimic tumor progression. *Neurology*, 63:535–7, Aug 2004.

De Witte, O., Levivier, M., Violon, P., Salmon, I., Damhaut, P., Wikler, D. l., Hildebrand, J., Brotchi, J., and Goldman, S. Prognostic value of positron emission tomography with [18F]Fluoro-2-deoxy-D-glucose in the low-grade glioma. *Neurosurgery*, 39(3), 1996. ISSN 0148-396X. URL https://journals.lww.com/neurosurgery/Fulltext/1996/09000/Prognostic_Value_of_Positron_Emission_Tomography.7.aspx.

Delbeke, D., Meyerowitz, C., Lapidus, R. L., Maciunas, R. J., Jennings, M. T., Moots, P. L., and Kessler, R. M. Optimal cutoff levels of F-18 fluorodeoxyglucose uptake in the differentiation of low-grade from high-grade brain tumors with PET. *Radiology*, 195(1):47–52, April 1995. ISSN 0033-8419. doi: 10.1148/radiology.195.1.7892494. URL https://doi.org/10.1148/radiology.195.1.7892494.

Dix, J. A. and Solomon, A. K. Role of membrane proteins and lipids in water diffusion across red cell membranes. *Biochimica et biophysica acta*, 773:219–30, Jun 1984.

Duffau, H. and Taillandier, L. New concepts in the management of diffuse low-grade glioma: Proposal of a multistage and individualized therapeutic approach. *Neuro-oncology*, 17:332–42, Mar 2015.

Einstein, A. Über die von der molekularkinetischen Theorie der Wärme geforderte Bewegung von in ruhenden Flüssigkeiten suspendierten Teilchen. *Ann. Phys.*, 322(8):549–560, January 1905. ISSN 0003-3804. doi: 10.1002/andp.19053220806. URL https://doi.org/10.1002/andp.19053220806.

Eis, M., Els, T., and Hoehn-Berlage, M. High resolution quantitative relaxation and diffusion mri of three different experimental brain tumors in rat. *Magn. Reson. Med.*, 34(6):835–844, December 1995. ISSN 0740-3194. doi: 10.1002/mrm.1910340608. URL https://doi.org/10.1002/mrm.1910340608.

Ellingson, B. M., Bendszus, M., Boxerman, J., Barboriak, D., Erickson, B. J., Smits, M., Nelson, S. J., Gerstner, E., Alexander, B., Goldmacher, G., Wick, W., Vogelbaum, M., Weller, M., Galanis, E., Kalpathy-Cramer, J., Shankar, L., Jacobs, P., Pope, W. B., Yang, D., Chung, C., Knopp, M. V., Cha, S., van den Bent, M. J., Chang, S., Yung, W. K. A., Cloughesy, T. F., Wen, P. Y., and Gilbert, M. R. Consensus recommendations for a standardized brain tumor imaging protocol in clinical trials. *Neuro-oncology*, 17:1188–98, Sep 2015.

Farid, N., Almeida-Freitas, D., White, N., McDonald, C., Muller, K., VandenBerg, S., Kesari, S., and Dale, A. Restriction-spectrum imaging of bevacizumab-related necrosis in a patient with GBM, 2013. URL https://www.frontiersin.org/articles/10.3389/fonc.2013.00258.

Federau, C., Meuli, R., K., OBrien, Maeder, P., and Hagmann, P. Perfusion measurement in brain gliomas with intravoxel incoherent motion MRI. *Am. J. Neuroradiol.*, 35(2):256, February 2014a. doi: 10.3174/ajnr.A3686. URL http://www.ajnr.org/content/35/2/256.abstract.

Federau, C. Intravoxel incoherent motion MRI as a means to measure in vivo perfusion: A review of the evidence. *NMR in Biomedicine*, 30(11):e3780, November 2017. ISSN 0952-3480. doi: 10.1002/nbm.3780. URL https://doi.org/10.1002/nbm.3780.

Federau, C., Maeder, P., O'Brien, K., Browaeys, P., Meuli, R., and Hagmann, P. Quantitative measurement of brain perfusion with intravoxel incoherent motion MR imaging. *Radiology*, 265(3):874–881, December 2012. ISSN 0033-8419. doi: 10.1148/radiol.12120584. URL https://doi.org/10.1148/radiol.12120584.

Federau, C., O'Brien, K., Meuli, R., Hagmann, P., and Maeder, P. Measuring brain perfusion with intravoxel incoherent motion (IVIM): Initial clinical experience. *J. Magn. Reson. Imaging*, 39(3):624–632, March 2014b. ISSN 1053-1807. doi: 10.1002/jmri.24195. URL https://doi.org/10.1002/jmri.24195.

Feng, Z., Min, X., Wang, L., Yan, X., Li, B., Ke, Z., Zhang, P., and You, H. Effects of echo time on IVIM quantification of the normal prostate. *Scientific Reports*, 8(1):2572, 2018. ISSN 2045-2322. doi: 10.1038/s41598-018-19150-2. URL https://doi.org/10.1038/s41598-018-19150-2.

Gerstner, E. R., Frosch, M. P., and Batchelor, T. T. Diffusion magnetic resonance imaging detects pathologically confirmed, nonenhancing tumor progression in a patient with recurrent glioblastoma receiving bevacizumab. *Journal of clinical oncology : official journal of the American Society of Clinical Oncology*, 28:e91–3, Feb 2010.

Ginsberg, L. E., Fuller, G. N., Hashmi, M., Leeds, N. E., and Schomer, D. F. The significance of lack of MR contrast enhancement of supratentorial brain tumors in adults: histopathological evaluation of a series. *Surgical neurology*, 49:436–40, Apr 1998.

Goldbrunner, R. H., Bernstein, J. J., and Tonn, J.-C. ECM-mediated glioma cell invasion. *Microsc. Res. Tech.*, 43 (3):250–257, November 1998. ISSN 1059-910X. URL https://doi.org/10.1002/(SICI)1097-0029(19981101)43:3<250::AID-JEMT7>3.0.CO;2-C.

Goldman, S., Levivier, M., Pirotte, B., Brucher, J.-M., Wikler, D., Damhaut, P., Dethy, S., Brotchi, J., and Hildebrand, J. Regional methionine and glucose uptake in high-grade gliomas: A comparative study on PET-guided stereotactic biopsy. *J Nucl Med*, 38(9):1459, September 1997. URL http://jnm.snmjournals.org/content/38/9/1459.abstract.

Goyal, P., Tenenbaum, M., Gupta, S., Kochar, P. S., Bhatt, A. A., Mangla, M., Kumar, Y., and Mangla, R. Survival prediction based on qualitative MRI diffusion signature in patients with recurrent high grade glioma treated with bevacizumab. *Quantitative Imaging in Medicine and Surgery; Vol 8, No 3 (April 30, 2018): Quantitative Imaging in Medicine and Surgery*, 2018. URL https://qims.amegroups.org/article/view/19278.

Graham, M. S., Drobnjak, I., and Zhang, H. Realistic simulation of artefacts in diffusion MRI for validating post-processing correction techniques. *NeuroImage*, 125:1079–1094, 2016. ISSN 1053-8119. doi: 10.1016/j.neuroimage.2015.11.006. URL https://www.sciencedirect.com/science/article/pii/S1053811915010289.

Graham, S. J., Stanchev, P. L., and Bronskill, M. J. Criteria for analysis of multicomponent tissue T2 relaxation data. *Magn. Reson. Med.*, 35(3):370–378, March 1996. ISSN 0740-3194. doi: 10.1002/mrm.1910350315. URL https://doi.org/10.1002/mrm.1910350315.

Griffiths, D. J. and Schroeter, D. F. *Introduction to Quantum Mechanics*. Cambridge University Press, Cambridge, 3 edition, 2018. doi: 10.1017/9781316995433. URL https://www.cambridge.org/core/books/introduction-to-quantum-mechanics/990799CA07A83FC5312402AF6860311E.

Gupta, A., Young, R. J., Karimi, S., Sood, S., Zhang, Z., Mo, Q., Gutin, P. H., Holodny, A. I., and Lassman, A. B. Isolated diffusion restriction precedes the development of enhancing tumor in a subset of patients with glioblastoma. *AJNR. American journal of neuroradiology*, 32:1301–1306, Aug 2011.

Hahn, E. L. Nuclear induction due to free larmor precession. *PR*, 77(2):297–298, January 1950a. doi: 10.1103/PhysRev.77.297.2. URL https://link.aps.org/doi/10.1103/PhysRev.77.297.2.

Hahn, E. L. Spin echoes. *PR*, 80(4):580–594, November 1950b. doi: 10.1103/PhysRev.80.580. URL https://link.aps.org/doi/10.1103/PhysRev.80.580.

Haining, Z., Kawai, N., Miyake, K., Okada, M., Okubo, S., Zhang, X., Fei, Z., and Tamiya, T. Relation of LAT1/4F2hc expression with pathological grade, proliferation and angiogenesis in human gliomas. *BMC clinical pathology*, 12:4, Feb 2012.

Hamacher, K. and Coenen, H. H. Efficient routine production of the 18f-labelled amino acid O-(2-[18F]fluoroethyl)-l-tyrosine. *Applied Radiation and Isotopes*, 57(6):853–856, 2002. ISSN 0969-8043. doi: 10.1016/S0969-8043(02)00225-7. URL https://www.sciencedirect.com/science/article/pii/S0969804302002257.

Han, C., Huang, S., Guo, J., Zhuang, X., and Han, H. Use of a high b-value for diffusion weighted imaging of peritumoral regions to differentiate high-grade gliomas and solitary metastases. *Journal of magnetic resonance imaging : JMRI*, 42:80–6, Jul 2015.

Hansen, B., Lund, T. E., Sangill, R., and Jespersen, S. N. Experimentally and computationally fast method for estimation of a mean kurtosis. *Magn Reson Med*, 69(6):1754–1760, June 2013. ISSN 0740-3194. doi: 10.1002/mrm.24743. URL https://doi.org/10.1002/mrm.24743.

Hansen, B., Lund, T. E., Sangill, R., Stubbe, E., Finsterbusch, J., and Jespersen, S. N. Experimental considerations for fast kurtosis imaging. *Magn. Reson. Med.*, 76(5):1455–1468, November 2016. ISSN 0740-3194. doi: 10.1002/mrm.26055. URL https://doi.org/10.1002/mrm.26055.

Hansen, P. C. Analysis of discrete ill-posed problems by means of the L-curve. *SIAM Rev.*, 34(4):561–580, December 1992. ISSN 0036-1445. doi: 10.1137/1034115. URL https://doi.org/10.1137/1034115.

Hattingen, E. and Pilatus, U. *Brain Tumor Imaging*. Springer Berlin, Heidelberg, 1 edition, 2016. ISBN 978-3-642-45039-6. doi: https://doi.org/10.1007/978-3-642-45040-2.

Herholz, K., Langen, K.-J., Schiepers, C., and Mountz, J. M. Brain tumors. *Seminars in nuclear medicine*, 42:356–70, Nov 2012.

Herzog, H., Langen, K.-J., Weirich, C., Rota Kops, E., Kaffanke, J., Tellmann, L., Scheins, J., Neuner, I., Stoffels, G., Fischer, K., Caldeira, L., Coenen, H. H., and Shah, N. J. High resolution BrainPET combined with simultaneous MRI. *Nuklearmedizin - NuclearMedicine*, 50(02):74–82, 2011. ISSN 2567-6407. doi: 10.3413/Nukmed-0347-10-09. URL http://www.thieme-connect.com/products/ejournals/abstract/10.3413/Nukmed-0347-10-09.

Higano, S., Yun, X., Kumabe, T., Watanabe, M., Mugikura, S., Umetsu, A., Sato, A., Yamada, T., and Takahashi, S. Malignant astrocytic tumors: Clinical importance of apparent diffusion coefficient in prediction of grade and prognosis. *Radiology*, 241(3):839–846, December 2006. ISSN 0033-8419. doi: 10.1148/radiol.2413051276. URL https://doi.org/10.1148/radiol.2413051276.

Hu, J. and Verkman, A. S. Increased migration and metastatic potential of tumor cells expressing aquaporin water channels. *FASEB journal : official publication of the Federation of American Societies for Experimental Biology*, 20:1892–4, Sep 2006.

Hu, X., Wong, K. K., Young, G. S., Guo, L., and Wong, S. T. Support vector machine multiparametric MRI identification of pseudoprogression from tumor recurrence in patients with resected glioblastoma. *J. Magn. Reson. Imaging*, 33(2):296–305, February 2011. ISSN 1053-1807. doi: 10.1002/jmri.22432. URL https://doi.org/10.1002/jmri.22432.

Huber, T., Bette, S., Wiestler, B., Gempt, J., Gerhardt, J., Delbridge, C., Barz, M., Meyer, B., Zimmer, C., and Kirschke, J. S. Fractional anisotropy correlates with overall survival in glioblastoma. *World Neurosurgery*, 95:525–534.e1, 2016. ISSN 1878-8750. doi: 10.1016/j.wneu.2016.08.055. URL https://www.sciencedirect.com/science/article/pii/S1878875016307227.

Iima, M., Reynaud, O., Tsurugizawa, T., Ciobanu, L., Li, J.-R., Geffroy, F., Djemai, B., Umehana, M., and Le Bihan, D. Characterization of glioma microcirculation and tissue features using intravoxel incoherent motion magnetic resonance imaging in a rat brain model. *Investigative Radiology*, 49(7), 2014. ISSN 0020-9996. URL https://journals.lww.com/investigativeradiology/Fulltext/2014/07000/Characterization_of_Glioma_Microcirculation_and.6.aspx.

Iima, M., Yano, K., Kataoka, M., Umehana, M., Murata, K., Kanao, S., Togashi, K., and Le Bihan, D. Quantitative non-Gaussian diffusion and intravoxel incoherent motion magnetic resonance imaging: Differentiation of malignant and benign breast lesions. *Investigative Radiology*, 50(4), 2015. ISSN 0020-9996. URL https://journals.lww.com/investigativeradiology/Fulltext/2015/04000/Quantitative_Non_Gaussian_Diffusion_and_Intravoxel.4.aspx.

Irfanoglu, M. O., Nayak, A., Jenkins, J., and Pierpaoli, C. TORTOISEv3: Improvements and new features of the NIH diffusion MRI processing pipeline. In *Proceedings of International Society of Magnetic Resonance in Medicine*, abstract nr. 3540, 2017.

Irfanoglu, M. O., Modi, P., Nayak, A., Hutchinson, E. B., Sarlls, J., and Pierpaoli, C. DR-BUDDI (diffeomorphic registration for blip-up blip-down diffusion imaging) method for correcting echo planar imaging distortions. *NeuroImage*, 106:284–299, 2015. ISSN 1053-8119. doi: 10.1016/j.neuroimage.2014.11.042. URL https://www.sciencedirect.com/science/article/pii/S1053811914009598.

Isselbacher, K. J. Sugar and amino acid transport by cells in culture – differences between normal and malignant cells. *N Engl J Med*, 286(17):929–933, April 1972. ISSN 0028-4793. doi: 10.1056/NEJM197204272861707. URL https://doi.org/10.1056/NEJM197204272861707.

Jacobs, M. A., Mitsias, P., Soltanian-Zadeh, H., Santhakumar, S., Ghanei, A., Hammond, R., Peck, D. J., Chopp, M., and Patel, S. Multiparametric MRI tissue characterization in clinical stroke with correlation to clinical outcome. *Stroke*, 32(4):950–957, April 2001. doi: 10.1161/01.STR.32.4.950. URL https://doi.org/10.1161/01.STR.32.4.950.

Jager, P. L., Vaalburg, W., Pruim, J., de Vries, E. G. E., Langen, K.-J., and Piers, D. A. Radiolabeled amino acids: Basic aspects and clinical applications in oncology. *J Nucl Med*, 42(3):432, March 2001. URL http://jnm.snmjournals.org/content/42/3/432.abstract.

Jain, R. K., di Tomaso, E., Duda, D. G., Loeffler, J. S., Sorensen, A. G., and Batchelor, T. T. Angiogenesis in brain tumours. *Nature reviews. Neuroscience*, 8:610–22, Aug 2007. doi: doi:10.1038/nrn2175.

Jensen, J. H. and Helpern, J. A. MRI quantification of non-gaussian water diffusion by kurtosis analysis. *NMR in biomedicine*, 23:698–710, Aug 2010. doi: doi:10.1002/nbm.1518.

Jensen, J. H., Helpern, J. A., Ramani, A., Lu, H., and Kaczynski, K. Diffusional kurtosis imaging: The quantification of non-Gaussian water diffusion by means of magnetic resonance imaging. *Magnetic Resonance in Medicine*, 53(6):1432–1440, 2005. doi: https://doi.org/10.1002/mrm.20508. URL https://onlinelibrary.wiley.com/doi/abs/10.1002/mrm.20508.

Jiang, R., Jiang, J., Zhao, L., Zhang, J., Zhang, S., Yao, Y., Yang, S., Shi, J., Shen, N., Su, C., Zhang, J., and Zhu, W. Diffusion kurtosis imaging can efficiently assess the glioma grade and cellular proliferation. *Oncotarget*, 6:42380–93, Dec 2015. doi: doi:10.18632/oncotarget.5675.

Jolliffe, I. T. *Principle Component Analysis*. Springer New York, NY, 2 edition, 2002. ISBN 978-0-387-95442-4. doi: https://doi.org/10.1007/b98835.

Jones, D. K. The effect of gradient sampling schemes on measures derived from diffusion tensor MRI: A monte carlo study†. *Magn. Reson. Med.*, 51(4):807–815, April 2004. ISSN 0740-3194. doi: 10.1002/mrm.20033. URL https://doi.org/10.1002/mrm.20033.

Jütten, K., Mainz, V., Gauggel, S., Patel, H. J., Binkofski, F., Wiesmann, M., Clusmann, H., and Na, C.-H. Diffusion tensor imaging reveals microstructural heterogeneity of normal-appearing white matter and related cognitive dysfunction in glioma patients. *Frontiers in oncology*, 9:536, 2019.

Kang, Y., Choi, S. H., Kim, Y.-J., Kim, K. G., Sohn, C.-H., Kim, J.-H., Yun, T. J., and Chang, K.-H. Gliomas: Histogram analysis of apparent diffusion coefficient maps with standard- or high-b-value diffusion-weighted MR imaging–correlation with tumor grade. *Radiology*, 261(3):882–890, December 2011. ISSN 0033-8419. doi: 10.1148/radiol.11110686. URL https://doi.org/10.1148/radiol.11110686.

Kaschten, B., Stevenaert, A., Sadzot, B., Deprez, M., Degueldre, C., Fiore, G. D., Luxen, A., and Reznik, M. Preoperative evaluation of 54 gliomas by PET with fluorine-18-fluorodeoxyglucose and/or carbon-11- methionine. *J Nucl Med*, 39(5):778, May 1998. URL http://jnm.snmjournals.org/content/39/5/778.abstract.

Keil, V. C., Mädler, B., Gielen, G. H., Pintea, B., Hiththetiya, K., Gaspranova, A. R., Gieseke, J., Simon, M., Schild, H. H., and Hadizadeh, D. R. Intravoxel incoherent motion MRI in the brain: Impact of the fitting model on perfusion fraction and lesion differentiability. *J. Magn. Reson. Imaging*, 46(4):1187–1199, October 2017. ISSN 1053-1807. doi: 10.1002/jmri.25615. URL https://doi.org/10.1002/jmri.25615.

Kiselev, V. G. and Il'yasov, K. A. Is the "biexponential diffusion" biexponential? *Magn. Reson. Med.*, 57(3):464–469, March 2007. ISSN 0740-3194. doi: 10.1002/mrm.21164. URL https://doi.org/10.1002/mrm.21164.

Kistler, M., Bonaretti, S., Pfahrer, M., Niklaus, R., and Büchler, P. The virtual skeleton database: An open access repository for biomedical research and collaboration, 2013. ISSN 14388871. URL http://www.ncbi.nlm.nih.gov/pubmed/24220210.

Kothari, P. D., White, N. S., Farid, N., Chung, R., Kuperman, J. M., Girard, H. M., Shankaranarayanan, A., Kesari, S., McDonald, C. R., and Dale, A. M. Longitudinal restriction spectrum imaging is resistant to pseudoresponse in patients with high-grade gliomas treated with bevacizumab. *Am. J. Neuroradiol.*, 34(9):1752, September 2013. doi: 10.3174/ajnr.A3506. URL http://www.ajnr.org/content/34/9/1752.abstract.

Kroeker, R. M. and Henkelman, R. M. Analysis of biological NMR relaxation data with continuous distributions of relaxation times. *Journal of Magnetic Resonance (1969)*, 69(2):218–235, 1986. ISSN 0022-2364. doi: 10.1016/0022-2364(86)90074-0. URL https://www.sciencedirect.com/science/article/pii/0022236486900740.

Kurokawa, R., Hagiwara, A., Kurokawa, M., Ellingson, B. M., Baba, A., and Moritani, T. Diffusion histogram profiles predict molecular features of grade 4 in histologically lower-grade adult diffuse gliomas following WHO classification 2021. *European Radiology*, 2023. ISSN 1432-1084. doi: 10.1007/s00330-023-10071-x. URL https://doi.org/10.1007/s00330-023-10071-x.

Kärger, J. Nmr self-diffusion studies in heterogeneous systems. *Advances in Colloid and Interface Science*, 23:129–148, 1985. ISSN 0001-8686. doi: https://doi.org/10.1016/0001-8686(85)80018-X. URL https://www.sciencedirect.com/science/article/pii/000186868580018X.

Lagarias, J. C., Reeds, J. A., Wright, M. H., and Wright, P. E. Convergence properties of the Nelder-Mead simplex method in low dimensions. *SIAM Journal on Optimization*, 9(1):112–147, 1998. ISSN 1052-6234. doi: 10.1137/S1052623496303470. URL http://www.scopus.com/inward/citedby.url?scp=0032251894&partnerID=8YFLogxK.

Langen, K.-J., Jarosch, M., Mühlensiepen, H., Hamacher, K., Bröer, S., Jansen, P., Zilles, K., and Coenen, H. H. Comparison of fluorotyrosines and methionine uptake in F98 rat gliomas. *Nuclear medicine and biology*, 30:501–8, Jul 2003.

Langleben, D. D. and Segall, G. M. PET in differentiation of recurrent brain tumor from radiation injury. *J Nucl Med*, 41(11):1861, November 2000. URL http://jnm.snmjournals.org/content/41/11/1861.abstract.

Lanzafame, S., Giannelli, M., Garaci, F., Floris, R., Duggento, A., Guerrisi, M., and Toschi, N. Differences in Gaussian diffusion tensor imaging and non-Gaussian diffusion kurtosis imaging model-based estimates of diffusion tensor invariants in the human brain. *Med. Phys.*, 43(5):2464–2475, May 2016. ISSN 0094-2405. doi: 10.1118/1.4946819. URL https://doi.org/10.1118/1.4946819.

Lasič, S., Nilsson, M., Lätt, J., Ståhlberg, F., and Topgaard, D. Apparent exchange rate mapping with diffusion MRI. *Magn. Reson. Med.*, 66(2):356–365, August 2011. ISSN 0740-3194. doi: 10.1002/mrm.22782. URL https://doi.org/10.1002/mrm.22782.

LaViolette, P. S., Mickevicius, N. J., Cochran, E. J., Rand, S. D., Connelly, J., Bovi, J. A., Malkin, M. G., Mueller, W. M., and Schmainda, K. M. Precise ex vivo histological validation of heightened cellularity and diffusion-restricted necrosis in regions of dark apparent diffusion coefficient in 7 cases of high-grade glioma. *Neuro-oncology*, 16:1599–606, Dec 2014.

Le Bihan, D. and Brenton, E. Imagerie de diffusion in-vivo par résonance magnétique nucléaire. *Comptes-Rendus de l'Académie des Sciences*, 93(5):27-34, 1985.

Le Bihan, D., Breton, E., Lallemand, D., Grenier, P., Cabanis, E., and Laval-Jeantet, M. MR imaging of intravoxel incoherent motions: application to diffusion and perfusion in neurologic disorders. *Radiology*, 161:401–7, Nov 1986.

Le Bihan, D., Breton, E., Lallemand, D., Aubin, M. L., Vignaud, J., and Laval-Jeantet, M. Separation of diffusion and perfusion in intravoxel incoherent motion MR imaging. *Radiology*, 168(2):497–505, 1988. doi: 10.1148/radiology.168.2.3393671. URL https://doi.org/10.1148/radiology.168.2.3393671. PMID: 3393671.

Le Bihan, D. and Turner, R. The capillary network: a link between ivim and classical perfusion. *Magn. Reson. Med.*, 27(1):171–178, September 1992. ISSN 0740-3194. doi: 10.1002/mrm.1910270116. URL https://doi.org/10.1002/mrm.1910270116.

Le Rhun, E., Taillibert, S., and Chamberlain, M. C. Current management of adult diffuse infiltrative low grade gliomas. *Current neurology and neuroscience reports*, 16:15, Feb 2016.

Lebel, C., Walker, L., Leemans, A., Phillips, L., and Beaulieu, C. Microstructural maturation of the human brain from childhood to adulthood. *NeuroImage*, 40:1044–55, Apr 2008.

Leigh, R., Knutsson, L., Zhou, J., and van Zijl, P. C. Imaging the physiological evolution of the ischemic penumbra in acute ischemic stroke. *Journal of cerebral blood flow and metabolism : official journal of the International Society of Cerebral Blood Flow and Metabolism*, 38:1500–1516, Sep 2018.

Lengauer, C., Kinzler, K. W., and Vogelstein, B. Genetic instabilities in human cancers. *Nature*, 396(6712):643–649, 1998. ISSN 1476-4687. doi: 10.1038/25292. URL `https://doi.org/10.1038/25292`.

Leu, K., Boxerman, J. L., Lai, A., Nghiemphu, P. L., Pope, W. B., Cloughesy, T. F., and Ellingson, B. M. Bidirectional contrast agent leakage correction of dynamic susceptibility contrast (DSC)-MRI improves cerebral blood volume estimation and survival prediction in recurrent glioblastoma treated with bevacizumab. *J. Magn. Reson. Imaging*, 44(5):1229–1237, November 2016. ISSN 1053-1807. doi: 10.1002/jmri.25227. URL `https://doi.org/10.1002/jmri.25227`.

Levitt, M. *Spin Dynamics: Basics of Nuclear Magnetic Resonance*. Wiley, 2013. ISBN 9781118681848. URL `https://books.google.de/books?id=bysFAa4MPQcC`.

Li, C., Wang, S., Yan, J.-L., Torheim, T., Boonzaier, N. R., Sinha, R., Matys, T., Markowetz, F., and Price, S. J. Characterizing tumor invasiveness of glioblastoma using multiparametric magnetic resonance imaging. *Journal of Neurosurgery JNS*, 132(5):1465–1472, 2020. doi: 10.3171/2018.12.JNS182926. URL `https://thejns.org/view/journals/j-neurosurg/132/5/article-p1465.xml`.

Liang, Z. P., Lauterbur, P. C., in Medicine, I. E., and Society, B. *Principles of Magnetic Resonance Imaging: A Signal Processing Perspective*. SPIE Optical Engineering Press, 2000. URL `https://books.google.de/books?id=sRyEQgAACAAJ`.

Livne, M., Kossen, T., Madai, V. I., Zaro-Weber, O., Moeller-Hartmann, W., Mouridsen, K., Heiss, W.-D., and Sobesky, J. Multiparametric model for penumbral flow prediction in acute stroke. *Stroke*, 48(7):1849–1854, July 2017. doi: 10.1161/STROKEAHA.117.016631. URL `https://doi.org/10.1161/STROKEAHA.117.016631`.

Louis, D. N., Perry, A., Reifenberger, G., von Deimling, A., Figarella-Branger, D., Cavenee, W. K., Ohgaki, H., Wiestler, O. D., Kleihues, P., and Ellison, D. W. The 2016 world health organization classification of tumors of the central nervous system: a summary. *Acta Neuropathologica*, 131(6):803–820, 2016. ISSN 1432-0533. doi: 10.1007/s00401-016-1545-1. URL `https://doi.org/10.1007/s00401-016-1545-1`.

Louis, D. N., Perry, A., Wesseling, P., Brat, D. J., Cree, I. A., Figarella-Branger, D., Hawkins, C., Ng, H. K., Pfister, S. M., Reifenberger, G., Soffietti, R., von Deimling, A., and Ellison, D. W. The 2021 WHO classification of tumors of the central nervous system: a summary. *Neuro-oncology*, 23:1231–1251, Aug 2021.

Loução, R., Oros-Peusquens, A.-M., Langen, K.-J., Ferreira, H., and Shah, N. A fast protocol for multiparametric characterisation of diffusion in the brain and brain tumours. *Frontiers in Oncology*, 11:554205, 2021. doi: 10.3389/fonc.2021.554205.

Lu, H., Jensen, J. H., Ramani, A., and Helpern, J. A. Three-dimensional characterization of non-gaussian water diffusion in humans using diffusion kurtosis imaging. *NMR Biomed.*, 19(2):236–247, April 2006. ISSN 0952-3480. doi: 10.1002/nbm.1020. URL `https://doi.org/10.1002/nbm.1020`.

Lätt, J., Nilsson, M., Wirestam, R., Ståhlberg, F., Karlsson, N., Johansson, M., Sundgren, P. C., and van Westen, D. Regional values of diffusional kurtosis estimates in the healthy brain. *J. Magn. Reson. Imaging*, 37(3):610–618, March 2013. ISSN 1053-1807. doi: 10.1002/jmri.23857. URL `https://doi.org/10.1002/jmri.23857`.

Mackay, A., Whittall, K., Adler, J., Li, D., Paty, D., and Graeb, D. In vivo visualization of myelin water in brain by magnetic resonance. *Magn. Reson. Med.*, 31(6):673–677, June 1994. ISSN 0740-3194. doi: 10.1002/mrm.1910310614. URL `https://doi.org/10.1002/mrm.1910310614`.

Maier, S. E. and Mulkern, R. V. Biexponential analysis of diffusion-related signal decay in normal human cortical and deep gray matter. *Magnetic resonance imaging*, 26:897–904, Sep 2008. doi: doi:10.1016/j.mri.2008.01.042.

Maier, S. E., Sun, Y., and Mulkern, R. V. Diffusion imaging of brain tumors. *NMR in biomedicine*, 23:849–64, Aug 2010. doi: doi:10.1016/j.mri.2008.01.042.

Mansfield, P. Multi-planar image formation using NMR spin echoes. *Journal of Physics C: Solid State Physics*, 10(3): L55, 1977. ISSN 0022-3719. doi: 10.1088/0022-3719/10/3/004. URL `https://dx.doi.org/10.1088/0022-3719/10/3/004`.

Manzano-Patron, J.-P., Moeller, S., Andersson, J. L. R., Yacoub, E., and Sotiropoulos, S. N. Denoising diffusion MRI: Considerations and implications for analysis., July 2023.

Markl, M. and Leupold, J. Gradient echo imaging. *J. Magn. Reson. Imaging*, 35(6):1274–1289, June 2012. ISSN 1053-1807. doi: 10.1002/jmri.23638. URL https://doi.org/10.1002/jmri.23638.

Meeus, E. M., Novak, J., Withey, S. B., Zarinabad, N., Dehghani, H., and Peet, A. C. Evaluation of intravoxel incoherent motion fitting methods in low-perfused tissue. *Journal of Magnetic Resonance Imaging*, 45(5):1325–1334, aug 2016. doi: 10.1002/jmri.25411.

Mong, S., Ellingson, B. M., Nghiemphu, P. L., Kim, H. J., Mirsadraei, L., Lai, A., Yong, W., Zaw, T. M., Cloughesy, T. F., and Pope, W. B. Persistent diffusion-restricted lesions in bevacizumab-treated malignant gliomas are associated with improved survival compared with matched controls. *AJNR. American journal of neuroradiology*, 33:1763–70, Oct 2012.

Moseley, M. E., Kucharczyk, J., Mintorovitch, J., Cohen, Y., Kurhanewicz, J., Derugin, N., Asgari, H., and Norman, D. Diffusion-weighted MR imaging of acute stroke: correlation with T2-weighted and magnetic susceptibility-enhanced mr imaging in cats. *AJNR. American journal of neuroradiology*, 11:423–9, May 1990.

Mulkern, R. V., Vajapeyam, S., Robertson, R. L., Caruso, P. A., Rivkin, M. J., and Maier, S. E. Biexponential apparent diffusion coefficient parametrization in adult vs newborn brain. *Magnetic resonance imaging*, 19:659–68, Jun 2001.

Mulkern, R. V., Gudbjartsson, H., Westin, C.-F., Zengingonul, H. P., Gartner, W., Guttmann, C. R. G., Robertson, R. L., Kyriakos, W., Schwartz, R., Holtzman, D., Jolesz, F. A., and Maier, S. E. Multi-component apparent diffusion coefficients in human brain. *NMR Biomed.*, 12(1):51–62, February 1999. ISSN 0952-3480. URL https://doi.org/10.1002/(SICI)1099-1492(199902)12:1<51::AID-NBM546>3.0.CO;2-E.

Nael, K., Bauer, A. H., Hormigo, A., Lemole, M., Germano, I. M., Puig, J., and Stea, B. Multiparametric MRI for differentiation of radiation necrosis from recurrent tumor in patients with treated glioblastoma. *American Journal of Roentgenology*, 210(1):18–23, September 2017. ISSN 0361-803X. doi: 10.2214/AJR.17.18003. URL https://doi.org/10.2214/AJR.17.18003.

Neto Henriques, R., Correia, M. M., Nunes, R. G., and Ferreira, H. A. Exploring the 3D geometry of the diffusion kurtosis tensor: Impact on the development of robust tractography procedures and novel biomarkers. *NeuroImage*, 111:85–99, 2015. ISSN 1053-8119. doi: 10.1016/j.neuroimage.2015.02.004. URL https://www.sciencedirect.com/science/article/pii/S1053811915000968.

Nguyen, H. S., Milbach, N., Hurrell, S. L., Cochran, E., Connelly, J., Bovi, J. A., Schultz, C. J., Mueller, W. M., Rand, S. D., Schmainda, K. M., and LaViolette, P. S. Progressing bevacizumab-induced diffusion restriction is associated with coagulative necrosis surrounded by viable tumor and decreased overall survival in patients with recurrent glioblastoma. *AJNR. American journal of neuroradiology*, 37:2201–2208, Dec 2016.

Ogura, A., Hayakawa, K., Miyati, T., and Maeda, F. Imaging parameter effects in apparent diffusion coefficient determination of magnetic resonance imaging. *European Journal of Radiology*, 77(1):185–188, January 2011. ISSN 0720-048X. doi: 10.1016/j.ejrad.2009.06.031. URL https://doi.org/10.1016/j.ejrad.2009.06.031.

Oh, J., Cha, S., Aiken, A. H., Han, E. T., Crane, J. C., Stainsby, J. A., Wright, G. A., Dillon, W. P., and Nelson, S. J. Quantitative apparent diffusion coefficients and T2 relaxation times in characterizing contrast enhancing brain tumors and regions of peritumoral edema. *J. Magn. Reson. Imaging*, 21(6):701–708, June 2005. ISSN 1053-1807. doi: 10.1002/jmri.20335. URL https://doi.org/10.1002/jmri.20335.

Olivero, W. C., Dulebohn, S. C., and Lister, J. R. The use of PET in evaluating patients with primary brain tumours: is it useful? *J Neurol Neurosurg Psychiatry*, 58(2):250, February 1995. doi: 10.1136/jnnp.58.2.250. URL http://jnnp.bmj.com/content/58/2/250.abstract.

Oros-Peusquens, A. M. and Shah, N. J. A simple and efficient method for acceleration and denoising of multi-contrast diffusion data: Application to Q-Space and HARDI. In *Proceedings of International Society of Magnetic Resonance in Medicine*, 21:3219, 2013.

Oros-Peusquens, A. M., Loução, R., Zimmermann, M., Langen, K.-J., and Shah, N. J. Methods for molecular imaging of brain tumours in a hybrid MR-PET context: Water content, T2*, diffusion indices and FET-PET. *Methods*, 130:135–151, 2017. ISSN 1046-2023. doi: 10.1016/j.ymeth.2017.07.025. URL https://www.sciencedirect.com/science/article/pii/S1046202317300907.

Ostrom, Q. T., Gittleman, H., Liao, P., Rouse, C., Chen, Y., Dowling, J., Wolinsky, Y., Kruchko, C., and Barnholtz-Sloan, J. CBTRUS statistical report: primary brain and central nervous system tumors diagnosed in the United States in 2007-2011. *Neuro-oncology*, 16 Suppl 4:iv1–63, Oct 2014.

Papadopoulos, M. C., Saadoun, S., and Verkman, A. S. Aquaporins and cell migration. *Pflugers Archiv : European journal of physiology*, 456:693–700, Jul 2008.

Patronas, N. J., Brooks, R. A., DeLaPaz, R. L., Smith, B. H., Kornblith, P. L., and Di Chiro, G. Glycolytic rate (PET) and contrast enhancement (CT) in human cerebral gliomas. *AJNR. American journal of neuroradiology*, 4: 533–5, May-Jun 1983.

Pauleit, D., Floeth, F., Hamacher, K., Riemenschneider, M. J., Reifenberger, G., Müller, H.-W., Zilles, K., Coenen, H. H., and Langen, K.-J. O-(2-[18f]fluoroethyl)-l-tyrosine PET combined with MRI improves the diagnostic assessment of cerebral gliomas. *Brain*, 128(3):678–687, March 2005. ISSN 0006-8950. doi: 10.1093/brain/awh399. URL `https://doi.org/10.1093/brain/awh399`.

Pauleit, D., Stoffels, G., Bachofner, A., Floeth, F. W., Sabel, M., Herzog, H., Tellmann, L., Jansen, P., Reifenberger, G., Hamacher, K., Coenen, H. H., and Langen, K.-J. Comparison of (18)F-FET and (18)F-FDG PET in brain tumors. *Nuclear medicine and biology*, 36:779–87, Oct 2009.

Periquito, J. S., Gladytz, T., Millward, J. M., Delgado, P. R., Cantow, K., Grosenick, D., Hummel, L., Anger, A., Zhao, K., Seeliger, E., Pohlmann, A., Waiczies, S., and Niendorf, T. Continuous diffusion spectrum computation for diffusion-weighted magnetic resonance imaging of the kidney tubule system. *Quantitative imaging in medicine and surgery*, 11:3098–3119, Jul 2021.

Perman, W. H., Hilal, S. K., Simon, H. E., and Maudsley, A. A. Contrast manipulation in NMR imaging. *Magnetic resonance imaging*, 2:23–32, 1984.

Pierpaoli, C., Walker, L., Irfanoglu, M. O., Barnett, A., Basser, P., Chang, L.-C., Koay, C., Pajevic, S., Rohde, G., and Wu, M. TORTOISE: an integrated software package for processing of diffusion MRI data. In *Proceedings of International Society of Magnetic Resonance in Medicine*, abstract nr. 1597, 2010.

Puig, J., Sánchez-González, J., Blasco, G., Daunis-i Estadella, P., Federau, C., Alberich-Bayarri, A., Biarnes, C., Nael, K., Essig, M., Jain, R., Wintermark, M., and Pedraza, S. Intravoxel incoherent motion metrics as potential biomarkers for survival in glioblastoma. *PLOS ONE*, 11(7):e0158887, July 2016. doi: 10.1371/journal.pone.0158887. URL `https://doi.org/10.1371/journal.pone.0158887`.

Purcell, E. M., Torrey, H. C., and Pound, R. V. Resonance absorption by nuclear magnetic moments in a solid. *PR*, 69 (1-2):37–38, January 1946. doi: 10.1103/PhysRev.69.37. URL `https://link.aps.org/doi/10.1103/PhysRev.69.37`.

Qi, C., Yang, S., Meng, L., Chen, H., Li, Z., Wang, S., Jiang, T., and Li, S. Evaluation of cerebral glioma using 3T diffusion kurtosis tensor imaging and the relationship between diffusion kurtosis metrics and tumor cellularity. *The Journal of international medical research*, 45:1347–1358, Aug 2017. doi: doi:10.1177/0300060517712654.

Rieger, J., Bähr, O., Müller, K., Franz, K., Steinbach, J., and Hattingen, E. Bevacizumab-induced diffusion-restricted lesions in malignant glioma patients. *Journal of Neuro-Oncology*, 99(1):49–56, 2010. ISSN 1573-7373. doi: 10.1007/s11060-009-0098-8. URL `https://doi.org/10.1007/s11060-009-0098-8`.

Ruggiero, M. R., Ait Itto, H., Baroni, S., Pierre, S., Boutonnat, J., Broche, L. M., Aime, S., Berger, F., Geninatti Crich, S., and Lahrech, H. Role of transmembrane water exchange in glioma invasion/migration: In vivo preclinical study by relaxometry at very low magnetic field. *Cancers*, 14(17), 2022. ISSN 2072-6694. doi: 10.3390/cancers14174180. URL `https://www.mdpi.com/2072-6694/14/17/4180`.

Rydelius, A., Bengzon, J., Engelholm, S., Kinhult, S., Englund, E., Nilsson, M., Lätt, J., Lampinen, B., and Sundgren, P. C. Predictive value of diffusion MRI-based parametric response mapping for prognosis and treatment response in glioblastoma. *Magnetic resonance imaging*, Sep 2023.

Saier, M. H., Daniels, G. A., Boerner, P., and Lin, J. Neutral amino acid transport systems in animal cells: Potential targets of oncogene action and regulators of cellular growth. *The Journal of Membrane Biology*, 104(1):1–20, 1988. ISSN 1432-1424. doi: 10.1007/BF01871898. URL `https://doi.org/10.1007/BF01871898`.

Seo, H. S., Chang, K.-H., Na, D. G., Kwon, B. J., and Lee, D. H. High b-value diffusion (b = 3000 s/mm2) MR imaging in cerebral gliomas at 3T: Visual and quantitative comparisons with b = 1000 s/mm2. *Am. J. Neuroradiol.*, 29(3):458, March 2008. doi: 10.3174/ajnr.A0842. URL `http://www.ajnr.org/content/29/3/458.abstract`.

Singhal, T., Narayanan, T. K., Jain, V., Mukherjee, J., and Mantil, J. 11C-L-methionine positron emission tomography in the clinical management of cerebral gliomas. *Molecular imaging and biology*, 10:1–18, Jan-Feb 2008.

Smirniotopoulos, J. G., Murphy, F. M., Rushing, E. J., Rees, J. H., and Schroeder, J. W. Patterns of contrast enhancement in the brain and meninges. *RadioGraphics*, 27(2):525–551, March 2007. ISSN 0271-5333. doi: 10.1148/rg.272065155. URL `https://doi.org/10.1148/rg.272065155`.

Spraggins, T. A. A perspective on k-space. *Radiology*, 199(3):874b–875, June 1996. ISSN 0033-8419. doi: 10.1148/radiology.199.3.8638022. URL https://doi.org/10.1148/radiology.199.3.8638022.

Springer Jr, C. S., Baker, E. M., Li, X., Moloney, B., Pike, M. M., Wilson, G. J., Anderson, V. C., Sammi, M. K., Garzotto, M. G., Kopp, R. P., Coakley, F. V., Rooney, W. D., and Maki, J. H. Metabolic activity diffusion imaging (MADI): II. noninvasive, high-resolution human brain mapping of sodium pump flux and cell metrics. *NMR in biomedicine*, 36:e4782, Jan 2023a.

Springer Jr, C. S., Baker, E. M., Li, X., Moloney, B., Wilson, G. J., Pike, M. M., Barbara, T. M., Rooney, W. D., and Maki, J. H. Metabolic activity diffusion imaging (MADI): I. metabolic, cytometric modeling and simulations. *NMR in biomedicine*, 36:e4781, Jan 2023b.

Stejskal, E. O. and Tanner, J. E. Spin diffusion measurements: spin echoes in the presence of a time-dependent field gradient. *The journal of chemical physics*, 42(1):288–292, 1965.

Stokum, J. A., Gerzanich, V., and Simard, J. M. Molecular pathophysiology of cerebral edema. *J Cereb Blood Flow Metab*, 36(3):513–538, November 2015. ISSN 0271-678X. doi: 10.1177/0271678X15617172. URL https://doi.org/10.1177/0271678X15617172.

Stupp, R., Brada, M., van den Bent, M. J., Tonn, J.-C., and Pentheroudakis, G. High-grade glioma: ESMO clinical practice guidelines for diagnosis, treatment and follow-up. *Annals of Oncology*, 25:iii93–iii101, September 2014. ISSN 0923-7534. doi: 10.1093/annonc/mdu050. URL https://doi.org/10.1093/annonc/mdu050.

Stupp, R., Mason, W. P., van den Bent, M. J., Weller, M., Fisher, B., Taphoorn, M. J. B., Belanger, K., Brandes, A. A., Marosi, C., Bogdahn, U., Curschmann, J., Janzer, R. C., Ludwin, S. K., Gorlia, T., Allgeier, A., Lacombe, D., Cairncross, J. G., Eisenhauer, E., and Mirimanoff, R. O. Radiotherapy plus concomitant and adjuvant temozolomide for glioblastoma. *The New England journal of medicine*, 352:987–96, Mar 2005.

Sugahara, T., Korogi, Y., Kochi, M., Ikushima, I., Shigematu, Y., Hirai, T., Okuda, T., Liang, L., Ge, Y., Komohara, Y., Ushio, Y., and Takahashi, M. Usefulness of diffusion-weighted MRI with echo-planar technique in the evaluation of cellularity in gliomas. *Journal of magnetic resonance imaging : JMRI*, 9:53–60, Jan 1999.

Suh, C. H., Kim, H. S., Jung, S. C., and Kim, S. J. Diffusion-weighted imaging and diffusion tensor imaging for differentiating high-grade glioma from solitary brain metastasis: A systematic review and meta-analysis. *AJNR. American journal of neuroradiology*, 39:1208–1214, Jul 2018.

Suh, C. H., Kim, H. S., Jung, S. C., Choi, C. G., and Kim, S. J. Imaging prediction of isocitrate dehydrogenase (IDH) mutation in patients with glioma: a systemic review and meta-analysis. *European radiology*, 29:745–758, Feb 2019.

Sun, Y., Mulkern, R. V., Schmidt, K., Doshi, S., Albert, M. S., Schmidt, N. O., Ziu, M., Black, P., Carrol, R., and Kieran, M. W. Quantification of water diffusion and relaxation times of human U87 tumors in a mouse model. *NMR Biomed.*, 17(6):399–404, October 2004. ISSN 0952-3480. doi: 10.1002/nbm.894. URL https://doi.org/10.1002/nbm.894.

Svolos, P., Kousi, E., Kapsalaki, E., Theodorou, K., Fezoulidis, I., Kappas, C., and Tsougos, I. The role of diffusion and perfusion weighted imaging in the differential diagnosis of cerebral tumors: a review and future perspectives. *Cancer imaging : the official publication of the International Cancer Imaging Society*, 14:20, Apr 2014. doi: doi:10.1186/1470-7330-14-20.

Tanner, J. E. and Stejskal, E. O. Restricted self-diffusion of protons in colloidal systems by the pulsed-gradient, spin-echo method. *The Journal of Chemical Physics*, 49(4):1768–1777, 09 1968. ISSN 0021-9606. doi: 10.1063/1.1670306. URL https://doi.org/10.1063/1.1670306.

Tietze, A., Hansen, M. B., Østergaard, L., Jespersen, S. N., Sangill, R., Lund, T. E., Geneser, M., Hjelm, M., and Hansen, B. Mean diffusional kurtosis in patients with glioma: Initial results with a fast imaging method in a clinical setting. *Am. J. Neuroradiol.*, 36(8):1472, August 2015. doi: 10.3174/ajnr.A4311. URL http://www.ajnr.org/content/36/8/1472.abstract.

Tikhonov, A. N. and Arsenin, V. I. A. *Solutions of Ill-posed Problems*. Winston, 1977. URL https://books.google.de/books?id=ECrvAAAAMAAJ.

Tozer, D. J., Rees, J. H., Benton, C. E., Waldman, A. D., Jäger, H. R., and Tofts, P. S. Quantitative magnetisation transfer imaging in glioma: preliminary results. *NMR in Biomedicine*, 24(5):492–498, 2011. doi: https://doi.org/10.1002/nbm.1614. URL https://analyticalsciencejournals.onlinelibrary.wiley.com/doi/abs/10.1002/nbm.1614.

Tustison, N. J., Shrinidhi, K. L., Wintermark, M., Durst, C. R., Kandel, B. M., Gee, J. C., Grossman, M. C., and Avants, B. B. Optimal symmetric multimodal templates and concatenated random forests for supervised brain tumor segmentation (simplified) with ANTsR. *Neuroinformatics*, 13(2):209–225, 2015. ISSN 1559-0089. doi: 10.1007/s12021-014-9245-2. URL https://doi.org/10.1007/s12021-014-9245-2.

Van Cauter, S., Veraart, J., Sijbers, J., Peeters, R. R., Himmelreich, U., De Keyzer, F., Van Gool, S. W., Van Calenbergh, F., De Vleeschouwer, S., Van Hecke, W., and Sunaert, S. Gliomas: Diffusion kurtosis MR imaging in grading. *Radiology*, 263(2):492–501, May 2012. ISSN 0033-8419. doi: 10.1148/radiol.12110927. URL https://doi.org/10.1148/radiol.12110927.

Vargová, L., Homola, A., Zámecník, J., Tichý, M., Benes, V., and Syková, E. Diffusion parameters of the extracellular space in human gliomas. *Glia*, 42:77–88, Apr 2003.

Veraart, J., Fieremans, E., and Novikov, D. S. Diffusion MRI noise mapping using random matrix theory. *Magn. Reson. Med.*, 76(5):1582–1593, November 2016a. ISSN 0740-3194. doi: 10.1002/mrm.26059. URL https://doi.org/10.1002/mrm.26059.

Veraart, J., Novikov, D. S., Christiaens, D., Ades-Aron, B., Sijbers, J., and Fieremans, E. Denoising of diffusion MRI using random matrix theory. *NeuroImage*, 142:394–406, Nov 2016b.

Verger, A., Filss, C. P., Lohmann, P., Stoffels, G., Sabel, M., Wittsack, H. J., Kops, E. R., Galldiks, N., Fink, G. R., Shah, N. J., and Langen, K.-J. Comparison of (18)F-FET PET and perfusion-weighted MRI for glioma grading: a hybrid PET/MR study. *European journal of nuclear medicine and molecular imaging*, 44:2257–2265, Dec 2017. doi: doi:10.1007/s00259-017-3812-3.

Villanueva-Meyer, J. E., Mabray, M. C., and Cha, S. Current clinical brain tumor imaging. *Neurosurgery*, 81:397–415, Sep 2017. doi: doi:10.1093/neuros/nyx103.

Wang, Q.-P., Lei, D.-Q., Yuan, Y., and Xiong, N.-X. Accuracy of ADC derived from DWI for differentiating high-grade from low-grade gliomas: Systematic review and meta-analysis. *Medicine*, 99:e19254, Feb 2020.

Weiss Lucas, C., Faymonville, A. M., Loução, R., Schroeter, C., Nettekoven, C., Oros-Peusquens, A.-M., Langen, K. J., Shah, N. J., Stoffels, G., Neuschmelting, V., Blau, T., Neuschmelting, H., Hellmich, M., Kocher, M., Grefkes, C., and Goldbrunner, R. Surgery of motor eloquent glioblastoma guided by tms-informed tractography: Driving resection completeness towards prolonged survival. *Frontiers in oncology*, 12:874631, 2022.

Weller, M., van den Bent, M., Hopkins, K., Tonn, J. C., Stupp, R., Falini, A., Cohen-Jonathan-Moyal, E., Frappaz, D., Henriksson, R., Balana, C., Chinot, O., Ram, Z., Reifenberger, G., Soffietti, R., and Wick, W. EANO guideline for the diagnosis and treatment of anaplastic gliomas and glioblastoma. *The Lancet. Oncology*, 15:e395–403, Aug 2014.

Weller, M., van den Bent, M., Preusser, M., Le Rhun, E., Tonn, J. C., Minniti, G., Bendszus, M., Balana, C., Chinot, O., Dirven, L., French, P., Hegi, M. E., Jakola, A. S., Platten, M., Roth, P., Rudà, R., Short, S., Smits, M., Taphoorn, M. J. B., von Deimling, A., Westphal, M., Soffietti, R., Reifenberger, G., and Wick, W. EANO guidelines on the diagnosis and treatment of diffuse gliomas of adulthood. *Nature reviews. Clinical oncology*, 18:170–186, Mar 2021.

Wen, P. Y., Macdonald, D. R., Reardon, D. A., Cloughesy, T. F., Sorensen, A. G., Galanis, E., DeGroot, J., Wick, W., Gilbert, M. R., Lassman, A. B., Tsien, C., Mikkelsen, T., Wong, E. T., Chamberlain, M. C., Stupp, R., Lamborn, K. R., Vogelbaum, M. A., van den Bent, M. J., and Chang, S. M. Updated response assessment criteria for high-grade gliomas: Response assessment in neuro-oncology working group. *JCO*, 28(11):1963–1972, March 2010. ISSN 0732-183X. doi: 10.1200/JCO.2009.26.3541. URL https://doi.org/10.1200/JCO.2009.26.3541.

White, M. L., Zhang, Y., Yu, F., and Kazmi, S. A. J. Diffusion tensor MR imaging of cerebral gliomas: Evaluating fractional anisotropy characteristics. *Am. J. Neuroradiol.*, 32(2):374, February 2011. doi: 10.3174/ajnr.A2267. URL http://www.ajnr.org/content/32/2/374.abstract.

Whittall, K. P. and MacKay, A. L. Quantitative interpretation of NMR relaxation data. *Journal of Magnetic Resonance (1969)*, 84(1):134–152, 1989. ISSN 0022-2364. doi: 10.1016/0022-2364(89)90011-5. URL https://www.sciencedirect.com/science/article/pii/0022236489900115.

Wu, O., Koroshetz, W. J., Østergaard, L., Buonanno, F. S., Copen, W. A., Gonzalez, R. G., Rordorf, G., Rosen, B. R., Schwamm, L. H., Weisskoff, R. M., and Sorensen, A. G. Predicting tissue outcome in acute human cerebral ischemia using combined diffusion- and perfusion-weighted MR imaging. *Stroke*, 32(4):933–942, April 2001. doi: 10.1161/01.STR.32.4.933. URL https://doi.org/10.1161/01.STR.32.4.933.

Wu, W.-C., Chen, Y.-F., Tseng, H.-M., Yang, S.-C., and My, P.-C. Caveat of measuring perfusion indexes using intravoxel incoherent motion magnetic resonance imaging in the human brain. *European Radiology*, 25(8):2485–2492, 2015. ISSN 1432-1084. doi: 10.1007/s00330-015-3655-x. URL https://doi.org/10.1007/s00330-015-3655-x.

Xiong, J., Tan, W.-L., Pan, J.-W., Wang, Y., Yin, B., Zhang, J., and Geng, D.-Y. Detecting isocitrate dehydrogenase gene mutations in oligodendroglial tumors using diffusion tensor imaging metrics and their correlations with proliferation and microvascular density. *Journal of magnetic resonance imaging : JMRI*, 43:45–54, Jan 2016.

Yamasaki, F., Kurisu, K., Aoki, T., Yamanaka, M., Kajiwara, Y., Watanabe, Y., Takayasu, T., Akiyama, Y., and Sugiyama, K. Advantages of high b-value diffusion-weighted imaging to diagnose pseudo-responses in patients with recurrent glioma after bevacizumab treatment. *European journal of radiology*, 81:2805–10, Oct 2012.

Yu, Y., Ma, Y., Sun, M., Jiang, W., Yuan, T., and Tong, D. Meta-analysis of the diagnostic performance of diffusion magnetic resonance imaging with apparent diffusion coefficient measurements for differentiating glioma recurrence from pseudoprogression. *Medicine*, 99:e20270, Jun 2020.

Zeng, Q., Dong, F., Shi, F., Ling, C., Jiang, B., and Zhang, J. Apparent diffusion coefficient maps obtained from high b value diffusion-weighted imaging in the preoperative evaluation of gliomas at 3T: comparison with standard b value diffusion-weighted imaging. *European Radiology*, 27(12):5309–5315, 2017. ISSN 1432-1084. doi: 10.1007/s00330-017-4910-0. URL `https://doi.org/10.1007/s00330-017-4910-0`.

Zeng, Q., Shi, F., Zhang, J., Ling, C., Dong, F., and Jiang, B. A modified tri-exponential model for multi-b-value diffusion-weighted imaging: A method to detect the strictly diffusion-limited compartment in brain. *Frontiers in neuroscience*, 12:102, 2018.

Zhang, L., Min, Z., Tang, M., Chen, S., Lei, X., and Zhang, X. The utility of diffusion MRI with quantitative ADC measurements for differentiating high-grade from low-grade cerebral gliomas: Evidence from a meta-analysis. *Journal of the neurological sciences*, 373:9–15, Feb 2017.

Zhang, M., Gulotta, B., Thomas, A., Kaley, T., Karimi, S., Gavrilovic, I., Woo, K. M., Zhang, Z., Arevalo-Perez, J., Holodny, A. I., Rosenblum, M., and Young, R. J. Large-volume low apparent diffusion coefficient lesions predict poor survival in bevacizumab-treated glioblastoma patients. *Neuro Oncol*, 18(5):735–743, May 2016. ISSN 1522-8517. doi: 10.1093/neuonc/nov268. URL `https://doi.org/10.1093/neuonc/nov268`.

Annexes

A. Additional Simulations of IVIM/NG-diff

In order to investigate to which extent the SNR, sampling strategy of b-value, degree of perfusion, averaging, and size of ROI, simulations were conducted. Accuracy and precision were investigated in regards of relative error and coefficient of variation, respectively.

A.1. Effect of SNR

Two SNR ranges were considered: an SNR range typical of clinical environment, ranging from 20 to 60 (clinical SNR range), in intervals of 10; and a second SNR range from 200 to 1000, in intervals of 200 (high SNR range).

In figs. A.1 and A.2 are presented the percent error vs SNR, and in Figs. A.3 and A.4 the coefficient of variation vs SNR, for the clinical and high SNR ranges, respectively.

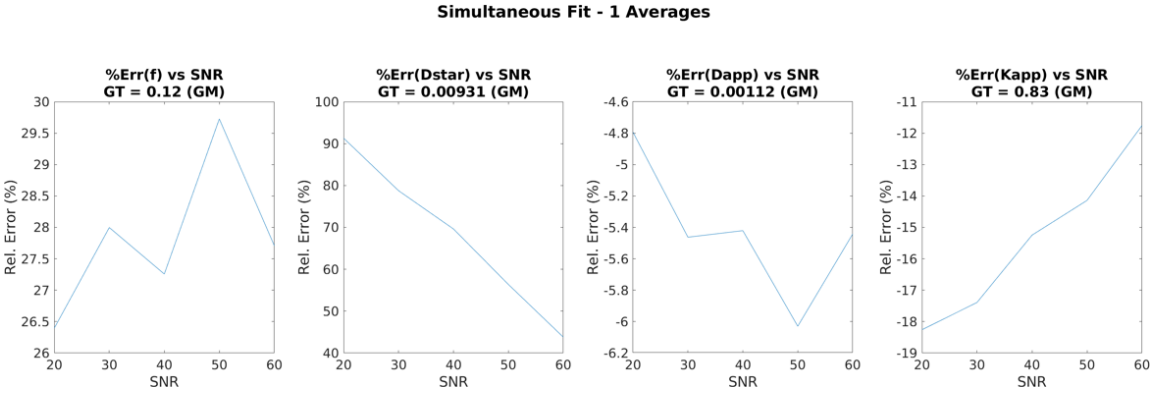

Figure A.1.: *Relative error of estimated parameters in simulated GM at clinical SNR.*

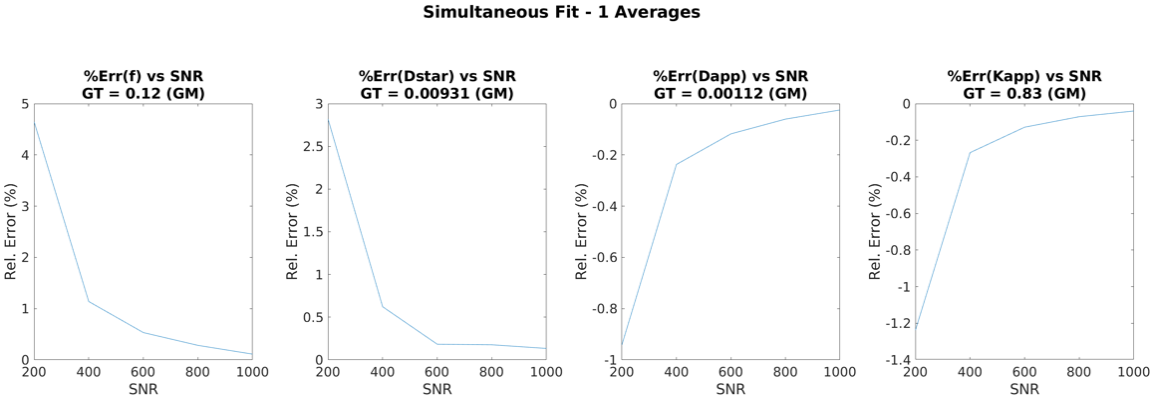

Figure A.2.: *Relative error of estimated parameters in simulated GM at high SNR.*

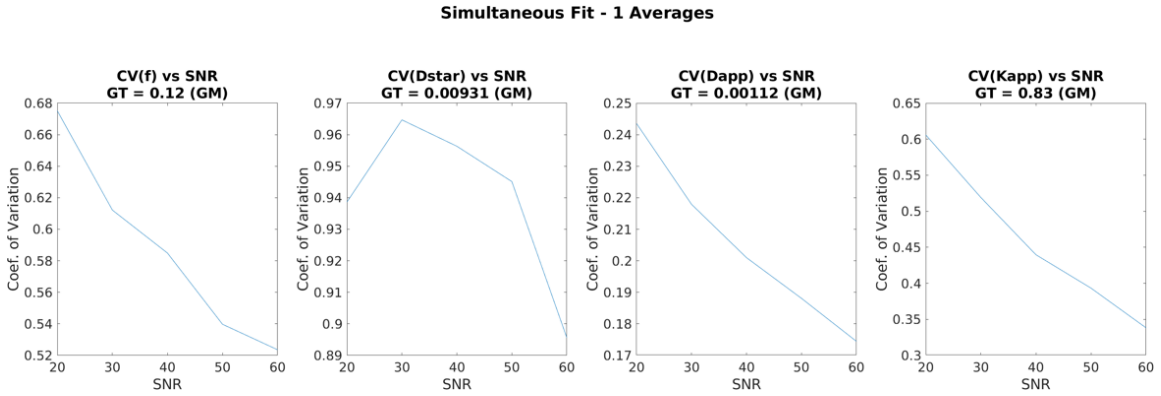

Figure A.3.: *Coefficient of variation of estimated parameters in simulated GM at clinical SNR.*

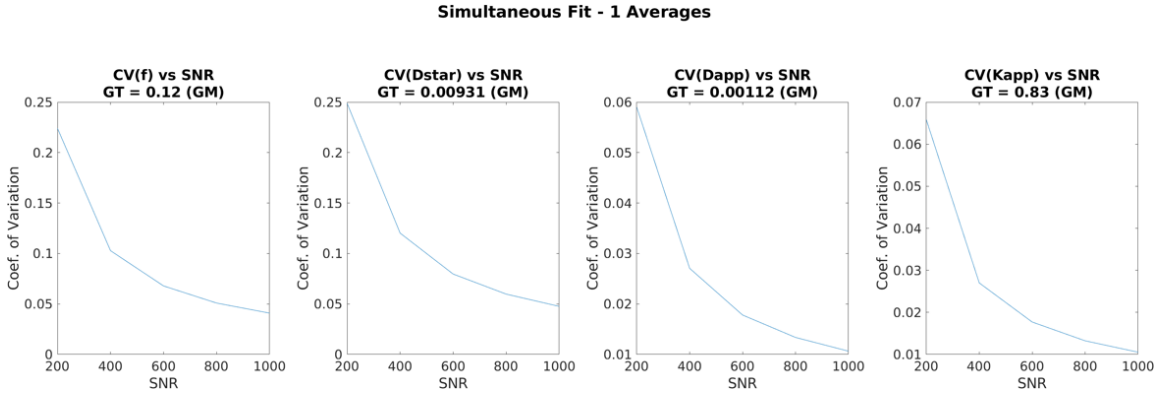

Figure A.4.: *Coefficient of variation of estimated parameters in simulated GM at clinical SNR.*

A.2. Effect of b-value sampling

To asses the influence of the b-value sampling scheme, an additional, dense sampling strategy was investigated, ranging from 0 to 2000 s/mm^2 in intervals of 10 s/mm^2 (dense scheme), whose simulation results can be seen in Figs. A.5 and A.6.

A.3. Effect of perfusion amount

Until now, the simulations focused on an simulated tissue with diffusion properties akin to GM. So as to determine to which extent the perfusion amount/tissue type affect the accuracy of the fits, different "ground-truth" curves (simulating different tissues) were drawn up. In addition to the tissues included in Chapter 4 (GM, WM with high FA, WM with low FA, oedema, and tumour), an additional fictitious tissue with high perfusion fraction (f = 0.3) was tested, keeping all other parameters the same as those in GM. Such high level of perfusion is not uncommon in other organs, e.g. the kidney.

In Chapter 4, the reader will find the simulation results of the non-fictitious tissues. In this Annex will only be shown the results of the fictitious tissue and non-fictitious GM for comparison, summarised in Fig. A.7.

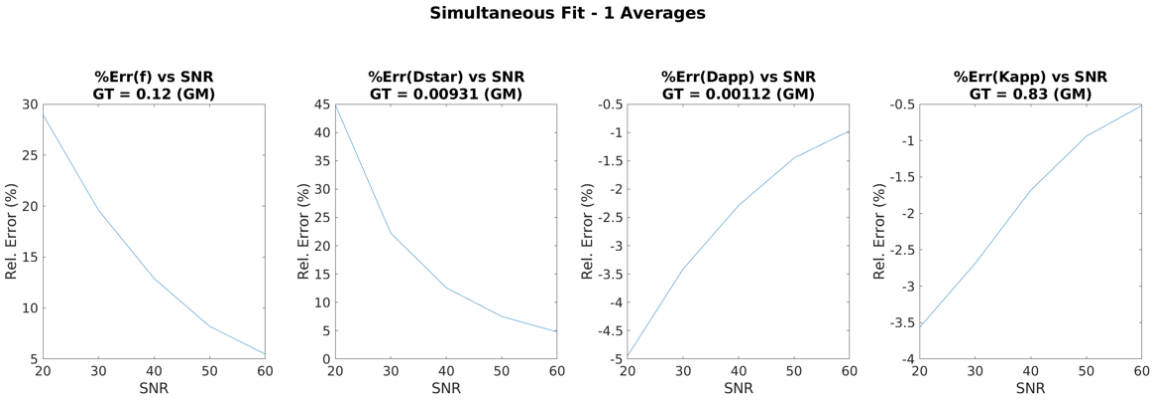

Figure A.5.: *Relative error of estimated parameters derived from the dense b-value scheme at clinical SNR range in simulated GM.*

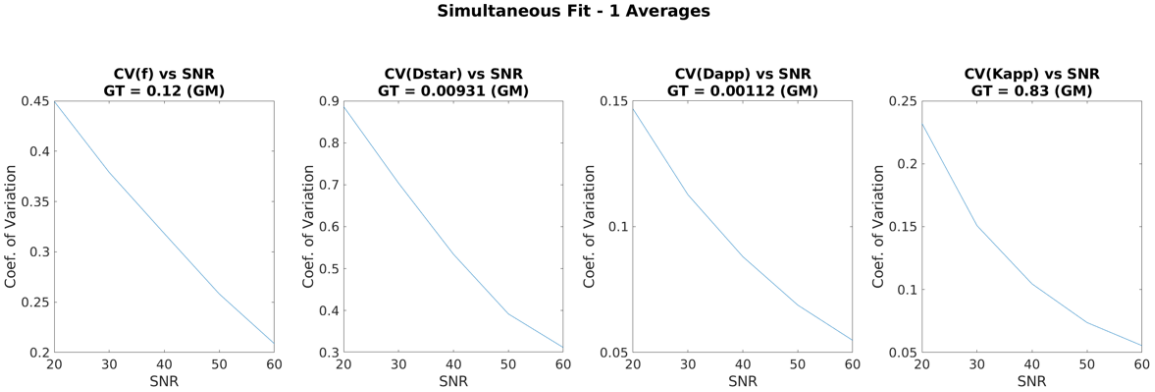

Figure A.6.: *Coefficient of variation of estimated parameters derived from the dense b-value scheme at clinical SNR range in simulated GM.*

A.4. Effect of averaging and size of ROI

The effect of averaging was investigated thusly. Simulations were conducted without averages (i.e. one decay per fit), and with 8 averages (i.e. 8 signals independently sampled and then averaged prior to fit). Results are shown in Fig. A.8.

One of the ideas behind developing the proposed protocol was to be able to provide a tissue characterising parameter, obtained by averaging signals of neighbouring voxels. Averaging increases the effective SNR of the data, additional investigations included the relationship between the ROI (tumour) size, effective SNR, and accuracy of parameter estimation. To achieve this, simulations were conducted using a set of 40 "amounts of voxels" (ROI sizes) with volumes ranging from 50 to 200,000 voxels, logarithmically sampled. The tumour volumes in the cohort of Chapter 4 ranged from 108 to 10,611 voxels. Each ROI was simulated and fitted 10,000 times with independently sampled noise.

A relationship between the effective SNR and size of ROI in voxels can be seen in Fig. A.9, ranging from around 140 for the smallest ROI, to close to 9000 for the biggest ROI. Accuracy and precision results for each metric are shown in Figs. A.10 and A.11, respectively.

To further determine the robustness of the ROI-based fit, a second variation of these simulations was conducted. In the first ROI simulation, all voxels in the ROI shared the

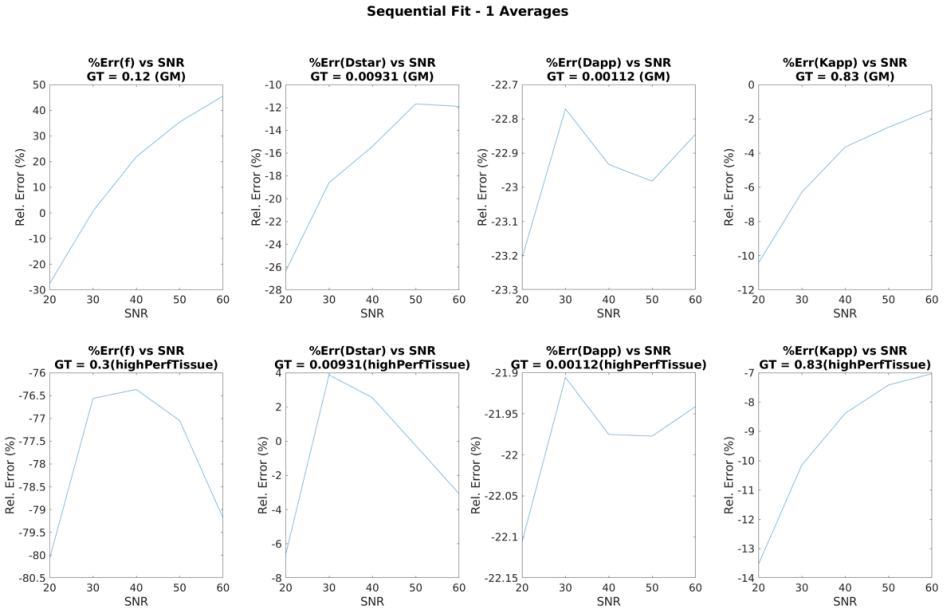

Figure A.7.: *Relative error estimated metrics in non-fictitious GM and fictitious high perfusion tissue at clinical SNR with the proposed sampling scheme.*

same ground truth. On the other hand, the second simulation had each voxel have an independent "ground truth" curve, to which noise was then added (variable ground truth), with each metric being randomly selected from [0.5*GT, 1.5*GT] (here GT are the tumour ground truth parameters from the ROI fit of the *in vivo* data). The relative error plots to each parameter's ground truth are summarised in Fig. A.12.

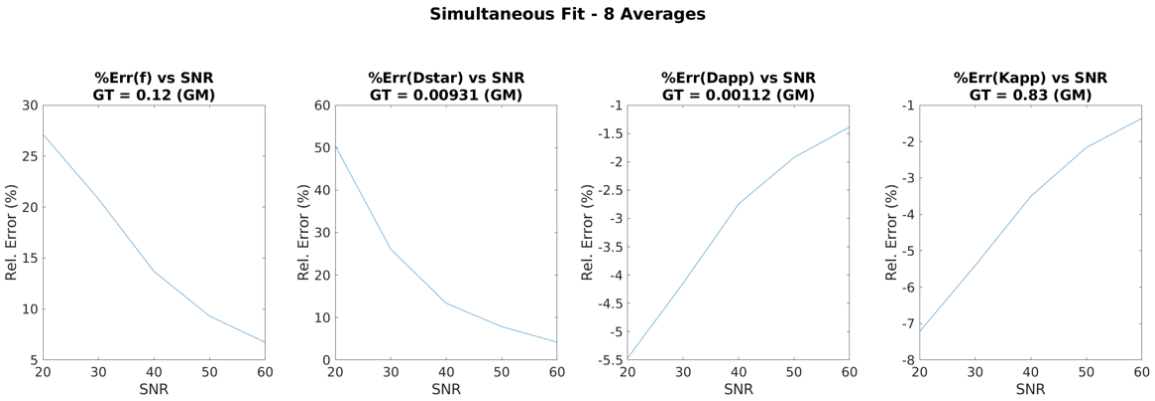

Figure A.8.: *Relative error in fitting parameters using 8 averages, clinical SNR range and the proposed b-value scheme.*

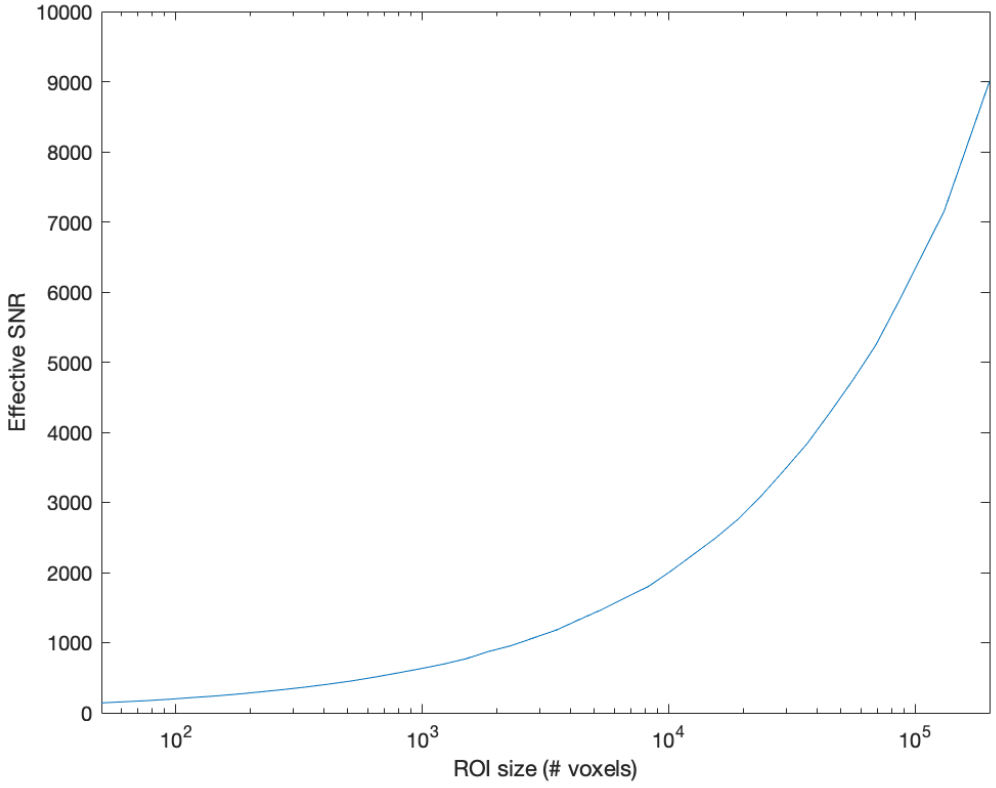

Figure A.9.: *Semi-logarithmic plot of the effective SNR vs ROI size in voxels.*

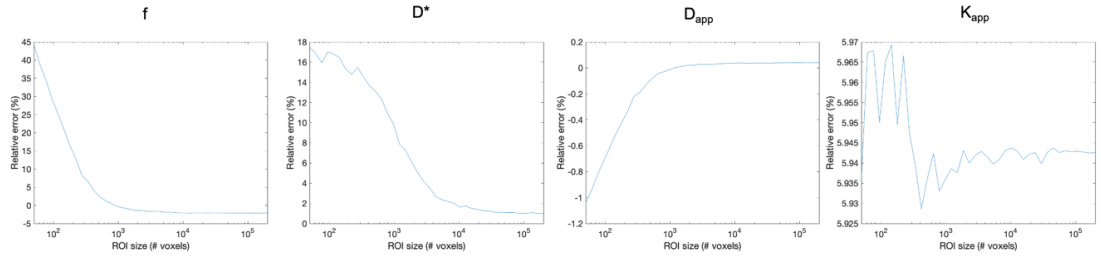

Figure A.10.: *Semi-logarithmic plot of the relative error vs ROI size in voxels.*

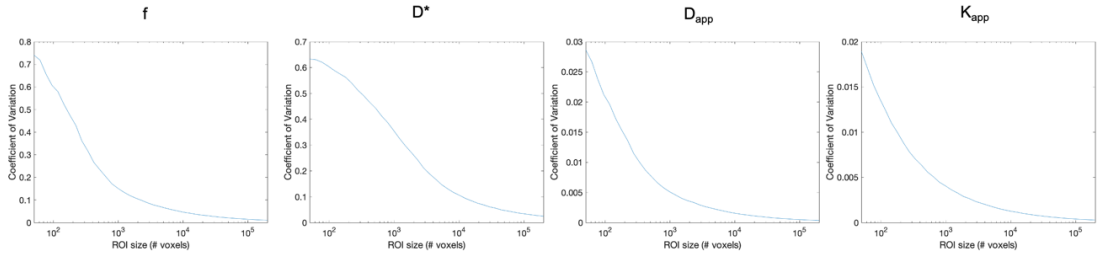

Figure A.11.: *Semi-logarithmic plot of the coefficient of variation vs ROI size in voxels.*

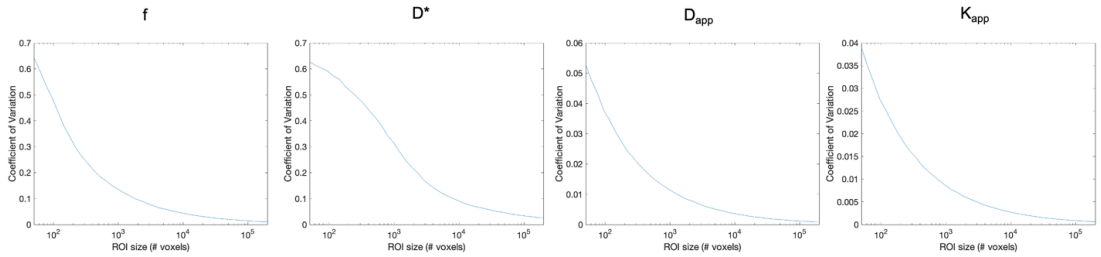

Figure A.12.: *Semi-logarithmic plot of the coefficient of variation vs ROI size for the random ground truth simulations.*

B. Compensation of T2 relaxation effects

When considering T_2 effects arising from different TEs, the signal decay of a diffusion weighted experiment is given by

$$S(b, TE) = S_0(TE)e^{-bD}e^{-\frac{TE}{T_2}} \tag{B.1}$$

where $S_0(TE)$ is the signal at b-value = 0 s/mm^2 and at some TE.

When two measurements are performed at the same b-value but with different TEs, the individual signals are given by

$$\begin{aligned} \frac{S(b, TE_1)}{S(0, TE_1)} &= e^{-bD}e^{-\frac{TE_1}{T_2}} \\ \frac{S(b, TE_2)}{S(0, TE_2)} &= e^{-bD}e^{-\frac{TE_2}{T_2}} \end{aligned} \tag{B.2}$$

The relation between these two signals is driven solely by the T_2 relaxation, since the diffusion terms cancel each other out, resulting in

$$\frac{S(TE_1)}{S(TE_2)} = \frac{e^{-\frac{TE_1}{T_2}}}{e^{-\frac{TE_2}{T_2}}} \tag{B.3}$$

Rewriting Eq. B.3 leads to

$$T_2 = \frac{TE_2 - TE_1}{ln\frac{S(TE_1)}{S(TE_2)}} \tag{B.4}$$

This means that one can estimate T_2 using the acquisition scheme proposed in Chapter 5, since the acquisition of lower b-value and higher b-value ranges have different TEs. This estimation is then used to correct the relaxation effects of, for example, the acquisition with shorter TE (lower b-value range) ahead of merging the datasets and calculating the trace signal. Examples of derived T_2 images are shown in Fig. B.1 for the three representative patients of Fig. 5.1.

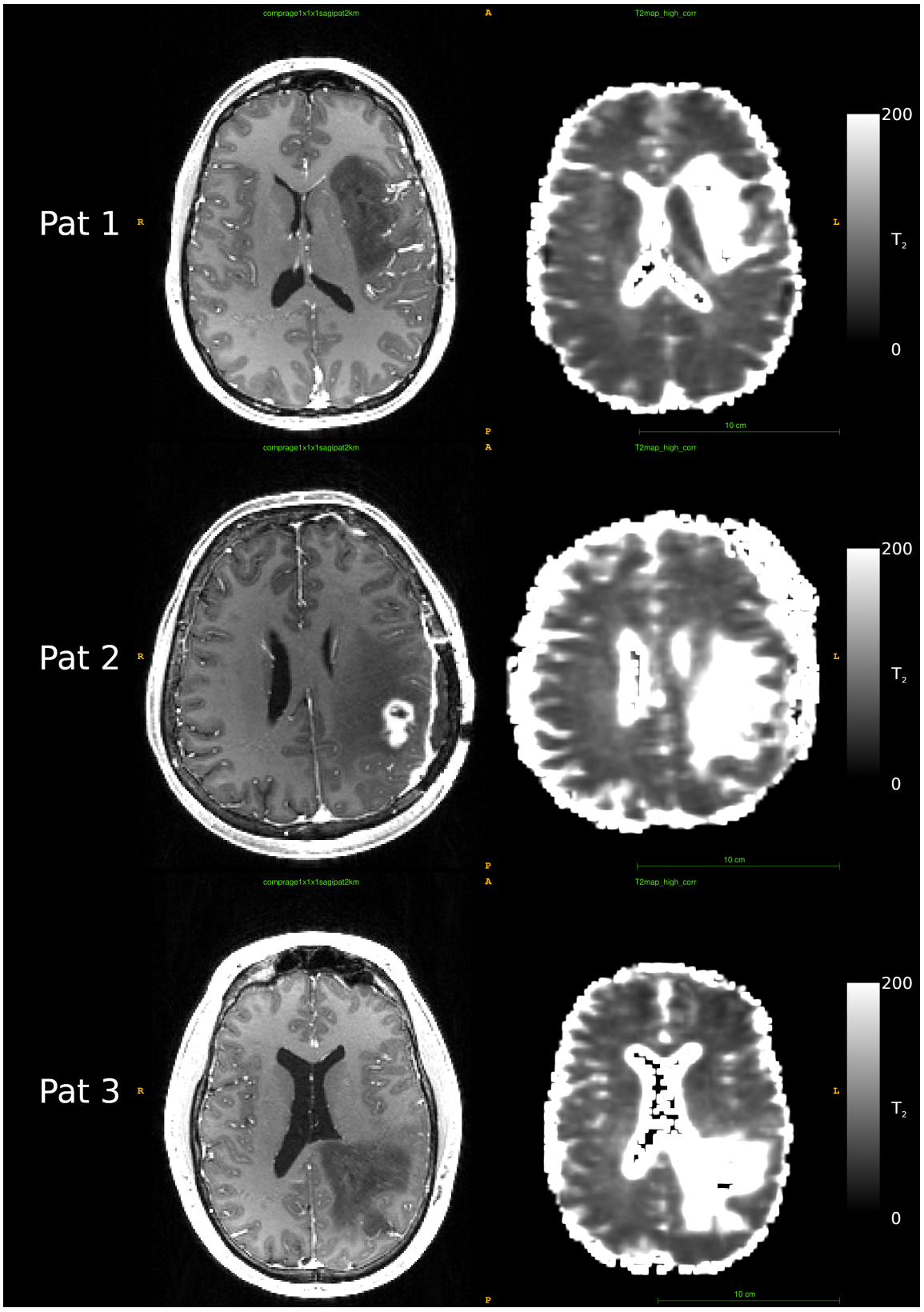

Figure B.1.: *Estimated T2 for the representative patients of Chapter 5. On the left-hand side are shown the T_1C images and on the right-hand side the estimated T2 maps*

.

Acknowledgements

This work would not have been possible without the help of colleagues, friends, and family.

First and foremost, I would like to thank Prof. Shah. I learned quite a lot during my stay in the INM and that would not have been possible had he not welcomed me into the institute and his group. I am particularly thankful to Dr. Ana-Maria Oros-Peusquens and for her mentoring which always pushed me to go above and beyond.

I am also thankful to my colleagues at the INM: Ha, Anna, Dennis, and Mónica, for the endless discussions at the office, always over official matters, of course; Markus, Ezequiel, Alex, Elene, Johannes, Richard, Michael, Robert, Melissa, Nuno, Wieland, for the guidance in navigating the scientific world; Cindy, who always had to help me fill out my hours' sheet; Claire, for proof-reading my, at times, dumb sentences; Elke, Anita, Andrea, and Petra, for teaching me to deal with the big monster that is acquiring an MR image. To the clinical team, Dr. Gabrielle Stoffels and Dr. Christian Fils, for helping me retrieve patient data.

To the long-lasting friends I made in Jülich along the years. Jonas, Dina, and Lisa, for a WG experience I will hardly forget. Alex, Liuba, Valantis, Aitor, and Saskia, for always nagging me with questions like "When are you finishing your PhD?" at our BBQs, which ultimately help boost motivation, especially when there was little in sight.

À minha família, por me terem suportado, não só fisicamente mas também psicologicamente, naquela que foi, até agora, uma das tarefas mais duras nas quais embarquei.

Und Kira, wer immer für mich da war, ist, und sein wird. Du hast mich gezeigt was wirklich wichtig im Leben ist - und zwar nicht immer die Arbeit. And to Leonardo, who, while still in the womb, kicked this work into high gear.

Affidavit according to § 5 (1) for Data Retention

I hereby declare that the original data forming the basis of this doctoral thesis are stored with my supervisor, Prof. N. Jon Shah, Institute of Neurosciences and Medicine, Research Centre Jülich, Jülich, Germany.

Jülich, 14.03.2024
Ricardo Loução

Affidavit according to § 5 (1) § 11 (3) 12 of the doctoral studies regulations

I, Ricardo Loução, hereby declare on oath that I independently collected and prepared the following results portrayed in the dissertation *"Analysis of multi-b-value diffusion MRI data for characterisation of healthy and pathological brain tissue".*

I had the following assistance with completing the dissertation. These are listed in the acknowledgments.

Names	Candidate (Loução)	Practical supervisor (Oros - Peusquens)	Physician(s) (Langen, Stoffels)	Collaborative partners (Ferreira, Fils)	Doctoral supervisor (Shah)	Sum (%)
Study supervision		70			30	100
Study design/conception	20	70			10	100
Examination of the study participants		10	90			100
Delivery of clinical information			70	30		100
Data evaluation	100					100
Development of analysis methods	90	10				100
Statistical evaluation	100					100
Delivery of imaging materials		10	80	10		100
Interpretation of data evaluation	60	30			10	100

_____
Signature of the doctoral candidate

As the supervisor of the above dissertation, I confirm the statements of Ricardo Loução.

_____
Signature of the doctoral supervisor